VNIVERSITAT DE VALÈNCIA

Doctorado en Nanociencia y Nanotecnología

Ph.D. thesis:

Vacuum processed perovskite solar cells

Ph.D. candidate:

Lidón Gil Escrig

Supervisors:

Dr. Hendrik Jan Bolink

Dr. Michele Sessolo

Tutor:

Dr. Hendrik Jan Bolink

Julio 2017

Dr. Hendrik Jan Bolink y **Dr. Michele Sessolo**, Investigador de la Universidad de Valencia en el Instituto de Ciencia Molecular (ICMol) e Investigador Postdoctoral del Instituto de Ciencia Molecular, respectivamente, certifican que la memoria presentada por la doctoranda Lidón Gil Escrig con el título "Vacuum processed perovskite solar cells" corresponde a su Tesis Doctoral y ha sido realizada bajo su dirección, autorizando mediante este escrito la presentación de la misma.

En Valencia, a 10 de Julio del 2017

Dr. Hendrik Jan Bolink Dr. Michele Sessolo

(director y tutor) (director)

Dedicat a la meua família

Acknowledgments

First of all, I would like to thank my thesis director, Dr. Hendrik Jan Bolink for giving me the opportunity to do the PhD in this fantastic group. Thank you very much for all the support given during this period, for trusting in me from the beginning and teaching me all the knowledge I have adquired. Del mismo modo me gustaría agradecer al Dr Michele Sessolo todo el apoyo prestado durante estos cuatro años. Muchísimas gracias por todos los consejos, ideas y ánimos dados, tanto cuando los experimentos han sido todo un éxito como cuando estos no han salido como se esperaba. Muchas gracias por tu infinita paciencia, esta tesis no hubiera sido lo mismo sin tu inagotable ayuda.

A continuación, también me gustaría dar las gracias a cada uno de los que han formado o forman parte de este fantástico grupo, sin ellos el día a día no hubiera sido lo mismo. A ti Cristina, mi eterna compañera, han sido muchos los momentos vividos durante estos cuatro años, momentos de alegría, de excitación, de estrés i alguna que otra decepción. Pero nadie negará que tenemos un 10 en compenetración. Muchas gracias por aguantarme durante estos años tanto en el trabajo como en tu casa, ha sido un placer trabajar contigo. Muchas gracias Laura, por las eternas conversaciones en la pecera, algunas de ellas sin sentido, pero que tan bien vienen en los días de estrés, por la buena energía que desprendes y por ese positivismo que enseguida se pega. Gracias Giulia, por todos los consejos que me has dado, por tu sentido del humor y por enseñarme tanto durante mi tesis. A ti Jorge Ávila, fuiste mi primer “discípulo” y… no lo he hecho tan mal, no? Bromas aparte, muchas gracias por todos los momentos vividos durante estos años ambientados siempre con tu magnífica música. Dani, gracias por todos los memes, por todas las risas en bucle, que muchas veces han durado hasta al día siguiente, contigo he ganado años de vida seguro con tantas risas. Gracias Toni, por estar siempre dispuesto a ayudar, siempre con una gran amabilidad y una gran sonrisa. Moltes gràcies Maria per l’ajuda amb tota la paperassa, per resoldre’m tots els problemes i dubtes que m’han anat sortint durant aquests anys i per haver estat sempre ahí. A Benni, gracias por todos los té de relax imaginarios que nos hemos

bebido en esta última etapa del doctorado. A Pablo, gràcies per totes les explicacions físiques (tant difícils d'entendre a vegades) i estar sempre de tant bon rotllo. A Maria Grazia, muchas gracias por todo el apoyo que me has dado, especialmente en esta última etapa. Azin, for being so funny and crazy at the same time, I really love your sense of humor. Muchas gracias Jorge Ferrando, siempre has reparado lo que a priori parecía irreparable, las evaporadoras y el grupo estarían perdidos sin ti. A Alejandra, gracias por haber estado ahí desde el principio. A Ángel, por estar dispuesto a ayudar en todo momento, por las infinitas conversaciones en la sala limpia, y por el buen rollo y la buena energía que transmites, muchas gracias, eres un ángel,literalmente. M'agradaria donar les gràcies també al Professor Enrique Ortí, per donar-me el seu suport i la seua ajuda durant la realització d'aquesta tesi. Agradecer a todas las personas que han formado parte y que ya no están en el grupo, de las cuales he aprendido mucho a lo largo de esta etapa: Olga, Cristina, Dani, Enrico, David...

Finalment, vull agrair tant a la meua família com als meus amics tot el suport donat durant aquest període. Als meus pares, per haver-me donat sempre el seu recolzament i haver tingut una sega confiança en mi. A ma mare, per tindre una fortalesa enorme i no deixar que em vingue avall en cap moment, gràcies per tot. A mon pare, tot aquest treball va especialment dedicat a tu, perquè sé que et sentiries molt orgullós de mi. De igual manera vull agrair a la meua germana tot el que ha fet per mi, sempre disposada a deixar-ho tot per ajudar-me i per donar-me als que han sigut durant aquesta etapa la meua millor manera de desconectar en els tants moments d'estrés, Luis i Ian.

A Toni, per fer senzill tot allò que al meu cap és complicat. Per aupar-me i ajudar-me a conseguir tots els reptes que em propose. Gràcies per ser el millor company de vida.

No saps del que ets capaç fins que ho aconsegueixes

Index

1. Introduction and aim of the thesis **11**

1.1. Hybrid perovskites 13

1.2 Deposition techniques 16

1.3 Device architectures 21

1.4 Perovskite solar cells operation 23

1.5 Aim of the thesis 26

2. Experimental and methodology **29**

2.1. Fabrication of perovskite solar cells 31

2.2. Perovskite film deposition 33

2.3. Characterization of the solar cells. 35

3. Mixed iodide-bromide perovskite-based diodes for light emission and photovoltaics **39**

3.1 Introduction 41

3.2 Mixed iodide -bromide methylammonium lead perovskite 43

3.3 Experimental methods 43

3.4 Results and discussion 44

3.5 Conclusion 53

4. Fullerene imposed high open-circuit voltage in efficient perovskite based solar cells. **61**

4.1 Introduction 63

4.2 Evaluation of five different fullerenes as electron transport materials 65

4.3 Experimental methods 65

4.4 Results and discussion 66

4.5 Conclusion 73

5. Interface engineering in efficient vacuum deposited perovskite solar cells. **81**

5.1 Introduction 83

5.2 Interface engineering in efficient perovskite solar cells 84

5.3 Experimental methods 84

5.4 Results and discussion 85

5.5 Conclusion 93

6. Conclusions **101**

7. Resumen en castellano **105**

Bibliography **125**

Index of figures **133**

Index of tables **138**

List of abbreviations **139**

Chapter 1.

Introduction and aim of the thesis.

1.1. Hybrid perovskites

In the last decades, the global energy consumption has been continually increasing. Inexpensive, clean and renewable energy sources are needed in order to reduce the dependence on fossil fuels such as coal, oil and gas. Solar energy is one of the most promising candidate among renewable energy sources. The current generation of photovoltaic devices relies on inorganic crystalline semiconductors, such as silicon, cadmium telluride (CdTe) and copper indium gallium selenide/sulphide (CIGS), as the light absorbers. Although they can be efficient and stable, they usually require high energy-input manufacturing, involving high-temperature and complex fabrication processes. Very recently, a new generation of photovoltaic materials has emerged. They make use of organic-inorganic (hybrid) perovskite semiconductors. These perovskite solar cells (PSCs) could become one of the future transformative technologies, due to the low energetic and monetary cost, coupled with their reliance on earth-abundant compounds.

Hybrid perovskites owe their name to the general three dimensional (3D) perovskite structure ABX_3, where A is an organic cation, B is a metal cation and X is a halide anion. The extended perovskite structure is composed by corner-sharing BX_6 octahedra with interstitial A cation. To keep a high-symmetry cubic structure, the Goldschmidt tolerance factor (t) of the perovskite should be close to 1 and is typically between 0.8 and 1.1. It is defined as follows:

$$t = \frac{r_A + r_X}{\sqrt{2}(r_B + r_X)} \qquad \text{Equation 1}$$

Where r represents the ionic radii of A, X or B, as indicated respectively. In the perovskite studied to date in solar cells, the cation B is usually a divalent metal with stable octahedral coordination, the most common ones being Pb^{2+}, Sn^{2+} and to a less extent Ge^{2+}, although some studies have also presented perovskites with trivalent ions such as Bi^{3+} and Sb^{3+}, in which lattice vacancies compensate for the extra charges.[1-4] Extended 3D hybrid perovskites can only form if the organic cation fits in the cavity delimited by

four corner-sharing octahedra. For this reason, only methylammonium (MA) and formamidinium (FA) fulfil such space limitation for organic and readily available cations. The tolerance factors for the most popular lead or tin halide perovskites are listed in Fig 1.1c. When the A site is occupied by groups that are too large, such as alkyl ammonium cations, the lead halide perovskite converts to a two-dimensional (2D) layered structure. The most studied hybrid perovskite for photovoltaics is methylammonium lead iodide, $MAPbI_3$. The $MAPbI_3$ perovskite has a reversible tetragonal (β) to cubic (α) phase transition that occurs at about 56 °C.[5, 6] At low-temperature, stabilized orthorhombic (γ) phase was detected at 100 K, and the phase transition between the tetragonal (β) phase and orthorhombic (γ) phase occurs at about 160 K; the crystal structure for each of the three phases is shown in Fig 1.1a and 1.1b.

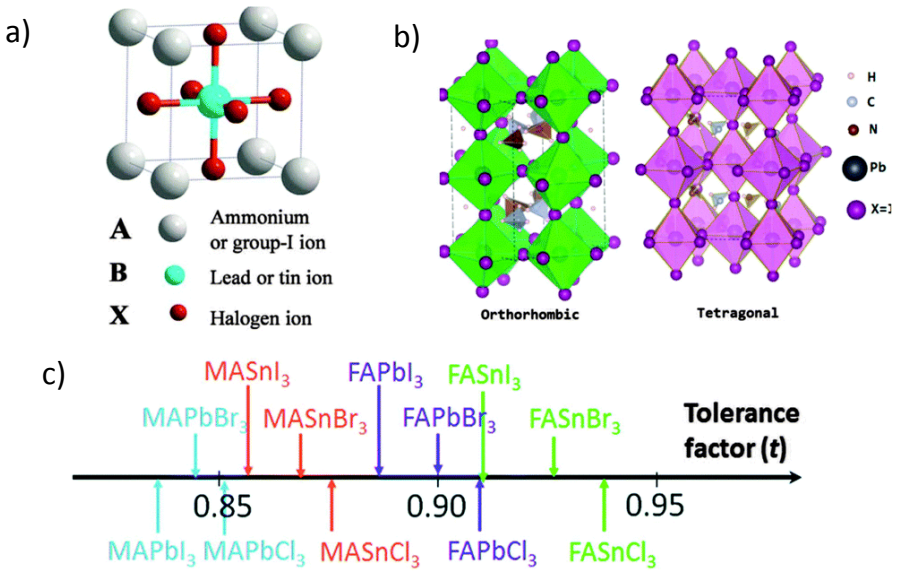

Fig 1.1 (a) Crystal structure of cubic lead halide perovskite (α phase) (b) Crystal structure of the tetragonal crystal system (β phase) and orthorhombic phase (γ phase) of $MAPbX_3$. (c) Tolerance factors of a series of halides perovskites. Adapted from reference 7.

This tetragonal to cubic phase transition accounts, in part, for the thermal stability issue of $MAPbI_3$ perovskite and for its optoelectronic devices.[8] A similar phase transition for $FAPbI_3$ occurs at higher temperature, partially explaining its higher thermal stability.

Hybrid perovskites present a range of desirable properties, which are the origin of the recent interest towards these materials and of the successful application of compounds such as $MAPbI_3$ in photovoltaics. Some of these properties are listed below.

- High optical absorption coefficient

The optical absorption coefficient ($\alpha > 10^5$ cm^{-1}, Fig 1.2) of $MAPbI_3$ is comparable to that of inorganic semiconductors, such as GaAs or CdTe. The large absorption coefficient over a broad wavelength range thus endows $MAPbI_3$ with the advantage to efficiently harvest the incident light while keeping the absorber layer thickness low.

- Low exciton binding energies

Hybrid perovskite films have high dielectric constants with reported values higher than 20, which lead to very small exciton binding energy, which facilitates the generation of free charge carriers within the perovskite at room temperature. [9-12]

- Balanced electron/hole mobility and long diffusion length

A balanced hole and electron mobility, and a large diffusion length of both carriers (in the µm range) has been found in polycrystalline perovskite films, which facilitates the charge extraction from the active material to the electrodes.[13-18]

- Tunable bandgap energy (E_g)

The conduction band of the perovskite is mainly formed by the *p* orbital of the Pb atoms and the valence band by the *p* orbitals of the halide. Hence, the bandgap can be easily tune by exchanging the halide, modifying the covalent/ionic character of the lead halide bond. In $MAPbX_3$, the partial and complete substitution of the iodide, first with bromide and then with chloride, allows to continuously widen the bandgap from 1.6 eV up to about 3.2 eV, which correspond to the fully substituted $MAPbCl_3$. By mixing different halides one can tune E_g over a wide spectral range.[16, 19, 20]

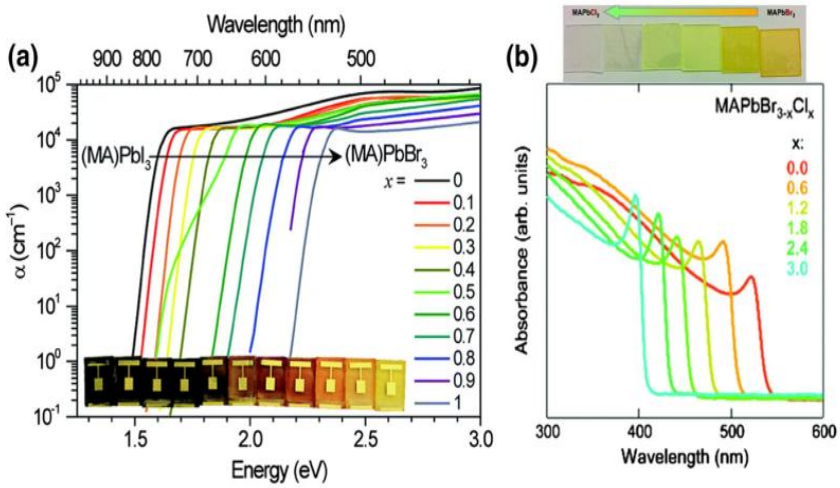

Fig 1.2 (a) Absorption coefficient of mixed $MAPb(I_{1-x}Br_x)_3$ thin films with increasing bromide content, adapted from reference 21. (b) Absorption spectra of mixed $MAPb(Br_{3-x}Cl_x)$ thin film with increasing chloride content, adapted from reference 22.

1.2 Deposition techniques

In order to obtain a high photocurrent in planar perovskite solar cells, the simplest approach would be to increase the absorber layer thickness to maximize photon harvesting. However, this is not straightforward because the film quality and properties are strongly dependent on the perovskite morphology. Actually, one of the main challenges to obtain high performance in solution-processed thin-film perovskite devices is the fabrication of high quality, pinhole-free films with controlled grain size and high surface coverage. All processes of charge separation, transport and diffusion strongly depend on the crystallinity of the film.[23, 24] The crystallization of perovskite compounds is in turn highly dependent on factors such as the deposition methods, the composition, type of substrate (surface chemistry and structure, degree of hydrophilicity, etc.), and the solvents/additives used. For this reason, several deposition techniques have been developed so far. The deposition methods commonly used for the preparation of perovskite films can be divided in two main classes: solution-

and vacuum-based techniques. Each of them includes a variety of modified processes, which are discussed below.[25-28]

1.2.1 Solution processing methods

Solution-based deposition methods are the more widespread because of their simplicity, allowing the preparation of high-quality perovskite films through simple casting of perovskite precursors. The perovskite precursor solutions are obtained by dissolving the inorganic and organic compounds (the metal and organic halide salts) in solvents such as N,N-dimethylformamide (DMF), dimethyl sulfoxide (DMSO), or γ-butirrolactone (GBL). The solution process techniques for depositing perovskite thin films can be grouped into two main categories: one-step and two-step methods, depicted in Fig 1.3.

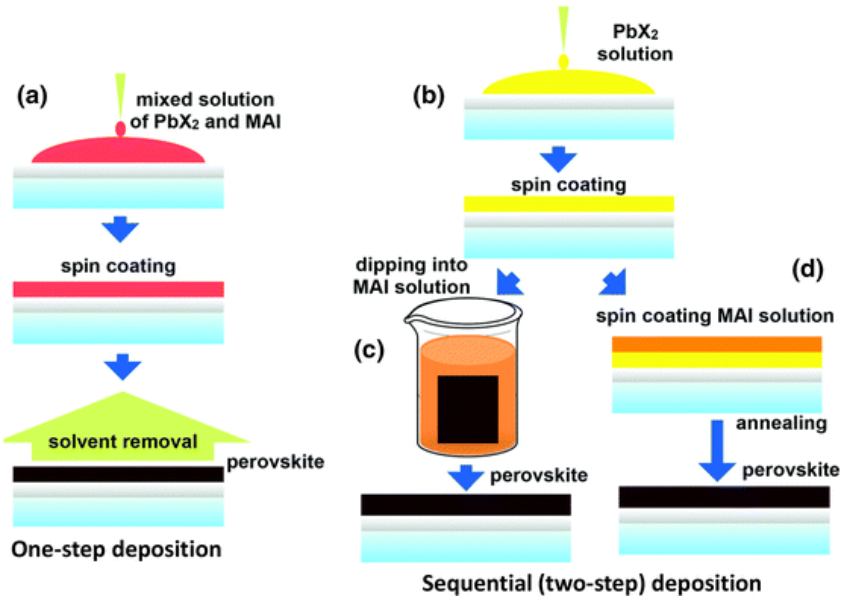

Fig 1.3 Schematics of the different solution deposition methods for hybrid perovskite thin-films, shown here in the case of methylammonium lead halides. Adapted from Reference 28.

In the one-step method, the perovskite is formed by direct spin-coating of a precursor solution, and the process is controlled by the evaporation of excess of solvent and by the subsequent crystallization of the solid perovskite film. The formation of high quality films with good coverage

depends on the speed of the latter processes. For this reason, it is crucial to control the reaction kinetics to achieve the desired morphology and to maintain consistent optical and electronic properties.[29] Moreover, an appropriate post-annealing treatment is important for a quantitative conversion of the precursors to the corresponding perovskites, as well as the choice of the substrate used. An interesting approach to control the rapid crystallization in the one-step method is the dripping of a non-polar solvent (such as toluene or chlorobenzene) over the film during spin-coating. The non-polar solvent modifies the crystallization kinetics, enabling the formation of very dense and homogeneous perovskite films.[30-34] Another way to gain control over the crystallization kinetics is by a two-steps deposition or sequential deposition technique. In this method, the inorganic precursor (PbX_2) is deposited into a uniform, compact film by solution or vapour deposition. Then it is converted to perovskite either by dip- or spin-coating of a solution of the organic cation. The final layer is usually annealed in order to promote the interdiffusion of the organic cation into the PbX_2 layer to ensure the formation of highly crystalline perovskite films.[35-38]

1.2.2 Vacuum deposition methods

Besides solution processing, vacuum deposition methods are also increasingly applied in the preparation of hybrid perovskite thin films. These techniques are widely used in the semiconductor industry on a large scale for several optoelectronics applications. Vacuum deposition techniques present some advantages over solution-based methods:

- High purity of the used precursors.

- Fine control over film thickness and morphology: the deposition rate and the thickness of the film are precisely monitored using quartz crystal microbalance (QCM) sensors. Moreover, this technique typically leads to very flat and homogeneous surfaces.

- Compatible with large area and different kind of substrates: when stoichiometric conditions are used, no annealing is needed after the

perovskite deposition, hence this technique is compatible with any substrate, even temperature sensitive materials such as textile or plastic foils.

- Intrinsically additive: different layers can be deposited on top of each other using vacuum techniques, allowing the preparation of multilayer architectures such as tandem solar cells.

In analogy with solution-based methods, vacuum deposition techniques can also be classified into two main approaches, the dual-source and the sequential vapor deposition.

Dual-source vapor deposition: In this technique the organic cation and the metal halide are simultaneously thermally sublimated in a high vacuum chamber, where they condense and react on a substrate placed above the thermal sources (Fig 1.4). The stoichiometry of the layer is controlled by adjusting the evaporation rate of the two components, giving real time control over the film growth.[26] Different precursors have been used to obtain the $MAPbI_3$ perovskite film. *Liu et al* were the first to use this technique to prepare a high-efficiency perovskite solar cells.[39] They used $PbCl_2$ and excess MAI as precursors which, after an annealing step lead to uniform and highly crystalline films with large grain size. At the same time our research team adopted this method to deposit pure iodide $MAPI_3$ perovskite films.[40] In this case stoichiometry conditions were used, hence no annealing step was needed to convert the as-deposited films. Ono *et al*. developed a similar method where the precursor stoichiometry was ensured by controlling the MAI vapor partial pressure inside the vacuum chamber.[41]

Sequential deposition method: in analogy with solution-based techniques, a sequential deposition method has also been developed, where the formation of the inorganic framework is decoupled from the reaction and intercalation with the organic halide. After the deposition of PbI_2 different ways of conversion have been described such as dipping into a MAI solution,[42] MAI reaction through chemical vapor deposition (CVD)[43] or the sequential deposition of alternating thin (<50nm) PbX_2/MAI multilayers,

where the MAI reaction can take place in solution[44] or in vapor phase.[45] Similarly to the sequential deposition in solution, the as-deposited film is usually annealed to ensure complete conversion of the precursors to perovskite.

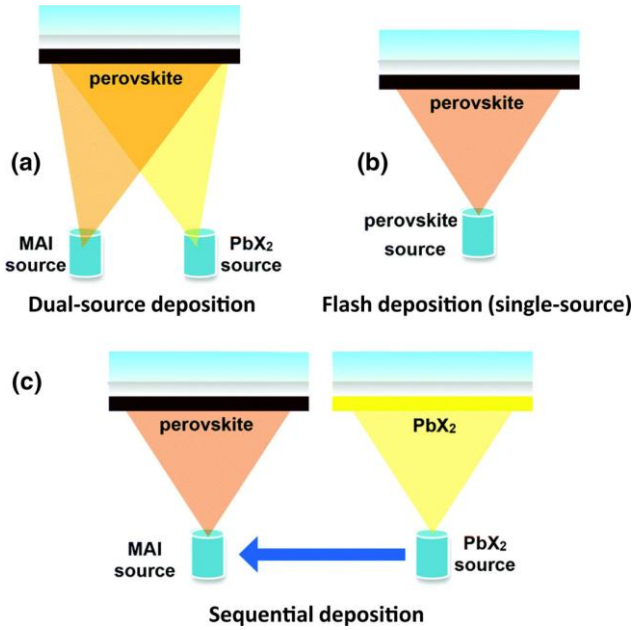

Fig 1.4 Schematics of the different vacuum deposition methods for hybrid perovskite thin-films, shown here in the case of methylammonium lead halides. Adapted from Reference 28.

Flash evaporation: an alternative physical method for the deposition of hybrid perovskite thin films is the flash evaporation. In this case the perovskite is pre-synthesized in the form of powder or as a thin film on a metal substrate. In the latter case, it can be deposited by meniscus coating on top of a tantalum foil and transferred to a vacuum chamber (Fig 1.4). Subsequently, a large current passes through the metal sheet causing the material to rapidly evaporate and condense onto a substrate. This technique is very versatile since it does not depend on the composition/solubility of the material to be evaporated.[46, 47] Recently, we demonstrated an efficient perovskite solar cell, where the active material was deposited by flash evaporation.[48]

All the above mentioned methods can be combined in order to obtain materials with desired thickness, properties, and composition. In the first chapter of this thesis, a combination of the dual source thermal evaporation and the sequential deposition method will be used to prepare a mixed halide perovskite. In the rest of the thesis the materials will be prepared via dual source thermal evaporation, applied to the deposition of $MAPbI_3$ films, which will be incorporated in perovskite solar cells.

1.3 Device architectures

Perovskite solar cells can be fabricated in several different configurations, all potentially leading to high performing devices. This characteristic is largely the result of balanced electron and hole mobilities with long diffusion length in perovskites, which in turns allows almost all device configurations to result in efficient PSCs.

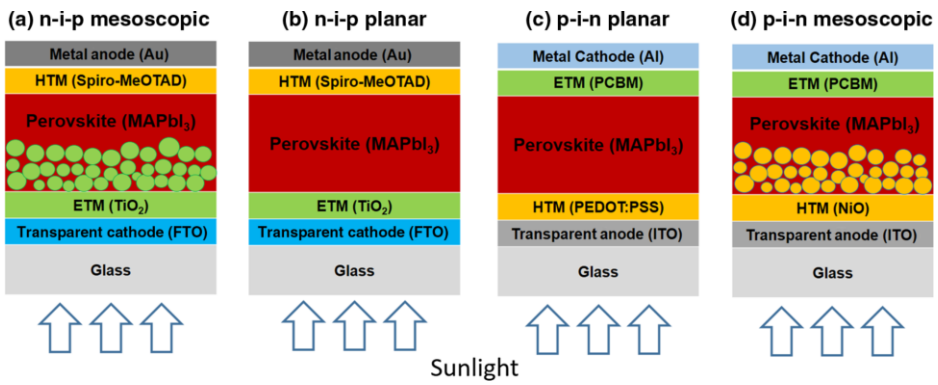

Fig 1.5 Schematics of perovskite solar cells in the (a) n-i-p mesoscopic, (b) n-i-p planar, (c) p-i-n planar, and (d) p-i-n mesoscopic structures. Adapted from reference 49.

The solar cell configurations can be divided into two general groups, mesoporous and planar devices. The first demonstration of a PSC reported by the group of Miyasaka was a dye sensitized solar cell (DSSC), where the traditional organometallic dye was replaced with the perovskite.[50, 51] Hence, common to these early configurations of PSCs is the use of a mesoporous metal-oxide layer (e.g., TiO_2 and Al_2O_3) as the scaffold to deposit the

perovskite, as illustrated in Fig 1.5. In these devices, TiO_2 is used to collect and transport the electrons while a solid state dye (SSD) is used as the hole conductor. [52, 53]

As opposite to DSSC, where a mesoporous metal oxide is needed in order to have sufficient dye infiltration and hence light absorption, it has been shown that perovskite solar cells can also operate in a planar configuration (Fig 1.5). In these devices the absorber material is sandwiched between electron and hole transport layers, either consisting of metal oxides or organic semiconductors. Depending on which transport material (the electron or hole transport layer, n- or p-type, respectively) is deposited on the transparent electrode, these planar structures are referred to as n-i-p, or the inverted, p-i-n. While mesoporous solar cells have been traditionally n-i-p, recently p-i-n mesoscopic perovskite devices using NiO front contact have also been developed.[54, 55]

n-i-p structure

The mesoscopic n-i-p structure is the archetypical architecture for PV devices and has been used to prepare high-efficiency solar cells, now exceeding 22%.[56] These devices typically consist in a FTO (fluorine doped tin oxide) transparent electrode, a 50 - 70 nm thick compact electron transport material (ETM, typically TiO_2), a 150 - 300 nm thick mesoporous metal oxide (mp-TiO_2 or mp-Al_2O_3) that is infiltrated with perovskite. The devices are finished with a thick (up to 300 nm) perovskite capping layer, a 150 - 200 nm thick hole transport layer (HTL, in most reports it consists of a doped 2,2',7,7'-tetrakis(N,N-di-p-methoxyphenylamine)-9,9'-spirobifluorene film, spiro-MeOTAD), and a metal anode (Au or Ag). In this structure, the mesoscopic layer is thought to enhance charge collection by decreasing the carrier transport distance, preventing direct current leakage between the two selective contacts and increasing photon absorption due to light scattering. The planar n-i-p structure is the natural evolution of the mesoscopic configuration, and the materials used very similar. To date, the most efficient n-i-p planar device has achieved 19.3% power conversion efficiency (PCE), after careful optimization of the interface between the indium tin oxide ITO and the TiO_2.[57] PCEs exceeding 20% have been

demonstrated in our group using doped fullerenes as the front contact in n-i-p perovskite cells.[58]

p-i-n structure

When the layer order is reversed and the HTL is deposited below the perovskite, the device is called "inverted" or, more unequivocally, p-i-n cell. Most p-i-n cells use the planar device configuration, and are typically built on a thin (< 100 nm) poly(3,4-ethylenedioxythiophene) poly(styrene-sulfonate) (PEDOT:PSS) conducting polymer film deposited on top of ITO substrates. Subsequently, a thin HTL (< 30 nm) can be applied onto the PEDOT:PSS prior to the perovskite deposition to ensure selective hole extraction. Thick perovskite absorber layers (300 - 600 nm) are usually employed, and the devices are completed with a thin ETL (10 - 50 nm), usually a fullerene derivative such as [6,6]-phenyl C_{61}-butyric acid methyl ester (PCBM), and with a metal cathode. Apart from organic materials, also metal oxide such as NiO and NiO/TiO_2 have been used in this configuration.[59, 60] The use of metal oxide HTLs allow to prepare mesoscopic p-i-n devices, based on $NiO/mp\text{-}Al_2O_3$ or c-NiO/mp-NiO.[54, 61]

In this thesis the architecture chosen for the perovskite solar cells is the planar p-i-n configuration, using organic semiconductors both as the hole and electron transport layers.

1.4 Perovskite solar cell operation

Upon illumination, the absorption of photons by the active material (perovskite) generates electron-hole pairs (i.e. excitons) within a few picoseconds. As discussed previously, perovskites such as $MAPbI_3$ present low exciton binding energies, leading to the formation of free electrons and holes immediately after illumination. These electrons and holes are selectively extracted by the hole and the electron transport materials and collected at the electrodes. In perovskite solar cells, the mobility of charge carriers and the exciton binding energy are two key parameters that control the carrier recombination and hence the efficiency of the device. There are mainly three types of recombination in semiconductors materials (Fig 1.6):

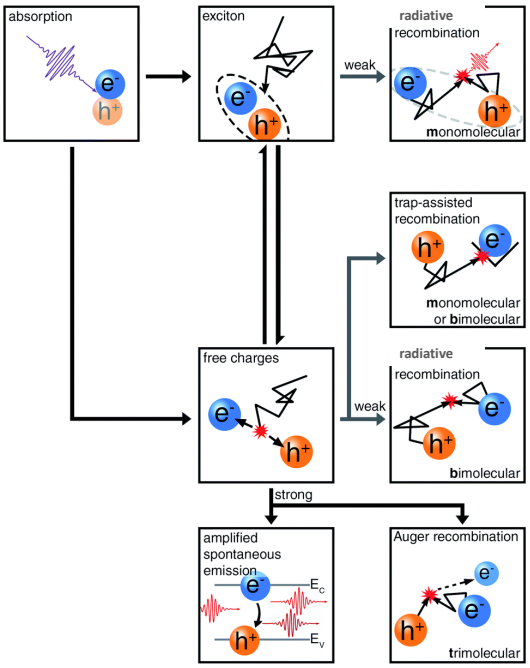

Fig 1.6 Scheme of the different types of recombination depending on the exciton binding energy. Adapted from reference 62.

- non-radiative (trap-assisted) recombination

The probability of such recombination depends on the density of the defects, which are unavoidably present in any material. Most defects induce localized energetic states within the bandgap, called electronic traps. Free carriers can be captured in traps and, once a carrier of the opposite charge comes in the proximity of the same trap, non-radiative (trap-assisted) recombination can occur.

- Radiative recombination

Radiative recombination is the process by which an electron relaxes from the conduction band to the valence band with the emission of light. An increase of the carrier concentration will increase the probability to meet and recombine.

- Non-radiative Auger recombination

Auger recombination is a higher-order process that occurs when an electron and hole recombine and transfer the excess energy to a nearby carrier.

In order to have an efficient charge extraction in perovskite solar cells, non-radiative recombination should be minimized. For this reason, the amount of defects in the perovskite films and in the complete device should be reduced. Although the presence, the nature and the distribution of traps are still under investigation, it has been shown that polycrystalline $MAPbI_3$ films present shallow and deep traps.[63] Here, as we have discussed before, the deposition methods and the different substrates used may influence the morphology of the films, hence determining the density of defects in the perovskite film. Apart from the bulk or surface of the perovskite film, charge recombination can also take place at the interface between the perovskite and the transport layers, hence the choice of materials and the optimization of their thickness is very important in order to reduce recombination losses. It has been shown that under normal solar cell operating conditions, trap-assisted recombination is the dominant recombination path.[64]

Solar cells and light-emitting diodes are complementary devices, transforming photons into electrons or vice versa. In their simplest form, organic light emitting diodes (OLEDs) are electronic devices consisting of a thin film of an electroluminescent organic material sandwiched between two conductors with different work functions. When an external voltage is applied, electrons and holes are injected into the electroluminescent layer and when they recombine, light is emitted. It has been demonstrated that efficient materials for solar cells, in addition to be good absorbers, must also emit light efficiently.[65] This is because in such materials the non-radiative recombination, which is the main loss path in solar cells, is minimized. The Shockley-Queisser limit (SQ), describing the maximum theoretical efficiency of a solar cell, assumes perfect external quantum efficiency of electroluminescence (EQE_{EL}) at open circuit conditions.[65] In fact, inefficient EQE_{EL} at open circuit is an indicator of non-radiative recombination and optical losses. In view of the above, radiative

recombination should be the only recombination process occurring in the device, as the non-radiative deactivation would be detrimental for the $V_{oc.}$[65] The reciprocity relation allows predicting the photo-voltage by measuring EQE_{EL}, which is therefore an additional figure of merit to evaluate the performance of perovskite solar cells. From equation 2, we can evaluate the relation between the V_{oc} and the external quantum efficiency.

$$V_{oc} = V_{oc,rad} - \frac{kT}{e} ln(EQE_{EL})^{-1} \qquad \text{Equation 2}$$

Where *e* is the elementary charge, $V_{oc,rad}$ is the maximum voltage in the radiative limit, k is the Boltzmann constant and T the temperature. At open circuit, an ideal solar cell would emit a photon for every photon that was absorbed. Hence, the external luminescence efficiency is an indicator of whether any additional loss mechanism (non-radiative recombination) is present. By operating the diode in forward bias the perovskite solar cells can function as a light-emitting diode (LEDs) and the current density and electroluminescence can be measured to derive the EQE_{EL}.[26]

In all of the chapters of this thesis the perovskite solar cells prepared will be also characterized as light-emitting diodes, in order to quantify EQE_{EL}.

1.5 Aim of the thesis

The aim of this thesis is the development of vacuum deposition methods for the fabrication of perovskite thin films, and their incorporation into devices using organic charge transport layers. The thesis will be structure as follows:

- Chapter 1: preparation of efficient single-junction perovskite solar cells with tunable bandgap using vacuum processed techniques.

- Chapter 2: study the effect of different fullerene derivatives as electron transport materials on the performance of perovskite solar cells. Additionally, the interface between the fullerene and the perovskite is optimized, in order to reduce the non-radiative recombination and maximize the photovoltage.

- Chapter 3: Interface engineering towards stable electron transport materials. Development of a new electrode buffer layer as an alternative to reactive metal cathodes in p-i-n perovskite solar cells.

Chapter 2.

Experimental and methodology.

2.1. Fabrication of perovskite solar cells

Processing, preparation and characterization of the devices were carried out in a class 10000 clean-room (Fig 2.1). The preparation of the devices consists of the following steps:

a) Cleaning of the substrates with soap, water and isopropanol in an ultrasonic bath, followed by O_2 plasma treatment.

b) Spin-coating of the organic layers, performed inside the clean-room in atmospheric conditions.

c) Deposition of the perovskite layers

- $MAPbI_3$: dual source vapor deposition technique using MAI and PbI_2 as a precursors.
- $MAPbBr_3$: two steps deposition technique. Vacuum deposition of $PbBr_2$, and conversion into perovskite via solution with MABr.

d) Thermal vacuum deposition of the cathode and characterization of the device under inert conditions in a nitrogen-filled glove box.

Fig 2.1 Nitrogen-filled glove box installed inside the clean-room at the Instituto de Ciencia Molecular (ICMol) of the Universidad de Valencia where all the devices were prepared and characterized.

All devices studied in this work have the following stack architecture: ITO/PEDOT:PSS/polyTPD/perovskite/ETL/metal (Ba-Ag or Al). Pre-patterned indium tin oxide (ITO) covered glass substrates were used. Poly(3,4-ethylenedioxythiophene) doped with poly(styrene sulfonic acid) (PEDOT:PSS) was obtained from Heraeus Holding and used as received. Poly[N,N'-bis(4-butylphenyl)-N,N'-bis(phenyl)-benzidine] (polyTPD) was purchased from ADS Dye Source. PbI_2 and $PbBr_2$ were purchased from Sigma Aldrich, MAI and poly(9,9-bis[3'-(N,N,N-ethyldimethylammonium)propyl]-fluorene-2,7-diyl) dibromide -alt- (9,9-dioctylfluorene-2,7-diyl) (PFNBr) from Lumtec and MABr from Dyesol, all of them were used as received. All fullerene derivative tested were purchased from Solenne BV. The N,N'-bis(dimethylaminopropyl-N'''-oxide)-perylene-3,4:9,10-tetracarboxidiimide (PDINO) was synthesized according to a previously published protocol by the group of Professor Sastre of the University Miguel Hernández.[66]

The devices were fabricated as follows. First, a 80 nm thick layer of PEDOT:PSS was spin-coated on the ITO glass substrate. The purpose of this layer is to smooth the ITO surface, hence improving the reproducibility of the devices and preventing the formation of pinholes that can lead to shorts. It also increases the work function of the electrode, enhancing the hole extraction from the perovskite. On top of PEDOT:PSS a thin film of polyTPD (15 nm) HTL was deposited from a chlorobenzene solution (7 mg mL^{-1}). Then the substrates were transferred to a vacuum chamber where a 300 nm thick $MAPbI_3$ perovskite film was deposited by dual-source vapor deposition,[40] the details of this process step are described in section 2.2. For the deposition of the $MAPbBr_3$, we used the two step deposition technique, for which a crucible with $PbBr_2$ was heated at 240 ºC and films of increasing thickness were deposited. The $PbBr_2$ films were converted to perovskite by spin coating a MABr solution in isopropanol. The concentration of this solution was increased with increasing thickness of the $PbBr_2$ layer. The fullerene layer was spin-coated from a chlorobenzene solution (20 mg mL^{-1}) in ambient conditions. When we tested the PDINO and PFNBr as interface materials, they were spin-coated from a methanol

solution (concentrations of 1 mg mL^{-1} or 2 mg mL^{-1}, respectively). Finally, all devices were completed by the thermal evaporation of the top electrode under a base pressure of $2 \cdot 10^{-6}$ mbar to a thickness of 100 nm of Ag or Ba/Ag (10/100 nm). In general, devices were not encapsulated and were characterized inside the inert atmosphere globe box at room temperature.

2.2. Perovskite film deposition

The vacuum deposition of the perovskite was performed using a vacuum chamber integrated in a nitrogen-filled inert glovebox, Fig 2.2. Temperature controlled evaporation sources fitted with ceramic crucibles were employed to sublime the CH_3NH_3I and the PbI_2. The sources are directed upwards with an angle approximately 90^o with respect to the substrate. The substrates were placed at a distance of 20 cm from the evaporation sources. A shutter below the substrate holder is used to control the final perovskite film thickness. Three quartz crystal microbalance (QCM) sensors are placed in the chamber, two monitoring the rate of each evaporation source and a third one at the altitude of the substrate holder.

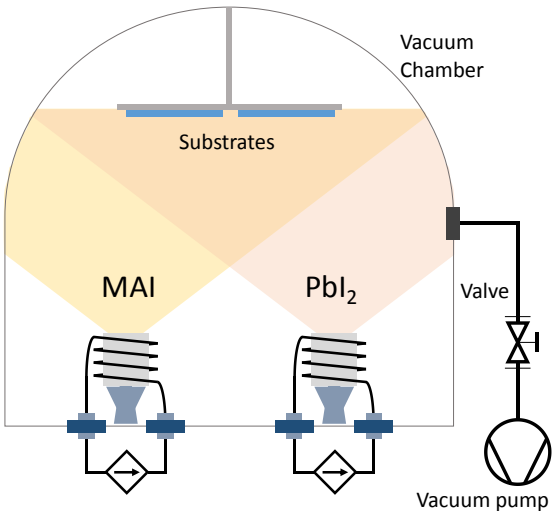

Fig 2.2 Scheme of the thermal vacuum deposition tool used in the dual source evaporation process.

The ceramic crucibles were loaded with the CH_3NH_3I and the PbI_2 and the chamber was evacuated to a base pressure of 10^{-6} mbar. The crucible

containing MAI was refilled (or cleaned and refilled) with pristine MAI. After the base pressure was reached, the CH_3NH_3I crucible was heated to 75 ºC. At this temperature, all three sensors gave a signal. Unfortunately we were unable to calibrate the material deposition rate by measuring the thickness of a deposited MAI film, as the films were very soft and not homogeneous. In order to address this issue, we kept constant the temperature of the crucible for this material and adjusted the deposition rate or the PbI_2 until the right stoichiometry was achieved (monitored a posteriori by optical absorption and x-ray diffraction). The total film thickness of the perovskite film was monitored using a third QCM sensor placed at the height of the substrate holder.

2.3. Characterization of the films

In order to ensure the perovskite formation and to guarantee the reproducibility of the devices, all the films were characterized with the following techniques.

First of all, the thickness of each layer was measured with a contact profilometer (Ambios XP-1) on control samples. These measurements allow us to optimize the deposition conditions (for example in the case of spin-coating the spin speed, concentration and solvent of the solution) in order to reach the optimum thickness for each layer. Also, as the absorption is proportional to the layer thickness, it was used to corroborate the profilometer data by measuring the UV-Vis absorption spectrum of the films, using an Avantes Avaspec-2048 spectrometer.

For the characterization of the perovskite layer, a more exhaustive control on every deposited film was carried out. Apart from the measurement of the layer thickness with the profilometer, every time we have collected the absorption spectrum in order to monitor the formation of the perovskite. The crystallinity of the vacuum deposited perovskite was investigated by grazing incidence X-ray diffraction (GIXRD) measurements which were collected at room temperature on an Empyrean PANalytical powder diffractometer using the Cu $k\alpha_1$ radiation. Typically, three consecutive measurements were collected and averaged into a single spectrum. Finally,

the surface morphology of the films was investigated using atomic force microscopy (AFM), using a Multimode SPM, Veeco, USA.

2.3. Characterization of the solar cells.

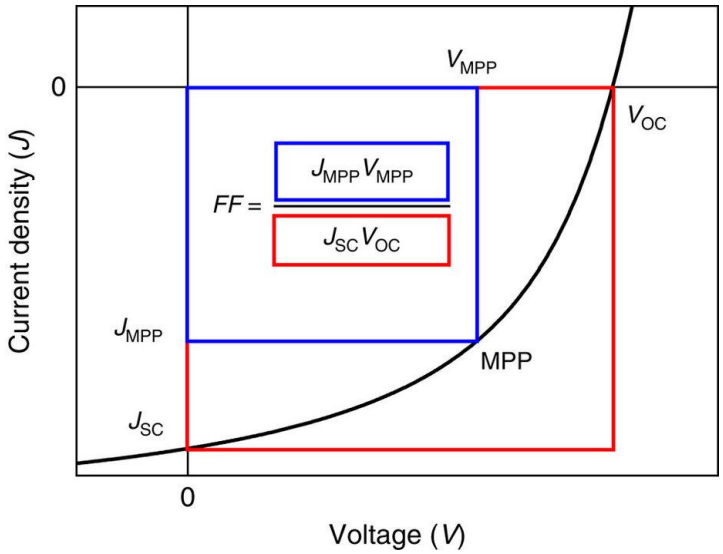

Fig 2.3 J-V characteristic of a typical solar cell, highlighting the main parameters used in the characterization. The product of V_{mp} and J_{mp} is the maximum power that the solar cell can deliver.

The parameters used to calculate the efficiency of the solar cells, extracted from the current density versus voltage (*J-V)* curves measured under standard AM 1.5 G illumination, are reported here as a reference (Fig 2.3):

- **Current density at short circuit**, J_{sc}. Measured in mA cm^{-2}, is the current density generated by the solar cell when the external voltage V = 0 V. Values of J_{sc} for state-of-the-art PSCs exceed 20 mA cm^{-2}.

- **Open circuit voltage**, V_{oc}. Measured in V or mV, this value represents the maximum voltage attainable from the photovoltaic device and is measured when the current through the cell is 0 A. The value of V_{oc} depends on the bandgap of the perovskite, the energy

levels of the charge transport layers, and the work function of the electrodes. Record values of V_{oc} for PSC based on $MAPbI_3$ are in excess of 1.1 V.

- **Maximum power point (MPP)**: The maximum of the power output curve of a solar cell (product of voltage and current density, *V* x *J*). While the maximum voltage and current attainable are V_{oc} and J_{sc}, respectively, at those extremes the power is zero. Hence at the MPP $V_{mp} < V_{oc}$ and $J_{mp} < J_{sc}$, where V_{mp} and J_{mp} are, respectively, the voltage and the current of the cell when it is delivering its maximum power output.

- **The fill factor**, *FF*. Reported as percentage, it essentially measures the efficiency of the charge extraction in a solar cell. It is calculated as $(V_{mp} \cdot J_{mp})/(V_{oc} \cdot J_{sc})$. In short, *FF* is the ratio of the actual power delivered by the solar cell to its theoretical maximum power and measures the "squareness" of the *J-V* curve. Graphically, it is the ratio between the areas of the blue and the red rectangles in Fig 2.3. State-of-the-art PSCs have $FF \geq 80\%$.

The power conversion efficiency (PCE, or η) of a solar cell is expressed in percentage and calculated using the formula:

$$\eta = \frac{FF \cdot J_{sc} \cdot V_{oc}}{P_{in}} \times 100 \qquad \text{Equation 3}$$

Where P_{in} is the incident light power (100 mW cm^{-2} for standard AM 1.5 G illumination).

In some cases, the solar cells were characterized as light-emitting diodes. In this case, in order to make reliable comparisons between different devices, we used the common parameters established as indicators of the electroluminescence:

- **Electroluminescence (EL) spectrum**: The EL spectrum consists in the intensity of electroluminescence as a function of the photon wavelength. It gives information on the excited states of the active

material and determines the color of the electroluminescence. The wavelength corresponding to the maximum of the emission peak of the EL spectrum is often reported and indicated as λ_{max}.

- **Irradiance ($\mu W\ cm^{-2}$):** It represents the radiant flux (power, W) associated with the light emission per unit of surface in a given direction.
- **Current density**: The intensity of the current per unit of surface ($A\ m^{-2}$).
- **External quantum efficiency (EQE)**: The ratio of the number of emitted photons per injected electrons in a device. It depends on the charge injection and recombination, on the radiative recombination efficiency and on the light outcoupling from the device.

The characterization of the solar cells was performed using two methods. External quantum efficiencies (EQE) measurements were performed using a white light halogen lamp in combination with band-pass filters (MiniSun simulator by ECN, the Netherlands). The perovskite cells were continuously illuminated at a defined wavelength and the short-circuit current monitored over time. Since the current is expressed as number of electrons (e) over time and the amount of available photons at every wavelength is known, one can calculate the EQE ratio e/photon. Current-voltage (I-V) characteristics were measured using a Keithley 2400 source measure unit with and without illumination. The light source was a 10500 solar simulator by Abet Technologies. Before each measurement, the exact light intensity was set at 100 mW/cm^2 using a calibrated Si reference solar cell. The current-voltage (I-V) and electroluminescence-voltage (L-V) characteristics were collected using a Keithley Model 2400 source measurement unit and a Si-photodiode coupled to a keithley Model 6485 picoamperometer, respectively. The electroluminescence spectra were recorded using an Avantis fiber-optics spectrometer.

Chapter 3.

Mixed iodide-bromide perovskite-based diodes for light emission and photovoltaics.

3.1. Introduction

Silicon solar cells dominate the photovoltaic market, and are also good candidates for bottom-cells in tandem architectures, in combination with a complementary wide-bandgap solar cell. Apart from silicon, copper indium gallium selenide (CIGS) solar cells with a bandgap of 1.15 eV, have been investigated as bottom-cells in monolithically-integrated tandem devices.[67] Based on the different simulations made, efficiencies above 35% could be achieved with top-cells having a bandgap of 1.7-1.75 eV.[68-71] The challenge for tandem solar cells is to find a cost-effective and high efficiency wide-bandgap top-cell. Since the beginning of the perovskite solar cells development, they have been considered as potential candidates for top-cells in tandem devices, thanks to the wide range of desirable properties they possess. A unique feature of these materials is their flexibility in terms of bandgap energy (E_g), which can be tuned by simple exchange of their components. The bandgap of the most widely studied hybrid perovskite, $MAPbI_3$, is about 1.55 eV. The $MAPbI_3$ bandgap can be narrowed by exchanging methylammonium with formamidinium, leading to a better solar spectrum matching and thus enhanced photocurrent when the compound is used as absorber in a solar cell.[13, 24, 72] Also, the use of different alkyl and aromatic ammonium halides modifies the bandgap of the resulting 2 or 3D perovskite.[73] Due to their bandgaps and the correspondent electroluminescence, these mixed alkyl-ammonium perovskites have been studied mainly in light-emitting devices.[74-77] In order to increase the perovskite bandgap, the simplest strategy is the partial or complete substitution of the iodide with bromide or chloride. Although most of the studies that have been published are focused on the bromide substitution, the replacement with chloride allows to continuously widen the bandgap up to 3.2 eV, which correspond to the fully substituted $MAPbCl_3$.[78] The complete replacement with bromide allows to reach a bandgap of about 2.3 eV which, with the proper selection of charge-transporting layers, can lead to photovoltaic devices having high V_{oc}, up to 1.5 V.[79] As discussed above, the ideal bandgap for the integration with Si and CIGS cells in tandem architectures lies in the range of 1.7 to 1.75 eV.[68-71] In order to obtain this bandgap, the most convenient strategy is to partially substitute the I^- by Br^-

to form a mixed-halide perovskite solar cell (PSC). Several approaches have been developed in order to reach this goal, most of which relies on controlling the I/Br stoichiometry by varying the relative concentrations of the halides precursors in solution. *Noh et al*[19] were the first to show that the bandgap of $MAPb(I_{1-x}Br_x)_3$ increases with increasing Br content. In this case, they simply spin-coated the proper precursors from DMF solutions. In this early study, however, the quality of the films was not high, leading to charge recombination losses which were limiting the performance of the solar cells. In order to improve the morphology of the films, a sequential deposition method was develop by *Cheng et al.*[80] They spin-coated the PbI_2 films and converted them to perovskite by spin-coating with MAI/MABr precursor solutions with different molar ratios. They obtained a PCE of 13.1% for a solar cell employing a perovskite with a bandgap of 1.72 eV. The sequential deposition has been widely applied because in this way the formation of the inorganic lead halide framework is decoupled from the reaction and intercalation with the ammonium halide.[35] Physical vapor deposition methods for the hybrid perovskite have also emerged, leading to high efficiency photovoltaic devices.[9, 39, 40, 58] Such techniques have intrinsic advantages over solution-based methods, such as, high purity layers, compatibility with large area, and fine control over film thickness and morphology. Importantly, vacuum methods are additive, meaning that multilayer devices can build without chemical modifications of the underlying layers. Also, mixed deposition route, where the lead halide is deposited by vacuum deposition and the converted to perovskite by solution, has also been demonstrated.[42, 81]

Although wide-bandgap PSC can be obtained by tuning the halide composition, at high bromide content phase segregation into bromide and iodide rich domains takes place. This phenomenon is typically light-induced and detrimental for the photovoltaic (PV) performance, since the V_{oc} of the device is limited by the bandgap of the iodide-rich phase (the one with the narrower bandgap). Despite the many studies on the topic, up to now there is not a clear and definitive solution to this problem.[21, 82, 83]

3.2. Mixed iodide-bromide methylammonium lead perovskite

A novel method to prepare mixed $MAPb(I_{1-x}Br_x)_3$ perovskite with different bromide content (x) is presented. The method consists in merging two stacked perovskite layers, each having its own composition and phase. To prepare both layers, vacuum-based deposition techniques are employed. The deposition of the $MAPbI_3$ film is done by co-evaporation, followed by the evaporation of a $PbBr_2$ layer. The latter is converted into the corresponding perovskite by exposure to MABr via solution processing. When this bilayer is annealed, halide interdiffusion takes place, producing the mixed halide perovskite phase (Fig 3.1). The content of bromide and hence the bandgap of the perovskite is controlled by the thickness of the $MAPbBr_3$ film. p-i-n diodes were prepared by depositing the perovskite bilayers between a hole transporting polymer and a fullerene electron-transporting layer.

3.3. Experimental methods

ITO-coated glass substrates were subsequentially cleaned with soap, water and isopropanol in an ultrasonic bath, followed by O_2 plasma treatment. Then, they were coated with a 70 nm thick film of PEDOT:PSS and with a thin (15 nm) layer of polyTPD acting as the hole-transporting and electron-blocking material. Substrates were transferred into a high vacuum chamber where 300 nm thick $MAPbI_3$ perovskite films were deposited by dual-source vapor deposition, as detailed in section 2.1. Without breaking the vacuum, thin films of $PbBr_2$ with different thicknesses were deposited on top of the previous perovskite. Finally, the conversion into $MAPbBr_3$ perovskite was carried out by spin-coating of an isopropanol solution of MABr onto the $PbBr_2$ layers. Optical absorption confirmed the formation of the high bandgap perovskite even without any heat treatment (Fig 3.2.c). The concentration of this solution was increased for increasing thicknesses of the $PbBr_2$. After this, an annealing treatment at 100 ºC for 5 min was performed in order to obtain the mixed perovskite $MAPb(I_{1-x}Br_x)_3$. A scheme of the perovskite preparation is reported in Fig 3.1. To finish the devices a thin layer of PCBM was spin-coated from a chlorobenzene solution (20 mg mL^{-1}) in ambient conditions. The devices were completed by thermal

evaporation of the top metal electrode (10 nm Ba capped with 100 nm Ag) under a base pressure of $2 \cdot 10^{-6}$ mbar. The device characterization was performed as described in chapter 2.2.

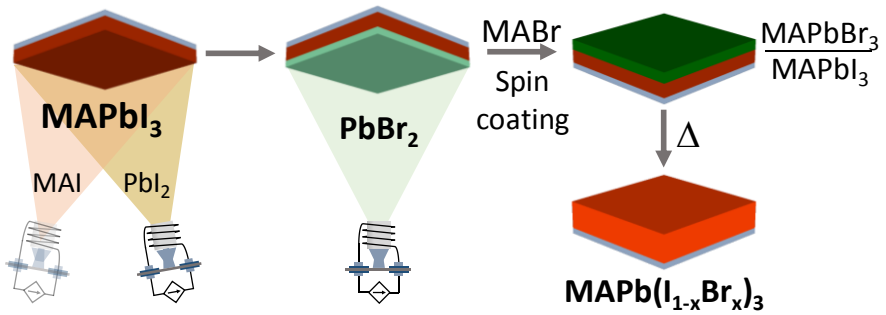

Fig 3.1 Process schematics with the deposition steps used to prepare the mixed halide perovskite.

3.4. Results and Discussion

The formation of the mixed halide perovskite $MAPb(I_{1-x}Br_x)_3$ was confirmed from optical absorption, as shown in Fig 3.2.a. As the thickness of the top-deposited $MAPbBr_3$ layer was increased, the onset of the absorption blue shifted with respect to the pure $MAPbI_3$ (1.55 eV), as represented in Fig 3.2.b. The bandgap of the mixed $MAPb(I_{1-x}Br_x)_3$ films increased when the thickness of the $MAPbBr_3$ was increased. Specifically, with 20, 40 and 60 nm thick $MAPbBr_3$ the obtained bandgaps were 1.61, 1.64 and 1.70 eV, respectively. When the thicknesses of the second bilayer were 100 and 200 nm, the bandgap energies increased considerably showing a much steeper absorption onset, reaching values of 1.80 and 1.92 eV, respectively. One point to take into account is that the onset of the absorption with 20, 40 and 60 nm thick $MAPbBr_3$ films was not as steep as compared to those obtained with 100 and 200 nm layers on top of the $MAPbI_3$. This could be attributed to an increased disorder in these films and some extent of phase separation following the iodide/bromide interdiffusion.[84]

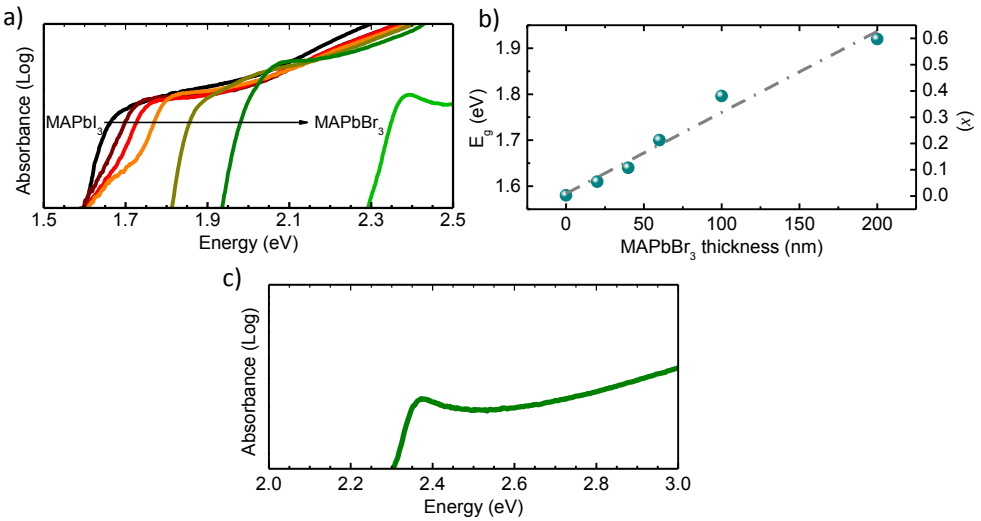

Fig 3.2 (a) Optical absorption spectra for a series of $MAPb(I_{1-x}Br_x)_3$ perovskite films prepared with increasing thicknesses of the $MAPbBr_3$.(b) Variation of the optical bandgap for the same series of $MAPb(I_{1-x}Br_x)_3$ films, with the estimated Br content (right axis) (c) Optical absorption of a pristine $MAPbBr_3$ perovskite thin film obtained by converting a pre-deposited $PbBr_2$ layer by spin-coating with MABr solutions in isopropanol. No annealing is needed in order to obtain the pure bromide-based perovskite.

The surface morphology of these films was analyzed using atomic force microscopy (AFM) and scanning electron microscopy (SEM). As depicted in Fig 3.3.a, the surface morphology of the $MAPbI_3$ was compact and homogeneous, composed by grains with size on the order of 100 - 500 nm. The root-mean-square (RMS) roughness of the sample was 22.1 nm (Fig 3.3.a). When a thin layer of $PbBr_2$ was deposited on top of the $MAPbI_3$ perovskite, the surface morphology changed substantially (Fig 3.3.b), becoming smoother (RMS = 8.7 nm) due to the presence of very small, densely packed grains (< 50nm). After the conversion to $MAPbBr_3$ and interdiffusion of the iodide/bromide, the morphology of the perovskite changed again. The resulting film surface (Fig 3.3.c) was composed of cubic-like closely packed crystals, with slightly increased roughness (RMS = 23.0 nm). These surface characteristics are in agreement with other reported previously.[42, 45]

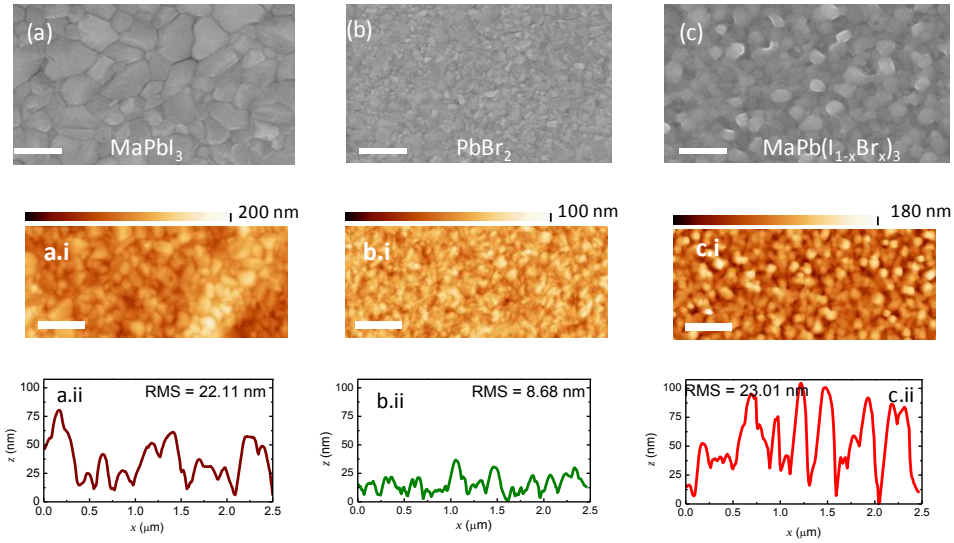

Fig 3.3 On the top, correspondent evolution of the surface morphology as monitored by scanning electron microscopy (SEM, scale bar 500nm). On the bottom, atomic force microscopy (AFM) characterization of the (a) $MAPbI_3$, (b) $PbBr_2$ and (c) $MAPb(I_{1-x}Br_x)_3$. The indexes indicate (i) the surface topography (scale bar 1 cm), and (ii) a profile along the scanning direction.

The formation of the mixed halide perovskite was also confirmed by XRD, Fig 3.4. A shift of the XRD signal to higher angles in the 2θ range 27.5 - 31º was observed when the amount of bromide was increased. Such a shift is in agreement with the transition from the tetragonal ($MAPbI_3$) to the cubic phase ($MAPbBr_3$).[19] For compounds with x = 0.4 and x = 0.6, a minor contribution from unconverted $MAPbI_3$ was also observed, see Fig 3.4. A reason for this incomplete conversion could be that the thickness of the $PbBr_2$ layers was rather high, hindering the interdiffusion of the halide ions through the whole perovskite film.

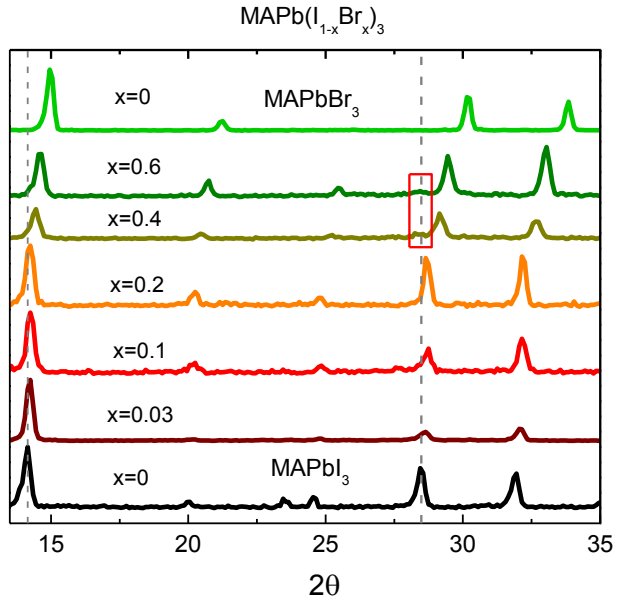

Fig 3.4 X-ray diffraction (XRD) patterns of a series of $MAPb(I_{1-x}Br_x)_3$ perovskite thin films with increasing Br content (x).

Initially, the perovskite diodes were characterized as solar cells. The incident photon to current efficiency, or photovoltaic external quantum efficiency (EQE_{pv}, Fig 3.5a) was determined by illuminating them with white-light halogen lamp in combination with bandpass filters. The EQE_{pv} was found to be high (0.7 - 0.8) in the visible range, although it decreased to 0.6 at wavelengths > 600 nm, due to a decrease of the perovskite absorption coefficient in that range. The onset on the spectral response lied in the near-infrared, between 750 and 800 nm for the pure $MAPbI_3$. When the amount of the bromide was increased, such onset shifted towards lower wavelengths, following the trend expected for the bandgap of the materials used. Interestingly, we observed a reduction of the EQE_{pv}, mainly in the range between 400 and 600 nm, and this loss was more severe for higher Br content (x = 0.4, 0.6), where the EQE_{pv} did not exceed 0.2. This discrepancy at the highest amounts of bromide was also observed in the XRD, where a minor but clear contribution of pure $MAPbI_3$ was detected.

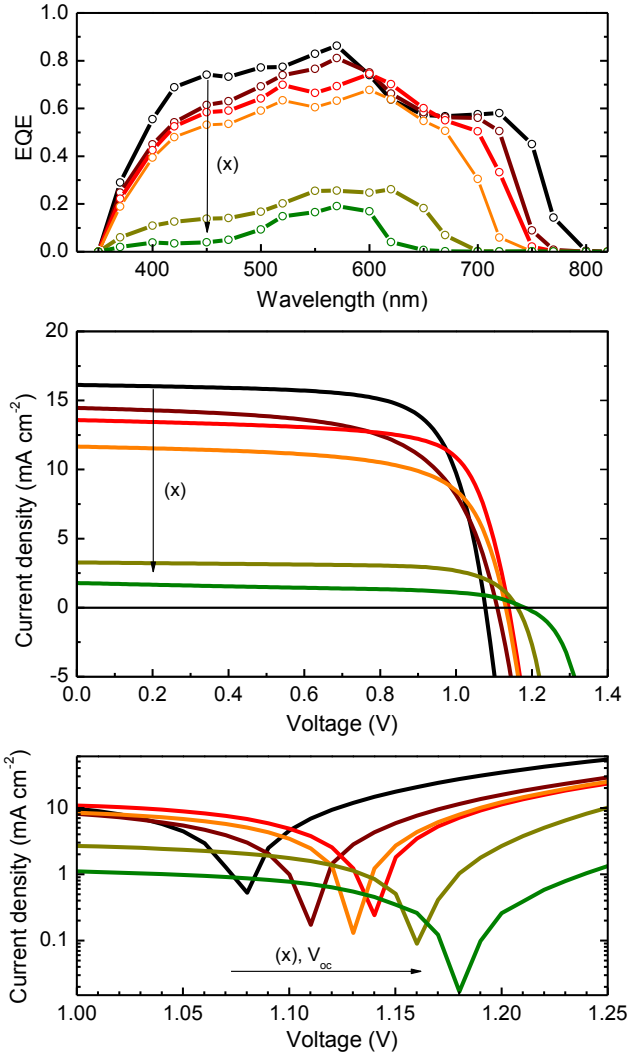

Fig 3.5 (a) EQE, (b) J-V curves under illumination, and (c) zoom on a log scale plot on the Voc for a series of solar cells using MAPb($I_{1-x}Br_x$)$_3$ perovskite with increasing content (x).

A similar trend was observed in the current density-voltage (*J-V*) characteristics under illumination (Fig 3.5b), whose main parameters are summarized in Table 1.

The short circuit current followed the trend observed in the EQE_{pv}, diminishing when the amount of bromide increased. On the other hand, the open-circuit voltage increased, going from 1079 mV for the perovskite cell

based on the pure iodide to 1182 mV for the device with the highest bromide concentration.

Table 1 Composition, optical and photovoltaic parameters for a series of solar cells based on $MAPbI_{(1-x}Br_x)_3$

$MAPbBr_3$ Thickness (nm)	$MAPb(I_{1-x}Br_x)_3$ x	E_g(eV)	V_{oc} (mV)	J_{sc} (mA/cm²)	*FF* (%)	*PCE* (%)
0	0	1.58	1079	16.34	73	12.9
20	0.03	1.61	1114	14.14	65	10.2
40	0.1	1.64	1139	13.14	72	10.8
60	0.2	1.70	1129	11.72	70	9.3
100	0.4	1.80	1175	3.01	71	2.5
200	0.6	1.92	1182	1.78	55	1.2

The trend in photovoltage is clearly visible in the plot in Fig 3.5c. The enhancement of the V_{oc} is a consequence of the larger bandgap when the content of bromide is increased. The fill factor, FF, of the different devices prepared was quite similar, decreasing drastically only for the device with x = 0.6. Again, this sudden drop is in line with the large reduction in the photocurrent. Finally, the PCE of the pure iodide perovskite cell was 12.9%, which was comparable with similar devices obtained with vacuum deposited perovskite and organic transport layers.[40] As already noticed, as the photocurrent diminished when the amount of bromide increased, the PCE of the mixed halide perovskite $MAPb(I_{1-x}Br_x)_3$ with $x \leq 0.2$ decreased, although the reduction in photocurrent was compensated with the augmented V_{oc}.

As a result, the device based on the mixed perovskite $MAPb(I_{0.8}Br_{0.2})_3$, with a bandgap of 1.70 eV, still maintained a rather high PCE of 9.3%. For the mixed halide perovskite with the highest concentrations of bromide (x = 0.4, 0.6) the PCE diminished drastically, due to the large decrease in photocurrent.

To further investigate these mixed perovskites, the devices prepared were characterized as light-emitting diodes (LEDs). In this case we used a

sensitive Si-photodiode coupled to an integrating sphere to monitor the electroluminescence of the device.

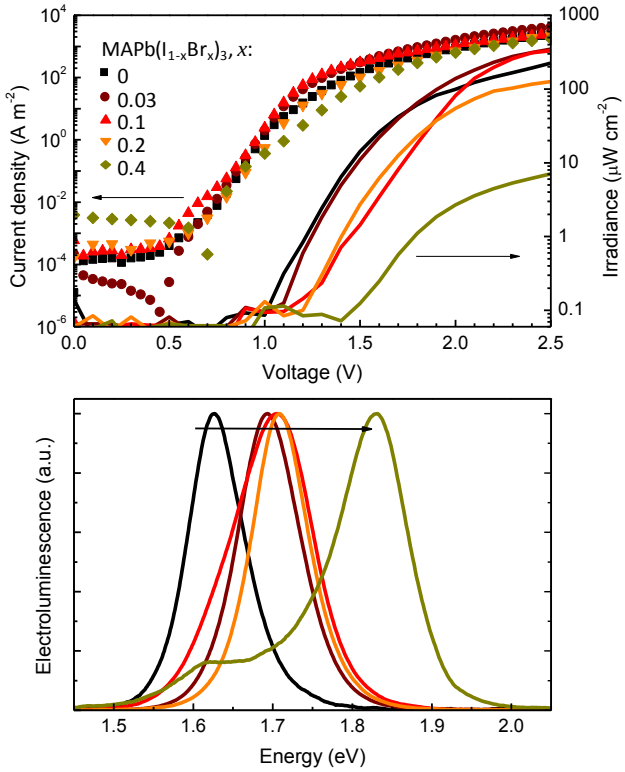

Fig 3.6 (a) Current density (left, symbols) and irradiance (right, lines) versus applied bias, (b) normalized electroluminescence spectra (the arrow indicates the blue shift for increasing Br content) for the mixed halide perovskite diode series.

In Fig 3.6a, the current density and the irradiance versus the applied voltage for the different devices is presented. As expected for the selected device layout, the current was governed by a low parasitical leakage current at very low voltages, with a transition to a steep increase of the current above approximately 0.5 V. After this, two regimes were identified. The first one is called diffusion dominated current, typically described by the Shockley diode equation.[85] Above the built-in potential at about 1.0 V, the current density curve is less steep, due to the establishment of a drift current, limited by either charge injection or the formation of a space charge. The

current density reached values higher than 1000 A/m^2 at 2.5 V, indicative of low carrier injection barriers and good charge transport in the diodes.

Intense electroluminescence was observed for all devices except for the ones with the highest amount of bromide. The turn-on voltage for the electroluminescence was found to be approximately 1 V for the $MAPbI_3$ based devices, similarly to literature reports.[86] The turn-on voltage of the electroluminescence increased with amount of bromide, reaching values close to 1.5 V. The emission spectra also shifted in energy when the content of bromide in the perovskite increased (Fig 3.6b). The emission could be tuned from 1.62 eV, the emission of the pure iodide perovskite, up to 1.83 eV for the $MAPb(I_{0.6}Br_{0.4})_3$. Interestingly, a second emission peak around 1.62 eV was observed in the spectra for the compound with x = 0.4, suggesting an incomplete conversion when a too thick $MAPbBr_3$ was used on top of the $MAPbI_3$. This residual $MAPbI_3$ phase did not contribute to the optical absorption but could be observed by carefully examining the diffraction pattern as minor peaks at 2θ of 28 - 30º. These minor peaks were present in the diffraction of the mixed perovskites with the highest concentration of bromide (Fig 3.4). The presence of a residual iodide-rich phase at high bromide content might enhance the carrier recombination and is likely responsible for the low performance of the solar cells and the inefficient electroluminescence.

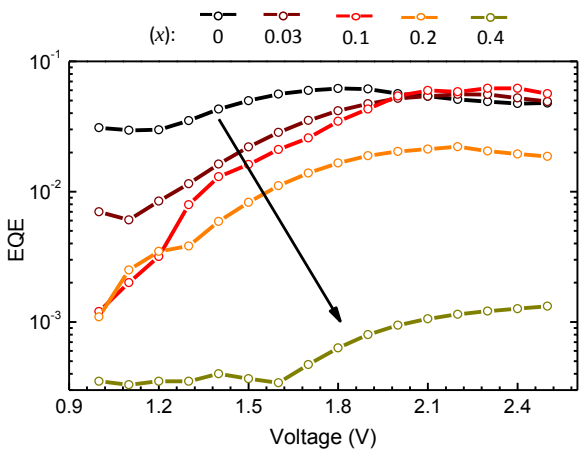

Fig 3.7 External quantum efficiency (EQE) for the electroluminescence versus applied voltage of a series of diodes employing $MAPb(I_{1-x}Br_x)_3$ as the active material.

The maximum EQE for electroluminescence (EQE_{EL}) of the diodes was found to be 0.06 % when the pure iodide was employed, while it decreased slightly when the amount of bromide increased (Fig 3.7*)*.

The ideality factors were calculated in order to obtain further information on these mixed halide perovskite devices. The ideality factor of a diode is a measure of how closely the diode follows the ideal diode equation:

$$J = J_0 \left[exp\left(\frac{qV}{\eta KT}\right) - 1 \right] \qquad \text{Equation 4}$$

Where J_0 is the saturation current density, η is the ideality factor, K the Boltzmann constant and T the temperature. The ideality factor is a measure of the slope of the J-V characteristics on a semi-logarithmic plot and can be determined by differentiation according to equation 4:

$$\eta = \left(\frac{KT}{q}\frac{\partial lnJ}{\partial V}\right)^{-1} \qquad \text{Equation 5}$$

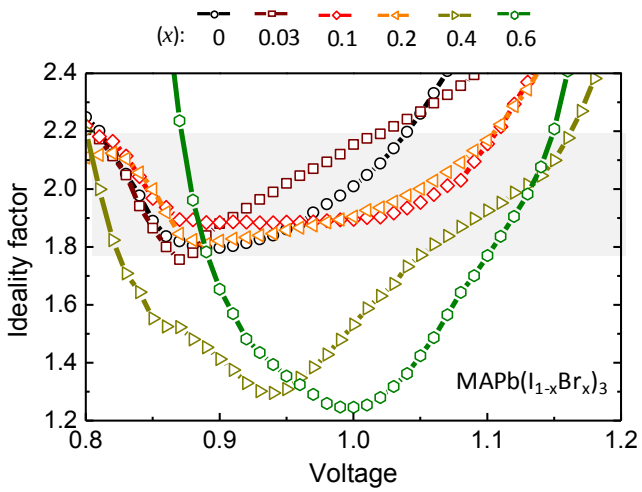

Fig 3.8 Calculated ideality factors for diodes based on $MAPb(I_{1-x}Br_x)_3$ with increasing Br content.

We calculated the ideality factors from the dark diffusion current below the built-in voltage, which varies in the range of 1 to 1.2 V. The ideality factor

can be estimated from the plateau of the curve in Fig 3.8. We found values of about 1.8 - 2 for the devices based on the pure iodide and for those employing mixed-halide perovskite with bromide concentration ≤ 0.2.

Interestingly, the ideality factor for the devices with the highest amount of bromide (x= 0.4, 0.6) was lower, about 1.2 - 1.3. In the absence of recombination, the ideal diode equation should apply, where the ideality factor should be 1. This is also the case for direct recombination, whereas trap-assisted recombination can change the ideality factor up to a value of 2. So, trap-assisted recombination appears to be the main recombination pathway in the pure iodide and the mixed halide perovskite with $x \leq 0.2$. For the devices with higher concentration of bromide, the residual $MAPbI_3$ phase might enhance the direct free-carrier recombination as a consequence of its lower bandgap, lowering the corresponding ideality factors.
The trend observed for the materials synthesized in this work could be ascribed to the phase segregation in mixed halide perovskites at high bromide content. In particular, such segregation would result in the formation of a minority phase with a lower bandgap (iodide-rich perovskite) within the majority phase. The photo-excited charge carriers can easily be trapped in the low-bandgap minority phase, undermining the photovoltaic efficiency.[21, 82, 87]

3.5. Conclusion

Mixed iodide-bromide methylammonium lead perovskites were prepared with a novel method involving vacuum-based processes and interdiffusion of two stacked perovskite films. The composition of the final compound was controlled by the thickness of the $MAPbBr_3$ deposited on top of the $MAPbI_3$. A perovskite with a bandgap of 1.7 eV was prepared, which is particularly interesting as a top cell for a tandem configuration with Si or CIGS cells. Increasing open-circuits was observed with solar cells with large Br content, as well as bright electroluminescence and tunable emission bands when the same devices were operated in forward bias. We observed a strong decrease in performance for the devices employing perovskites with

bromide content above x > 0.2, due to the presence of a residual $MAPbI_3$ phase. This minority phase was likely to enhance the direct charge recombination within these domains.

3.6. Contribution of the author

L. Gil-Escrig, A. Miquel-Sempere; M. Sessolo; H. J. Bolink. “Mixed Iodide-Bromide Methylammonium Lead Perovskite-based Diodes for Light Emission and Photovoltaics” J. Phys. Chem. Lett. 6, 3743−3748 (2015).

THE JOURNAL OF PHYSICAL CHEMISTRY Letters

Letter

pubs.acs.org/JPCL

Mixed Iodide–Bromide Methylammonium Lead Perovskite-based Diodes for Light Emission and Photovoltaics

Lidón Gil-Escrig, Araceli Miquel-Sempere, Michele Sessolo, and Henk J. Bolink*

Instituto de Ciencia Molecular (ICMOL), Universidad de Valencia, Calle Catedrático José Beltrán, 2, 46980 Paterna, Valencia, Spain

Supporting Information

ABSTRACT: Vacuum deposition techniques are used to prepare mixed iodide–bromide methylammonium lead perovskite diodes via an intermediate double layer of the pure iodide and bromide perovskites. The diodes lead to bright electroluminescence, whose emission spectra maxima shift from the infrared toward the visible with increasing bromide content. When illuminated with AM1.5 simulated sunlight the devices function as efficient solar cells with power conversion efficiencies as high as 12.9%.

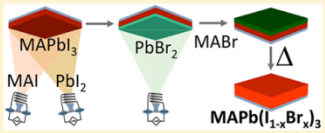

Organic–inorganic (hybrid) lead halide perovskites have recently become a self-standing, wide research field thanks to the demonstration of solar cells with rapidly increasing power conversion efficiencies (PCEs), now exceeding 20%.[1−3] The interest toward these materials arises from the possibility of processing them into thin films by simple solution or vacuum techniques, which might lead to efficient and inexpensive photovoltaic devices. Hybrid perovskites have a wide spectrum of desirable properties; they are direct bandgap semiconductors with very high absorption coefficients, high and balanced hole and electron mobility, and large charge diffusion length.[4−9] A unique feature of these materials is their versatility in terms of bandgap energy (E_g), which can be tuned by simple exchange of their components. The most studied compound in photovoltaics, the methylammonium lead iodide ($MAPbI_3$), has an optical bandgap of about 1.55 eV. The $MAPbI_3$ bandgap can be narrowed by exchanging methylammonium with formamidinium, leading to a better solar spectrum matching and thus enhanced photocurrent when the compounds is used as absorber in a solar cell.[3,4,10] In other applications, it might be desirable to increase the bandgap of the perovskite. Partial and complete substitution of the iodide, first with bromide and then with chloride, allows to continuously widen the bandgap up to about 3.2 eV, which correspond to the fully substituted $MAPbCl_3$.[11] The use of different alkyl and phenyl ammonium halides also modifies the bandgap of the resulting 2 or 3D perovskite.[12] These mixed alkyl-ammonium halide perovskites have been especially studied for applications in light-emitting devices because their bandgaps and the correspondent electroluminescence span the whole visible spectrum.[13−16] The $MAPbBr_3$ perovskite, with a bandgap of ∼2.3 eV, has been used as absorber in solar cells and leads to a high photovoltage.[17,18] Through proper selection of the charge-transporting layers, open-circuit voltages (V_{oc}) up to 1.5 V and PCEs exceeding 10% have been demonstrated.[19] The bandgap flexibility and the high V_{oc} of perovskite solar cells make them good candidates to be integrated with Si or CIGS cells in tandem architectures.[20,21] Importantly, the ideal bandgap for a top cell in a tandem configuration with Si (E_g = 1.12 eV) and CIGS (E_g = 1.15 eV) lies in the range from 1.70 to 1.75 eV,[22] which can be achieved by partial bromide substitution into the $MAPbI_3$ system.[23,24] To reach this goal, mixed $MAPb(I_{1-x}Br_x)_3$ perovskites with different Br content (x) are the most promising materials, and these have been studied as the light absorber in solar cells.[23,25−27] In most cases the I/Br stoichiometry was controlled by varying the relative concentrations of the halides precursors in solution. It is well known from the vast available literature on $MAPbI_3$ solar cells that the degree and nature of the perovskite crystallinity have a strong effect on the photophysical properties of the material.[28] Because the thin-film morphology is controlled by the precursors reaction kinetics,[29] several solution-processing methods have been proposed so far.[30] Among these, the sequential deposition has been widely applied because the formation of the inorganic lead halide framework is decoupled from the reaction and intercalation with the ammonium halide.[31] Physical vapor deposition methods for the hybrid perovskites have also emerged, leading to high-efficiency photovoltaic devices.[32−34] Such techniques have intrinsic advantages over solution-based methods, such as high purity, compatibility with large area, and fine control over film thickness and morphology. Importantly, vacuum methods are additive, meaning that multilayer devices can be built without chemical modifications of the underlying layers. Mixed deposition route, where the lead halide is deposited by vacuum deposition and converted to perovskite in solution, has also been demonstrated.[35,36]

Here a novel method to prepare mixed $MAPb(I_{1-x}Br_x)_3$ perovskite with different Br content (x) is presented. The method consists in merging of two stacked perovskite layers, each having its own composition and phase. To prepare the perovskite double layer, vacuum-based deposition techniques are employed. The deposition of the $MAPbI_3$ film is done by

Received: August 6, 2015
Accepted: September 2, 2015
Published: September 2, 2015

DOI: 10.1021/acs.jpclett.5b01716
J. Phys. Chem. Lett. 2015, 6, 3743−3748

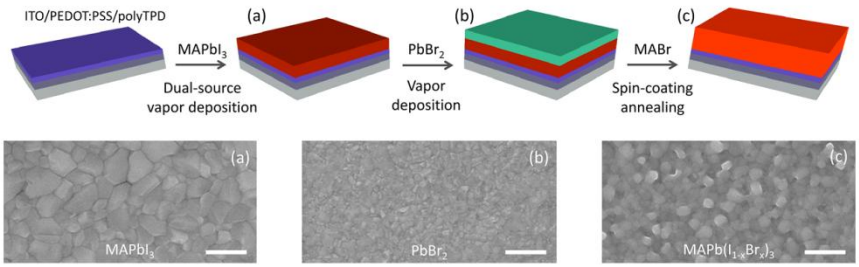

Figure 1. On the top, process schematics with the deposition steps used to prepare the $MAPb(I_{1-x}Br_x)_3$ thin film series and, on the bottom, the correspondent evolution of the surface morphology as monitored by scanning electron microscopy (SEM, scale bar 500 nm).

dual-source vapor deposition, followed by the evaporation of a $PbBr_2$ layer. The latter is then converted to perovskite upon exposure to MABr. When this bilayer is annealed, halide interdiffusion takes place, producing the $MAPb(I_{1-x}Br_x)_3$ phase.[37,38] The Br content and hence the bandgap is controlled by changing the thickness of the top $MAPbBr_3$ perovskite. p-i-n-type diodes were prepared by depositing the perovskite bilayers on top of a hole transporting polymer and covering them with an electron-transporting material and a suitable metal electrode. These perovskite devices have been characterized as both light-emitting diodes and solar cells.[39] When used as light-emitting diodes the electroluminescent spectrum blue-shifts with increasing x as a consequence of the wider bandgap of the perovskite. Under 1 sun illumination these diodes work as solar cells with PCEs ranging from 9.2 to 12.9%. The conversion of the $MAPbI_3$ to mixed $MAPb(I_{1-x}Br_x)_3$ works quantitatively up to a $MAPbBr_3$ thickness of 60 nm. Above that limit, the conversion is not complete and free-carrier recombination occurs, as inferred from examining the diode ideality factors, diminishing the device performances.

Details of materials, thin-film deposition, device preparation, and characterization are provided in the Supporting Information. Briefly, ITO/glass substrates were coated with a 70 nm thick film of poly(3,4-ethylenedioxythiophene) doped with poly(styrene sulfonic acid) (PEDOT:PSS) and a thin layer (20 nm) of poly(*N*,*N*′-bis(4-butylphenyl)-*N*,*N*′-bis(phenyl)-benzidine) (polyTPD) functioning as the hole-transporting and electron-blocking layer. A scheme of the perovskite preparation process is reported in Figure 1. Substrates were transferred into a high vacuum chamber where a 300 nm thick $MAPbI_3$ perovskite film was deposited by dual-source vapor deposition. The surface morphology of the $MAPbI_3$ layer is compact and homogeneous (Figure 1a), composed of grains with size on the order of 100−500 nm. The root-mean-square (RMS) roughness of the sample is 22.11 nm. (See Figure S1 in the Supporting Information for the atomic force microscopy characterization.)

Without breaking the vacuum, thin films of $PbBr_2$ with different thicknesses were deposited on top. The morphology of the $PbBr_2$ layers deposited on top of the $MAPbI_3$ is very different from that of the $MAPbI_3$ (Figure 1b); they are smooth (RMS roughness = 8.68 nm) and are composed of very small (<50 nm), densely packed nanocrystallites. The morphology closely resembles that observed for evaporated thin (<50 nm) films of PbI_2.[35] Conversion to the $MAPbBr_3$ perovskite was performed by spin-coating an isopropanol solution of MABr on top of the $PbBr_2$ films. Optical absorption confirmed the formation of the high bandgap perovskite even without any heat treatment (Figure S2 in the Supporting Information). Upon annealing at 100 °C for 5 min, the $MAPbI_3$/$MAPbBr_3$ bilayers were converted to the mixed $MAPb(I_{1-x}Br_x)_3$ perovskite. The resulting film surface (Figure 1c) is composed of block-like closely packed crystals, with a slightly increased roughness (RMS = 23.01 nm), in agreement with previous reports on the conversion of vapor-deposited PbI_2 films to its correspondent perovskites.[35,40] The formation of mixed $MAPb(I_{1-x}Br_x)_3$ perovskites was monitored using optical absorption (Figure 2a). As the thickness of the top-deposited $MAPbBr_3$ layer is increased, the onset of the absorption blue shifts with respect to the pure $MAPbI_3$ (1.58 eV), and the correspondent bandgap progressively widens, as represented in Figure 2b.

In particular, the bandgap for $MAPb(I_{1-x}Br_x)_3$ films obtained with 20, 40, and 60 nm thick $MAPbBr_3$ were found to be 1.61,

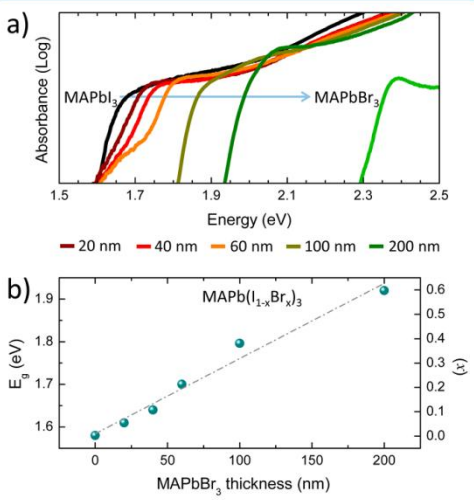

Figure 2. (a) Optical absorption spectra for a series of $MAPb(I_{1-x}Br_x)_3$ perovskite films prepared with increasing thickness of the $MAPbBr_3$ layer. The absorption spectra of the pure $MAPbI_3$ and $MAPbBr_3$ (black and light green, respectively) are included as references. (b) Variation of the optical bandgap for the same series of $MAPb(I_{1-x}Br_x)_3$ films, with the estimated Br content (right axis).

DOI: 10.1021/acs.jpclett.5b01716
J. Phys. Chem. Lett. 2015, 6, 3743−3748

Table 1. Composition, Optical, and Photovoltaic Parameters for a Series of Solar Cells Based on $MAPb(I_{1-x}Br_x)_3$ and for Increasing Br Content (x)[a]

$MAPbBr_3$ thickness (nm)	$MAPb(I_{1-x}Br_x)_3$ x	E_g (eV)	V_{oc} (mV)	J_{sc} (mA/cm^2)	FF (%)	PCE (%)
0	0	1.58	1079	16.34	73	12.9
20	0.03	1.61	1114	14.14	65	10.2
40	0.1	1.64	1139	13.14	72	10.8
60	0.2	1.70	1129	11.72	70	9.3
100	0.4	1.80	1175	3.01	71	2.5
200	0.6	1.92	1182	1.78	55	1.2

[a]Bromide concentration in $MAPb(I_{1-x}Br_x)_3$, x, bandgap energy, E_g, open circuit voltage, V_{oc}, short-circuit current density, J_{sc}, fill factor, FF, and power conversion efficiency, PCE.

1.64, and 1.70, respectively. Interestingly, the onset of the absorption for these samples is not as steep as for the other materials, which points to an augmented disorder in the film as a consequence of the iodide/bromide interdiffusion.[41] Film prepared by interdiffusion of a $MAPbBr_3$ layer with thicknesses of 100 and 200 nm showed a much steeper absorption onset and bandgap energies of 1.80 and 1.92 eV, respectively. The variation of the bandgap is accompanied by a shift of the XRD signal to higher angles in the 28−31° 2θ range, in agreement with a transition from the tetragonal ($MAPbI_3$) to the cubic ($MAPbBr_3$) phase (Figure S3 in the Supporting Information).[23] In Table 1, the series of samples with the correspondent bandgap energy and the stoichiometric fraction of bromide, estimated comparing the absorption onset with literature values, are reported.[23,24]

As previously mentioned, the synthesized materials are very interesting as light absorber in top cells of tandem devices or as light-emitting layers in LEDs. p-i-n type diodes were obtained by depositing a thin (40 nm) layer of [6,6]-phenyl-C_{61}-butyric acid methyl ester (PCBM) as the electron transport material, capped with a double layer (Ba/Ag) low work function electrode. To monitor the electroluminescence of the diodes using the series of mixed perovskites as previously described, we used a sensitive Si-photodiode coupled to an integrating sphere to obtain the irradiance of the device.

In Figure 3a, the current density and irradiance as a function of the applied bias for devices with increasing Br content is presented. The leakage current is low, indicating the preparation of high-quality diodes for the whole series of devices. A deviation from the leakage current occurs around 0.5 V, after which two regimes can be identified. First, an almost linear increase (in the log scale plot) is present, followed by a slower increase at higher voltages. The first regime is due to a diffusion current, whereas the second regime is where injection or space-charge is limiting the current increase.[42] Eventually, the current density reaches values higher than 1000 A/m^2 at 2.5 V, indicative of low carrier injection barriers and good charge transport in the diodes. Intense electroluminescence was observed for all, but one, of the diodes studied. The turn-on voltage for the electroluminescence was found to be as low as 1 V for the $MAPbI_3$-based devices, similar as previously reported.[13,16,39] With increasing Br content of the mixed perovskite, the turn-on voltage for light-emission increases, reaching 1.5 V for the diode based on the perovskite with the highest Br content. The emission spectrum maxima of the diodes reduces in wavelength (increases in energy), with increasing Br content in the mixed perovskite used, in line with the trend observed from optical absorption measurements. The emission can be tuned from 1.62 eV, corresponding to the pure iodide compound, up to 1.83 eV for the $MAPb(I_{0.6}Br_{0.4})_3$. Even though the electroluminescence spectra could be obtained, as just described, no photoluminescence could be observed when the perovskite films were excited with a xenon lamp. This implies that the photoluminescence quantum yield (PLQY) is very low for these films, at least at low excitation energy.[43] The maximum EQE for electroluminescence (EQE_{EL}) of the diodes was found to be ∼0.06% when the pure $MAPbI_3$ was employed, while it decreased slightly when perovskite with increasing Br content was used (Figure S4 of the Supporting Information). This EQE_{EL} is in the same range as those reported previously for similar diodes.[13,16,39] The electroluminescence spectrum of the diode consisting of the $MAPb(I_{0.4}Br_{0.6})_3$ perovskite contains a low-energy component, indicative of a residual $MAPbI_3$ phase in the material. Such a phase, although not observed by optical absorption, can be observed by carefully examining the 2θ diffraction pattern as minor peaks at angles of 28−30°. These diffraction peaks are present for both $MAPb(I_{0.6}Br_{0.4})_3$ and $MAPb(I_{0.4}Br_{0.6})_3$ (Figure S3, Supporting Information). The presence of a residual, separate pure iodide-rich phase might enhance carrier recombination and thus be responsible for both the low leakage currents and low electroluminescence observed for these diodes. To investigate the origin of the reduced performances of the diodes based on high Br content perovskites, we calculated the ideality factors from the dark diffusion current below the built-in voltage, which is ∼1 V for this set of samples. The ideality factor can be determined from the plateau in Figure 3c[44] and was found to have values between 1.8 and 2.0 for the devices based on the pure $MAPbI_3$ and for the mixed perovskites with low Br content ($x \leq 0.2$). The deviation from unity of the ideality factor has been previously observed in hybrid perovskites, and it is associated with nonradiative trap-assisted recombination as the main recombination pathway.[42] Interestingly, the ideality factor for the diodes employing $MAPb(I_{0.6}Br_{0.4})_3$ and $MAPb(I_{0.4}Br_{0.6})_3$ is substantially lower, indicating that either trap-assisted recombination is somehow reduced or that other recombination processes become more relevant in these materials.[44] From one side, the presence of a residual $MAPbI_3$ phase in these compounds might enhance direct free-carrier recombination as a consequence of the lower bandgap of the pure iodide domains. On the contrary, when comparing the pure $MAPbI_3$ and $MAPbBr_3$, the valence band maximum (VBM) shifts from −5.4 to −5.9 eV.[45] Hence, the energy difference between the perovskite VBM and the HOMO of the hole blocking material (here PCBM, with HOMO at about −5.9/−6.0 eV from vacuum level) is progressively reduced when increasing the Br content. In the extreme case of the pure $MAPbBr_3$, such energy difference is virtually zero and thus enhanced direct charge recombination at the $MAPbBr_3$/PCBM interface or even in the PCBM layer can occur. This phenomena would also explain the

DOI: 10.1021/acs.jpclett.5b01716
J. Phys. Chem. Lett. 2015, 6, 3743−3748

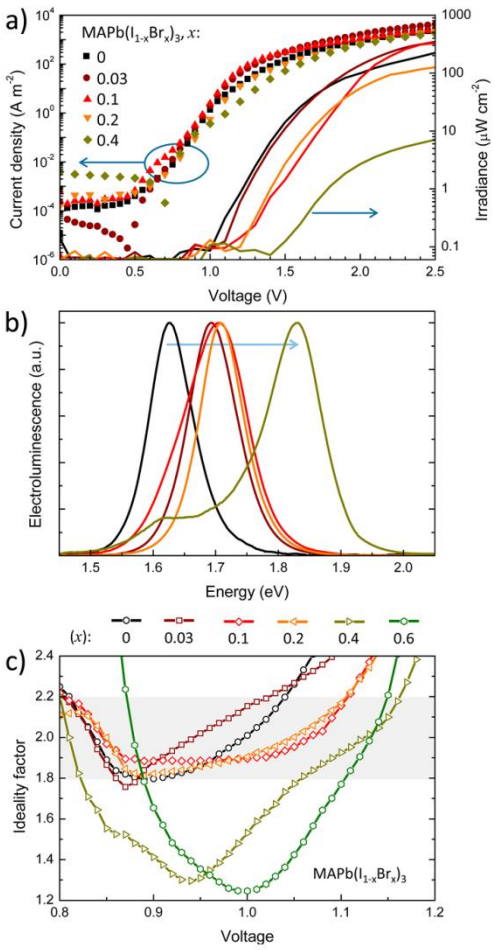

Figure 3. (a) Current density (left, symbols) and irradiance (right, lines) versus applied bias, (b) electroluminescence spectra normalized to [0, 1] (the arrow indicates the blue shift for increasing Br content), and (c) calculated ideality factors for diodes based on $MAPb(I_{1-x}Br_x)_3$ with increasing Br content (x). The device structure is ITO/PEDOT:PSS (70 nm)/polyTPD(20 nm)/$MAPb(I_{1-x}Br_x)_3$ (300 nm + thickness of the top $MAPbBr_3$ perovskite used, see Table 1)/PCBM (40 nm)/Ba (10 nm)/Ag (100 nm).

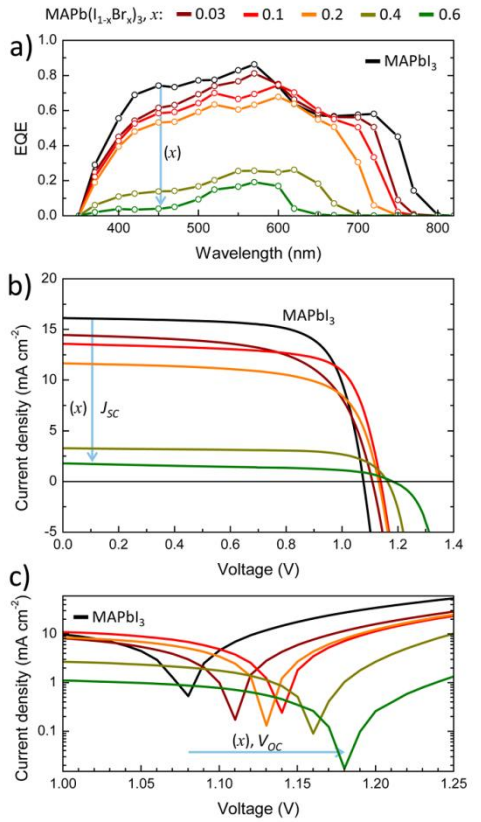

Figure 4. (a) EQE, (b) $J-V$ curves under illumination, and (c) zoom on a log scale plot on the V_{oc} for a series of solar cells using $MAPb(I_{1-x}Br_x)_3$ perovskite with increasing Br content (x). The device structure is ITO/PEDOT:PSS (70 nm)/polyTPD(20 nm)/$MAPb(I_{1-x}Br_x)_3$ (300 nm + thickness of the top $MAPbBr_3$ perovskite used, see Table 1)/PCBM (40 nm)/Ba (10 nm)/Ag (100 nm).

ideality factor of approximately 1 and justify the lower EQE_{EL} observed for devices with high Br-content perovskites.

The same diodes as previously described were also characterized as solar cells. The incident photon to current efficiency, or photovoltaic external quantum efficiency (EQE_{pv}, Figure 4a) of the diodes, was determined by illuminating them with a white-light halogen lamp in combination with interference filters. The EQE_{pv} of the device employing the pure $MAPbI_3$ is high (0.7 to 0.8) in the visible range, while it diminishes at wavelengths >600 nm, where the perovskite is weakly absorbing ($EQE_{pv} \approx 0.6$). The onset of the spectral response lies in the near-infrared, between 750 and 800 nm. The measured EQE_{pv} for the different cells follows the trend expected for the bandgaps of the materials used. Compared with the pure $MAPbI_3$, the onset of the spectral response shifts toward lower wavelengths with increasing bromide content, that is, for wider bandgaps, as was shown previously for cells using solution-processed perovskite from mixed halogen precursors.[23] At the same time, we observed a reduction of the EQE values in the 400−600 nm spectral range. This phenomena is more profound for the solar cells employing $MAPb(I_{1-x}Br_x)_3$ with high Br content (x = 0.4, 0.6), for which the photocurrent onset is shifted to ∼650 nm. Unfortunately, this shift is accompanied by a drastic reduction of the EQE over the full visible spectrum, with a maximum EQE of ∼0.2 for both cells. The rather different behavior of the diodes using the perovskite prepared from the two thickest $MAPbBr_3$ layers is in line with what was observed in electroluminescence and dark current behavior.

DOI: 10.1021/acs.jpclett.5b01716
J. Phys. Chem. Lett. 2015, 6, 3743−3748

The same trend in diode performance is observed from the current density−voltage (J−V) characterization under illumination, as reported in Figure 4b. The critical photovoltaic parameters are summarized in Table 1. The short-circuit current density (J_{sc}) of the solar cells follows the trend observed in the EQE, diminishing with increasing bromide content. At the same time, however, an increase in the open-circuit voltage (V_{oc}) is observed, going from 1079 mV for the device based on the pure $MAPbI_3$ up to 1182 mV for the solar cell using $MAPb(I_{0.4}Br_{0.6})_3$ as the absorber. (The trend in the V_{oc} is more clearly observed in the logarithmic plot in Figure 4c.) The PCE of the pure $MAPbI_3$ is 12.9%, comparable to state-of-the-art vacuum deposited p-i-n solar cells with perovskite films of comparable thickness (here 300 nm).[34,46] For low Br content ($x \leq 0.2$), the photocurrent is diminished compared with that of the cells using the pure iodide perovskite, but the reduction in the photocurrent is partially compensated by the increase in V_{oc}. As a result, the device employing the mixed $MAPb(I_{0.8}Br_{0.2})_3$ perovskite, with a bandgap of 1.7 eV, which is suitable for tandem photovoltaics, still maintains a high PCE of 9.3%. Despite the augmented photovoltage, the low photocurrent measured for devices employing $MAPb(I_{1-x}Br_x)_3$ with higher Br content leads to efficiencies as low as 2.5% ($x = 0.4$) and 1.2% ($x = 0.6$). The observed trend with a drastic reduction of the PCE when increasing the Br content in the perovskite absorber has been previously reported.[23,26]

In general, the enhanced V_{oc} does not compensate for the reduction in photocurrent, which is a consequence of the larger bandgap and mismatch with the solar spectrum. In our case, however, the reduction of the EQE for Br content $x \geq 0.4$ is too severe, especially considering the sample thickness (400 nm for $x = 0.4$ and 500 nm for $x = 0.6$). As mentioned in the discussion of the electroluminescence properties of these diodes, two factors are likely hindering a proper device functioning at high Br content: (i) the noncomplete conversion when using too thick top $MAPbBr_3$ layers and (ii) a reduced energy barrier for holes at the perovskite/PCBM interfaces, leading to enhanced quenching of excitons.

In summary, mixed iodide−bromide methylammonium lead perovskite were prepared through vacuum-based processes using interdiffusion of components from the two pure starting layers. The composition of the final material is controlled by the respective starting layer thicknesses, which works well up to an iodide/bromide ratio of 4:1, leading to a perovskite material with a bandgap of 1.70 eV. Vacuum-processed perovskites with this bandgap are particularly interesting as top cells in tandem configurations with Si or CIGS cells. Simple diodes are prepared that lead to bright electroluminescence with tunable emission bands, in line with the perovskite composition. The same diodes also work as efficient solar cells when illuminated, leading to an increased open-circuit voltages for increasing bromide content as a result of the larger bandgap.

■ ASSOCIATED CONTENT

Supporting Information

The Supporting Information is available free of charge on the ACS Publications website at DOI: 10.1021/acs.jpclett.5b01716.

Materials and methods, AFM characterization, optical absorption for as-deposited $MAPbBr_3$ thin films, and XRD characterization. (PDF)

■ AUTHOR INFORMATION

Corresponding Author

*E-mail: henk.bolink@uv.es.

Notes

The authors declare no competing financial interest.

■ ACKNOWLEDGMENTS

This work has been supported by the Spanish Ministry of Economy and Competitiveness (MAT2014-55200 and FAFOR) and by the Generalitat Valenciana (Prometeo/2012/053).

■ REFERENCES

(1) Kojima, A.; Teshima, K.; Shirai, Y.; Miyasaka, T. Organometal Halide Perovskites as Visible-Light Sensitizers for Photovoltaic Cells. *J. Am. Chem. Soc.* **2009**, *131*, 6050−6051.

(2) Lee, M. M.; Teuscher, J.; Miyasaka, T.; Murakami, T. N.; Snaith, H. J. Efficient Hybrid Solar Cells Based on Meso-Superstructured Organometal Halide Perovskites. *Science* **2012**, *338*, 643−647.

(3) Yang, W. S.; Noh, J. H.; Jeon, N. J.; Kim, Y. C.; Ryu, S.; Seo, J.; Seok, S. I. High-Performance Photovoltaic Perovskite Layers Fabricated through Intramolecular Exchange. *Science* **2015**, *348*, 1234−1237.

(4) Stoumpos, C. C.; Malliakas, C. D.; Kanatzidis, M. G. Semiconducting Tin and Lead Iodide Perovskites with Organic Cations: Phase Transitions, High Mobilities, and Near-Infrared Photoluminescent Properties. *Inorg. Chem.* **2013**, *52*, 9019−9038.

(5) Stranks, S. D.; Eperon, G. E.; Grancini, G.; Menelaou, C.; Alcocer, M. J. P.; Leijtens, T.; Herz, L. M.; Petrozza, A.; Snaith, H. J. Electron-Hole Diffusion Lengths Exceeding 1 Micrometer in an Organometal Trihalide Perovskite Absorber. *Science* **2013**, *342*, 341−344.

(6) Gonzalez-Pedro, V.; Juarez-Perez, E. J.; Arsyad, W.-S.; Barea, E. M.; Fabregat-Santiago, F.; Mora-Sero, I.; Bisquert, J. General Working Principles of $CH_3NH_3PbX_3$ Perovskite Solar Cells. *Nano Lett.* **2014**, *14*, 888−893.

(7) Yin, W.-J.; Shi, T.; Yan, Y. Unique Properties of Halide Perovskites as Possible Origins of the Superior Solar Cell Performance. *Adv. Mater.* **2014**, *26*, 4653−4658.

(8) Dong, Q.; Fang, Y.; Shao, Y.; Mulligan, P.; Qiu, J.; Cao, L.; Huang, J. Electron-Hole Diffusion Lengths > 175 μm in Solution-Grown $CH_3NH_3PbI_3$ Single Crystals. *Science* **2015**, *347*, 967−970.

(9) Shi, D.; Adinolfi, V.; Comin, R.; Yuan, M.; Alarousu, E.; Buin, A.; Chen, Y.; Hoogland, S.; Rothenberger, A.; Katsiev, K.; et al. Low Trap-State Density and Long Carrier Diffusion in Organolead Trihalide Perovskite Single Crystals. *Science* **2015**, *347*, 519−522.

(10) Eperon, G. E.; Stranks, S. D.; Menelaou, C.; Johnston, M. B.; Herz, L. M.; Snaith, H. J. Formamidinium Lead Trihalide: a Broadly Tunable Perovskite for Efficient Planar Heterojunction Solar Cells. *Energy Environ. Sci.* **2014**, *7*, 982−988.

(11) Xing, G.; Mathews, N.; Lim, S. S.; Yantara, N.; Liu, X.; Sabba, D.; Grätzel, M.; Mhaisalkar, S.; Sum, T. C. Low-Temperature Solution-Processed Wavelength-Tunable Perovskites for Lasing. *Nat. Mater.* **2014**, *13*, 476−480.

(12) Mitzi, D. B.; Chondroudis, K.; Kagan, C. R. Organic-Inorganic Electronics. *IBM J. Res. Dev.* **2001**, *45*, 29−45.

(13) Tan, Z. K.; Moghaddam, R. S.; Lai, M. L.; Docampo, P.; Higler, R.; Deschler, F.; Price, M.; Sadhanala, A.; Pazos, L. M.; Credgington, D.; et al. Bright Light-Emitting Diodes Based on Organometal Halide Perovskite. *Nat. Nanotechnol.* **2014**, *9*, 687−692.

(14) Kumawat, N. K.; Dey, A.; Narasimhan, K. L.; Kabra, D. Near Infrared to Visible Electroluminescent Diodes Based on Organometallic Halide Perovskites: Structural and Optical Investigation. *ACS Photonics* **2015**, *2*, 349−354.

(15) Kumawat, N. K.; Dey, A.; Kumar, A.; Gopinathan, S. P.; Narasimhan, K. L.; Kabra, D. Band Gap Tuning of CH_3NH_3Pb-

DOI: 10.1021/acs.jpclett.5b01716
J. Phys. Chem. Lett. 2015, 6, 3743−3748

$(Br_{1-x}Cl_x)_3$ Hybrid Perovskite for Blue Electroluminescence. *ACS Appl. Mater. Interfaces* **2015**, *7*, 13119−13124.
(16) Kim, Y.-H.; Cho, H.; Heo, J. H.; Kim, T.-S.; Myoung, N.; Lee, C.-L.; Im, S. H.; Lee, T.-W. Multicolored Organic/Inorganic Hybrid Perovskite Light-Emitting Diodes. *Adv. Mater.* **2015**, *27*, 1248−1254.
(17) Edri, E.; Kirmayer, S.; Cahen, D.; Hodes, G. High Open-Circuit Voltage Solar Cells Based on Organic−Inorganic Lead Bromide Perovskite. *J. Phys. Chem. Lett.* **2013**, *4*, 897−902.
(18) Cai, B.; Xing, Y.; Yang, Z.; Zhang, W.-H.; Qiu, J. High Performance Hybrid Solar Cells Sensitized by Organolead Halide Perovskites. *Energy Environ. Sci.* **2013**, *6*, 1480−1485.
(19) Heo, J. H.; Song, D. H.; Im, S. H. Planar $CH_3NH_3PbBr_3$ Hybrid Solar Cells with 10.4% Power Conversion Efficiency, Fabricated by Controlled Crystallization in the Spin-Coating Process. *Adv. Mater.* **2014**, *26*, 8179−8183.
(20) Snaith, H. J. Perovskites: The Emergence of a New Era for Low-Cost, High-Efficiency Solar Cells. *J. Phys. Chem. Lett.* **2013**, *4*, 3623−3630.
(21) Bailie, C. D.; Christoforo, M. G.; Mailoa, J. P.; Bowring, A. R.; Unger, E. L.; Nguyen, W. H.; Burschka, J.; Pellet, N.; Lee, J. Z.; Gratzel, M.; et al. D. Semi-Transparent Perovskite Solar Cells for Tandems with Silicon and CIGS. *Energy Environ. Sci.* **2015**, *8*, 956−963.
(22) Coutts, T. J.; Emery, K. A.; Scott Ward, J. Modeled Performance of Polycrystalline Thin-Film Tandem Solar Cells. *Prog. Photovoltaics* **2002**, *10*, 195−203.
(23) Noh, J. H.; Im, S. H.; Heo, J. H.; Mandal, T. N.; Seok, S. I. Chemical Management for Colorful, Efficient, and Stable Inorganic-Organic Hybrid Nanostructured Solar Cells. *Nano Lett.* **2013**, *13*, 1764−1769.
(24) Hoke, E. T.; Slotcavage, D. J.; Dohner, E. R.; Bowring, A. R.; Karunadasa, H. I.; McGehee, M. D. Reversible Photo-Induced Trap Formation in Mixed-Halide Hybrid Perovskites for Photovoltaics. *Chem. Sci.* **2015**, *6*, 613−617.
(25) Zhao, Y.; Zhu, K. Efficient Planar Perovskite Solar Cells Based on 1.8 eV Band Gap $CH_3NH_3PbI_2Br$ Nanosheets via Thermal Decomposition. *J. Am. Chem. Soc.* **2014**, *136*, 12241−12244.
(26) Suarez, B.; Gonzalez-Pedro, V.; Ripolles, T. S.; Sanchez, R. S.; Otero, L.; Mora-Sero, I. Recombination Study of Combined Halides (Cl, Br, I) Perovskite Solar Cells. *J. Phys. Chem. Lett.* **2014**, *5*, 1628−1635.
(27) Aharon, S.; Cohen, B. E.; Etgar, L. Hybrid Lead Halide Iodide and Lead Halide Bromide in Efficient Hole Conductor Free Perovskite Solar Cell. *J. Phys. Chem. C* **2014**, *118*, 17160−17165.
(28) Nie, W.; Tsai, H.; Asadpour, R.; Blancon, J.-C.; Neukirch, A. J.; Gupta, G.; Crochet, J. J.; Chhowalla, M.; Tretiak, S.; Alam, M. A.; et al. High-Efficiency Solution-Processed Perovskite Solar Cells with Millimeter-Scale Grains. *Science* **2015**, *347*, 522−525.
(29) Moore, D. T.; Sai, H.; Tan, K. W.; Smilgies, D.-M.; Zhang, W.; Snaith, H. J.; Wiesner, U.; Estroff, L. A. Crystallization Kinetics of Organic−Inorganic Trihalide Perovskites and the Role of the Lead Anion in Crystal Growth. *J. Am. Chem. Soc.* **2015**, *137*, 2350−2358.
(30) Zhao, Y.; Zhu, K. Solution Chemistry Engineering toward High-Efficiency Perovskite Solar Cells. *J. Phys. Chem. Lett.* **2014**, *5*, 4175−4186.
(31) Burschka, J.; Pellet, N.; Moon, S.-J.; Humphry-Baker, R.; Gao, P.; Nazeeruddin, M. K.; Gratzel, M. Sequential Deposition as a Route to High-Performance Perovskite-Sensitized Solar Cells. *Nature* **2013**, *499*, 316−319.
(32) Liu, M.; Johnston, M. B.; Snaith, H. J. Efficient Planar Heterojunction Perovskite Solar Cells by Vapour Deposition. *Nature* **2013**, *501*, 395−398.
(33) Malinkiewicz, O.; Yella, A.; Lee, Y. H.; Espallargas, G. M.; Graetzel, M.; Nazeeruddin, M. K.; Bolink, H. J. Perovskite Solar Cells Employing Organic Charge-Transport Layers. *Nat. Photonics* **2013**, *8*, 128−132.
(34) Lin, Q.; Armin, A.; Nagiri, R. C. R.; Burn, P. L.; Meredith, P. Electro-Optics of Perovskite Solar Cells. *Nat. Photonics* **2014**, *9*, 106−112.
(35) Liu, D.; Gangishetty, M. K.; Kelly, T. L. Effect of $CH_3NH_3PbI_3$ thickness on device efficiency in planar heterojunction perovskite solar cells. *J. Mater. Chem. A* **2014**, *2*, 19873−19881.
(36) Chen, Y.; Chen, T.; Dai, L. Layer-by-Layer Growth of $CH_3NH_3PbI_{3-x}Cl_x$ for Highly Efficient Planar Heterojunction Perovskite Solar Cells. *Adv. Mater.* **2015**, *27*, 1053−1059.
(37) Jang, D. M.; Park, K.; Kim, D. H.; Park, J.; Shojaei, F.; Kang, H. S.; Ahn, J.-P.; Lee, J. W.; Song, J. K. Reversible Halide Exchange Reaction of Organometal Trihalide Perovskite Colloidal Nanocrystals for Full-Range Band Gap Tuning. *Nano Lett.* **2015**, *15*, 5191−5199.
(38) Pellet, N.; Teuscher, J.; Maier, J.; Grätzel, M. Transforming Hybrid Organic Inorganic Perovskites by Rapid Halide Exchange. *Chem. Mater.* **2015**, *27*, 2181−2188.
(39) Gil-Escrig, L.; Longo, G.; Pertegas, A.; Roldan-Carmona, C.; Soriano, A.; Sessolo, M.; Bolink, H. J. Efficient Photovoltaic and Electroluminescent Perovskite Devices. *Chem. Commun.* **2015**, *51*, 569−571.
(40) Chen, C.-W.; Kang, H.-W.; Hsiao, S.-Y.; Yang, P.-F.; Chiang, K.-M.; Lin, H.-W. Efficient and Uniform Planar-Type Perovskite Solar Cells by Simple Sequential Vacuum Deposition. *Adv. Mater.* **2014**, *26*, 6647−6652.
(41) Sadhanala, A.; Deschler, F.; Thomas, T. H.; Dutton, S. E.; Goedel, K. C.; Hanusch, F. C.; Lai, M. L.; Steiner, U.; Bein, T.; Docampo, P.; et al. Preparation of Single-Phase Films of $CH_3NH_3Pb(I_{1-x}Br_x)_3$ with Sharp Optical Band Edges. *J. Phys. Chem. Lett.* **2014**, *5*, 2501−2505.
(42) Wetzelaer, G.-J. A. H.; Scheepers, M.; Sempere, A. M.; Momblona, C.; Ávila, J.; Bolink, H. J. Trap-Assisted Non-Radiative Recombination in Organic-Inorganic Perovskite Solar Cells. *Adv. Mater.* **2015**, *27*, 1837−1841.
(43) Deschler, F.; Price, M.; Pathak, S.; Klintberg, L. E.; Jarausch, D.-D.; Higler, R.; Hüttner, S.; Leijtens, T.; Stranks, S. D.; Snaith, H. J.; et al. High Photoluminescence Efficiency and Optically Pumped Lasing in Solution-Processed Mixed Halide Perovskite Semiconductors. *J. Phys. Chem. Lett.* **2014**, *5*, 1421−1426.
(44) Wetzelaer, G. A. H.; Kuik, M.; Nicolai, H. T.; Blom, P. W. M.; Trap-Assisted. and Langevin-Type Recombination in Organic Light-Emitting Diodes. *Phys. Rev. B: Condens. Matter Mater. Phys.* **2011**, *83*, 165204.
(45) Schulz, P.; Edri, E.; Kirmayer, S.; Hodes, G.; Cahen, D.; Kahn, A. Interface Energetics in Organo-Metal Halide Perovskite-Based Photovoltaic Cells. *Energy Environ. Sci.* **2014**, *7*, 1377−1381.
(46) Momblona, C.; Malinkiewicz, O.; Roldán-Carmona, C.; Soriano, A.; Gil-Escrig, L.; Bandiello, E.; Scheepers, M.; Edri, E.; Bolink, H. J. Efficient Methylammonium Lead Iodide Perovskite Solar Cells with Active Layers from 300 to 900 nm. *APL Mater.* **2014**, *2*, 081504.

DOI: 10.1021/acs.jpclett.5b01716
J. Phys. Chem. Lett. 2015, 6, 3743−3748

Chapter 4.

Fullerene imposed high open-circuit voltage in efficient perovskite based solar cells.

4.1. Introduction

The material used as the electron transport layer (ETL) plays a key role in the overall solar cell functioning, as it controls the extraction and transport of the electrons from the absorber layer to the electrode. At the same time, it serves as a hole blocking layer and to suppress charge recombination at the interface. Some characteristics of the ETL leading to high photovoltaic performances are the high charge mobility, advantageous energy level alignment, low trap density, and good (homogeneous) morphology. As discussed in the introductory chapter, two main perovskite solar cell architectures have been developed so far, the mesoscopic and the planar PSCs, which can be further classified in n-i-p and p-i-n configurations. Until now, TiO_2 has been the most widely used ETL in n-i-p perovskite solar cells.[39, 88] The advantages presented by this material are: very fast electron injection rates from the perovskite to the TiO_2, simple fabrication, favorable energy level alignment and long electron lifetimes of TiO_2.[89] On the other hand, TiO_2 has a relatively low electron mobility (μ_e < 1 $cm^2\ V^{-1}\ s^{-1}$),[90] it requires high temperature for sintering and typically has a large density of trap states. Moreover, its photocatalytic activity under UV illumination could undermine the stability of the perovskite solar cells. For these reasons, alternative materials such as ZnO or SnO_2 have been investigated as ETLs in the n-i-p configuration, in view of their higher electron mobility compared to TiO_2 (the mobility for ZnO is 1 - 5 $cm^2\ V^{-1}\ s^{-1}$ and for SnO_2 can be as high as 250 $cm^2\ V^{-1}\ s^{-1}$) and their low-temperature synthesis.[89, 91-93] High performance perovskite solar cells have been obtained, indicating the potential of these materials. On the other hand, planar n-i-p solar cells based on metal oxides usually suffer from a large degree of hysteresis in the *J-V* characteristics. In orders to circumvent these issues, other device configurations have been studied, such us the p-i-n or “inverted” structure. Most of the p-i-n configuration uses PEDOT:PSS as the hole injection/extraction layer. Being a doped conducting polymer, PEDOT:PSS is not selective for holes and recombination can occur at the interface with the perovskite. For this reason we have adopted the use a thin electron blocking layer such as polyPTD in between the PEDOT:PSS and the perovskite absorber.[40] On the other hand, the choice for the electron

transport material (ETM) is rather limited. PCBM is the most widely used n-type organic semiconductor, due to its adequate electron mobility ($6 \cdot 10^{-2}$ cm^2 V^{-1} s^{-1}),[94] suitable energy level alignment, and the possibility to be processed at room temperature by simple solution processing. Moreover, it has been demonstrated that fullerenes can effectively passivate the perovskite surface states and alleviate photocurrent hysteresis.[9, 95, 96] Recently, *Shao et al* have demonstrated one of the best solar cell efficiencies (19.4%) using PCBM as the ETL. They highlighted the importance of the structural order in the electron transport layers as a means to improve the V_{oc}.[97] Apart from PCBM, other C_{60} derivatives and non-PCBM organic materials have been used in p-i-n perovskite solar cells. *Jeng et al.* were the first in adopting different fullerene derivatives in a p-i-n configuration. They tested PCBM, C_{60} and indene-C_{60} (ICBA) and they showed the formation of a donor-acceptor interface at the $CH_3NH_3PbI_3/C_{60}$ interface. Importantly, the application of ICBA significantly increased the V_{oc} as a consequence of the reduced energy losses at the perovskite interface.[98] Wang *et al.* reported a high fill factor using a double layer structure consisting of PCBM/C_{60} or ICBA/C_{60}, which they ascribed to passivation of traps states. Liang *et al*. showed a correlation between the electron mobility of the fullerene and the performance of the perovskite solar cell. They reported efficiencies of 8.06%, 13.37% and 15.44% for ICBA, PCBM and C_{60}, respectively, consequence of the fact that the electron mobility in C_{60} is higher compared to PCBM, and even higher than in ICBA.[94] Recently, the importance of the molecular design of the fullerene derivative when employed in perovskite devices has been underlined. ETMs which contain lone electron pairs can bind under-coordinated Pb atoms on the perovskite surface, efficiently passivating the material.[99-101] Moreover, some ETMs can effectively modify the work function (WF) of the cathode, improving the electron extraction. High PCEs of 17.6% have been reported using C5-NCMA, as this fullerene derivative presents a higher-lying LUMO compared to PCBM resulting in higher $V_{oc.}$[96] PCE up to 16.6% was obtained with C_{60}-N derivative, due to its superior electron-donating properties.[102] Finally, other alternative organic semiconductors are being investigated as ETMs in

perovskite solar cells, although their performances have not yet surpassed those obtained with fullerene derivatives.[103, 104]

4.2. Evaluation of five fullerene derivatives as electron transport materials in efficient perovskite solar cells.

In this chapter, five different commercially available fullerenes are evaluated as the hole blocking/electron transport materials in p-i-n perovskite solar cells. These derivatives contain longer alkyl esters (compared to the methyl ester in PCBM) which would favor the solubility in aromatic solvents at room temperature. In fact, at room temperature the solubility of PCBM in solvents such as toluene is approximately 20 mg mL^{-1}, limiting the achievable layer thickness. In addition, two different fullerene derivatives employing a different linker between the fullerene cage and the alkyl ester were investigated. *Sieval et al* showed that these two new fullerenes derivatives combine the advantages of PCBM, i.e., good solubility and simple processing, with higher V_{oc} due to the slightly lower reduction potentials.[105] The fullerenes employed are members of two families; [6,6]-phenyl-C_{61}-butyric acid with methyl (PCBM), butyl (PCBH), hexyl ester (PCBB), and indene-C_{60}-propionic acid butyl ester and hexyl ester (IPB and IPH, respectively), as depicted in Fig 4.1.b.

4.3. Experimental methods

Devices (Fig 4.1a) were prepared on cleaned ITO substrates by spin coating a thin layer (70nm) of PEDOT:PSS. On top of this a thin film of polyTPD was deposited from a chlorobenzene solution (7 mg mL^{-1}). The substrates were then transferred to a vacuum chamber integrated in a nitrogen-filled glovebox (O_2 and H_2O < 0.1 ppm). The deposition of the perovskite was performed by dual source thermal evaporation using the protocol described in chapter 2. The thickness of the perovskite film was about 320 nm in these experiments. The fullerene layers were deposited using a chlorobenzene solution of 20 mg mL^{-1} under ambient conditions using spin coating. The devices were completed by the thermal evaporation of the metal electrode under a base pressure of $2 \cdot 10^{-6}$ mbar, to a thickness of 10 nm of Ba and

100 nm of Ag. The device characterization was performed as described in chapter 2.3.

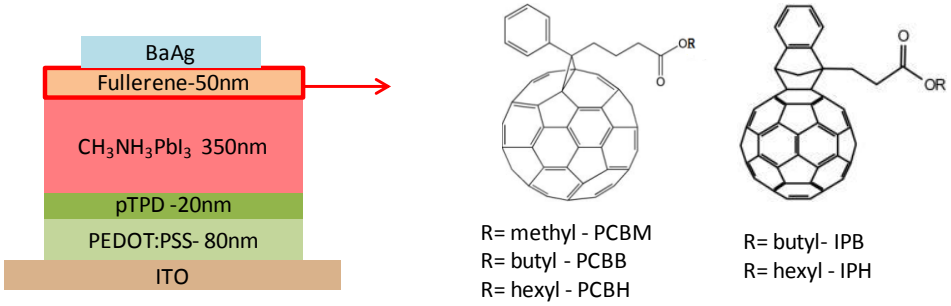

Fig 4.1 (a) Device layout (b) Chemical structures of the fullerene derivatives, PCBM, PCBB, PCBH, IPB, IPH.

4.4. Results and Discussion

The crystallinity and the absorption spectrum (Fig 4.2) of the $MAPbI_3$ films deposited by dual source thermal evaporation were initially analyzed. The crystallinity was investigated by GIXRD, and revealed the expected diffraction pattern of the tetragonal $MAPbI_3$ perovskite. The absorption spectra also confirmed the formation of the perovskite, showing the characteristic band-to-band absorption at about 760 nm.

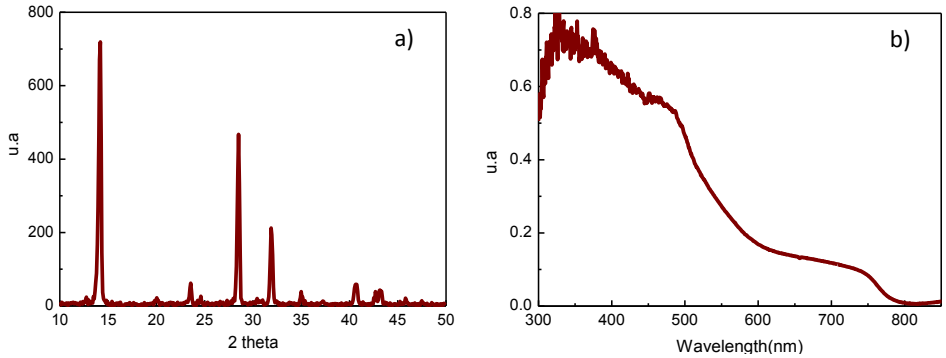

Fig 4.2 (a) XRD pattern and (b) optical absorption spectrum for the vacuum deposited perovskite film (thickness 320 nm).

The main difference between the fullerene derivatives (PCB-R and IP-R) is the increased length of the alkyl chains (Cn) used in the ester group,

increasing their solubility. In Fig 4.3 one can easily differentiate the two families of fullerenes, as the PCB-R show a higher absorption in the 350 - 450 nm range. Films of C_{60} are also known to show similar absorption tails at lower energies.[106] Furthermore, the IP-R films have only one absorption peak with a maximum around 325 nm whereas the PCB-R films present two peaks with maxima at 300 and 350 nm, due to the differences in the chemical structure among the two classes of compounds.

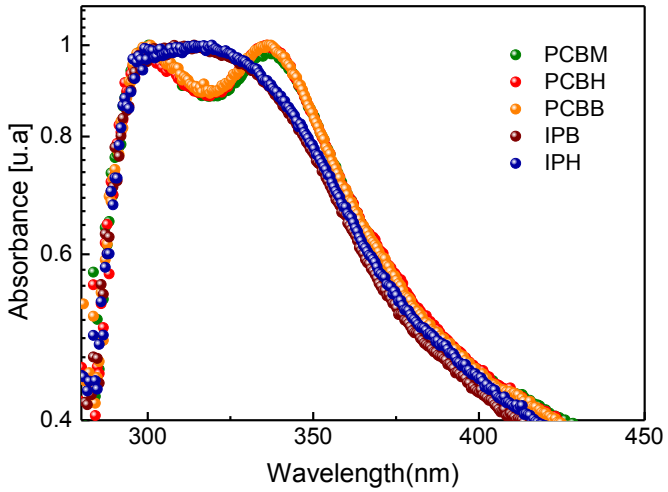

Fig 4.3 Optical absorption spectra for thin films of the five different fullerenes deposited on quartz.

AFM was employed to study the surface morphology of the different ETMs deposited on the perovskite films, as shown in Fig 4.4. It was observed for all fullerene derivatives that the calculated RMS roughness values were rather low. Although there were not large differences, the surface topography appeared more homogeneous and flat for PCBB and the IP-R compounds. This was corroborated at a larger scale by optical microscopy, as reported in Fig 4.5. Interestingly, when PCBM was processed on top of the perovskite films, large defects appeared on the surface, which are likely leading to charge recombination when the material is used in a diode.

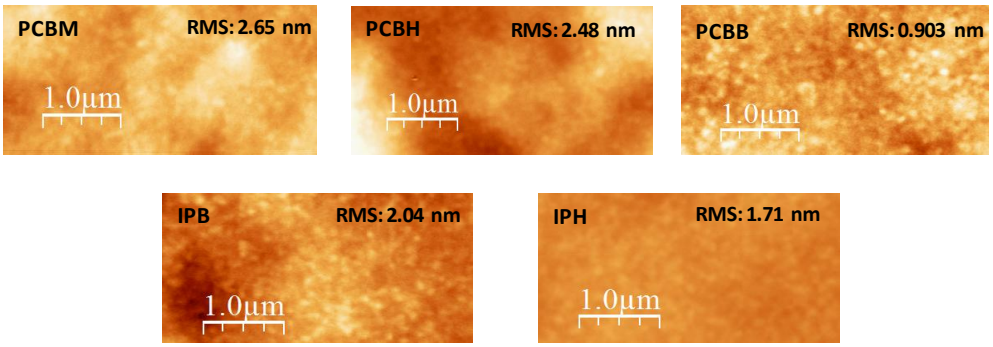

Fig 4.4 AFM topographies of a) PCBM, b) PCBH, c) PCBB, d) IPB and e) IPH thin films.

A better solubility of the alternative fullerene derivatives led to films with fewer defects, and more homogeneous films were obtained for the IP-R derivatives.

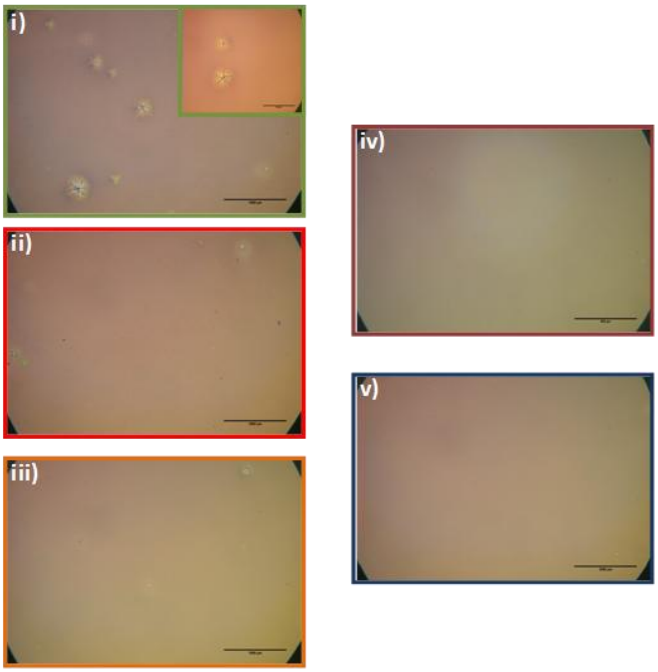

Fig 4.5 Optical microscopy images of the fullerene layers deposited on top of the perovskite: i) PCBM, ii) PCBH, iii) PCBB, iv) IPB and v) IPH.

The ETL series was hence incorporated in perovskite diodes and characterized under illumination and in forward bias to test their electroluminescence. The external quantum efficiency (EQE_{pv}, Fig 4.6) of the diodes was found to be rather independent on the ETL used, with a sharp increase at 770 nm in agreement with the perovskite absorption spectrum. As the $MAPbI_3$ strongly absorbs in the visible spectrum, the EQE_{pv} was as high as 0.7 in this range, while it diminished at wavelengths > 600 nm, where the perovskite is weekly absorbing (EQE_{pv} ~ 0.6). Slightly higher EQE_{pv} values were obtained when using the IPH as the ETL.

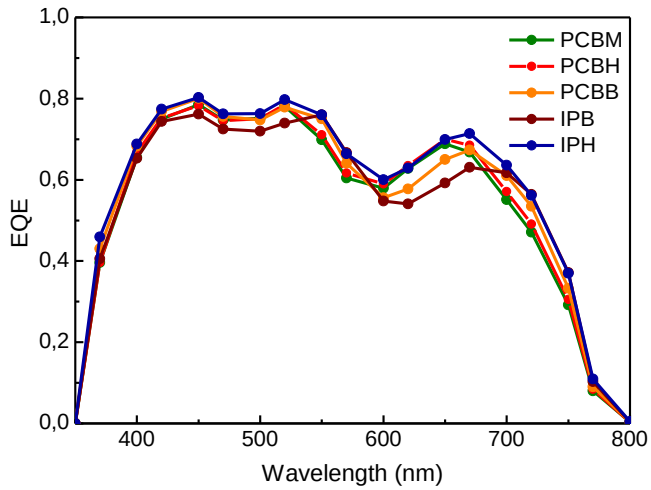

Fig 4.6 External quantum efficiency (EQE_{pv}) of the different diodes.

The *J-V* curves in the dark and under 1 sun illumination were collected. In the inset of Fig 4.7a, the dark current density versus voltage curves are shown for the whole device series. All *J-V* curves were similar independently of the fullerene employed, with a low parasitic leakage current indicating a high diode quality. The very similar behavior among the devices is interesting, as it implied that the large defect observed in Fig 4.5 after the deposition of the PCBM on top of the perovskite did not lead to direct ohmic contact between the Ba/Ag electrode and the perovskite.

The solar cell characteristics under approximately 1 sun illumination for the series of devices are shown in Fig 4.7a. No hysteresis was detected for any of the devices prepared when a scan speed of 0.01 V s^{-1} was used.

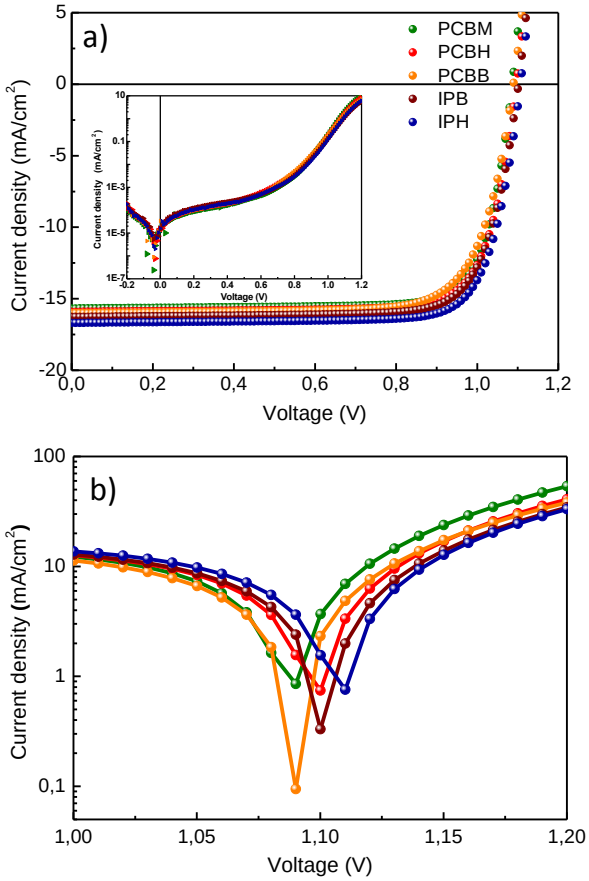

Fig 4.7 Electrical characterization of the solar cells employing different fullerenes: (a) current density versus voltage under 1 sun illumination and in the dark (inset); (b) zoom around the V_{oc} of the J-V curves on a log scale plot for the solar cell series.

No clear trend in the fill factors (FF) was observed with the different fullerenes employed, all of them lying between 75 and 80% (Fig 4.8). The high FF implies a good charge extraction up to voltages close to the V_{oc}. The short-circuit current of the solar cells was found to be higher in devices employing IPH as a ETL, in agreement with the trend observed previously with the EQE_{pv} (Fig 4.6). It is interesting to note that lower values were obtained for the devices with PCBM, likely due to the defects observed on the device surface, which might lead to charge recombination.

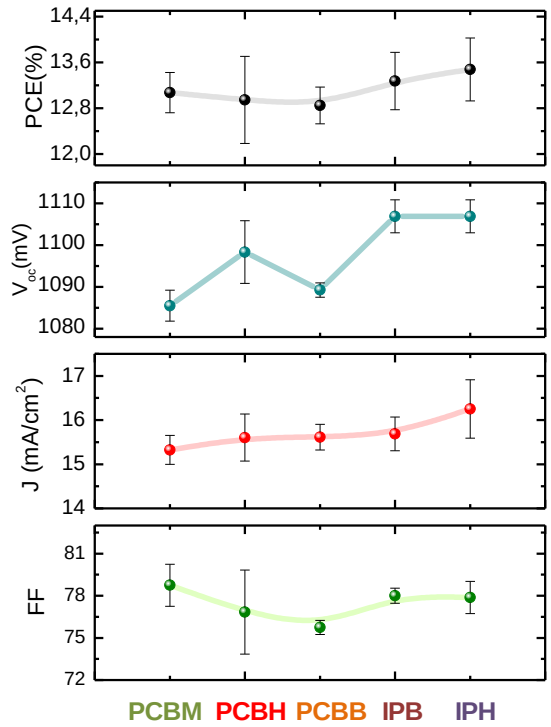

Fig 4.8 Photovoltaic parameters (J_{sc}, V_{oc}, FF, PCE) of the different fullerenes for > 8 devices per each configuration.

The V_{oc} values obtained were higher (10 - 20 mV) for the devices employing the IP-R derivatives. This in line with their lower reduction potential when compared to the PCBM, as reported by *Sieval et al.*[105] Due to the higher current density and open circuit voltage, the devices using IPH as the ETL exhibited the highest power conversion efficiencies, up to 14.6% for the record cell.

The increase of the V_{oc} might also be related to a decrease of the non-radiative recombination of the charge carriers in favor of radiative recombination. As highlighted previously, the radiative recombination should be the only recombination process occurring in a solar cell.[65] By measuring the EQE_{EL}, it is possible to estimate the recombination losses in the devices. Hence, the perovskite diode series with the different fullerene derivatives were also characterized under forward bias at moderate

voltages (above V_{oc}), and the electroluminescence was monitored using a sensitive Si-photodiode coupled to an integrating sphere.

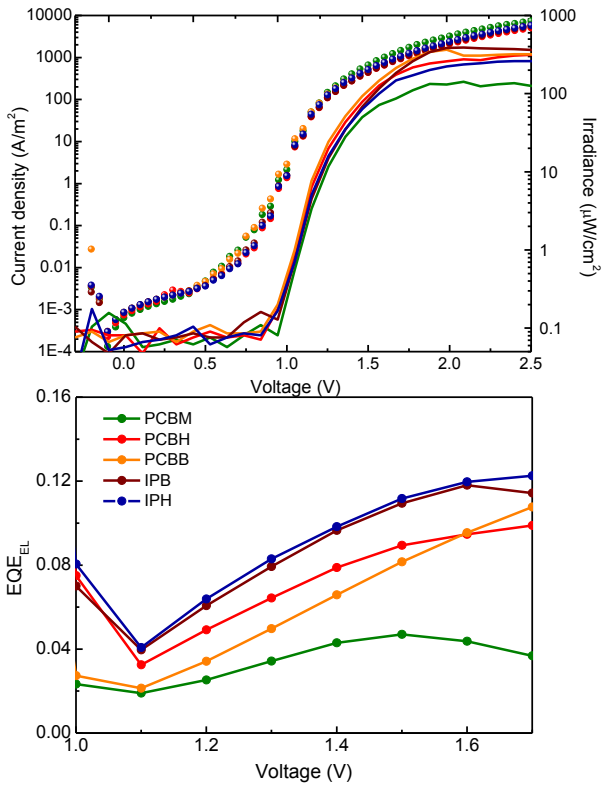

Fig 4.9 (a) Current density and irradiance versus the applied voltage and (b) corresponding external quantum efficiency (EQE_{EL}) for diodes employing different fullerene derivatives.

The current density and electroluminescence characteristics as a function of the applied bias for all devices are presented in Fig 4.9a. Intense electroluminescence was observed in all the devices prepared, with slightly differences depending on the fullerene used, and the turn-on voltage for the electroluminescence was found to be as low as 1 V, similar to literature reports.[74, 77, 86] The EQE_{EL} of the diodes did change depending of the fullerene derivative employed. For the PCBM-based cells, the value obtained was similar to previous reports.[74, 77, 86] The EQE_{EL} for the diodes

employing the other fullerenes was found to be higher compared to PCBM, with the highest value (about 0.12%) measured for the devices using the IP-R fullerenes. Interestingly, these two fullerenes were the ones leading to the larger V_{oc}, suggesting that the enhanced performance can at least partially be attributed to a reduction of non-radiative recombination.

4.5. Conclusion

In this chapter, five different fullerenes derivatives (PCBM, PCBH, PCBB, IPB, and IPH) were evaluated as the electron transport and hole blocking layer in p-i-n perovskite diodes. The layers prepared with fullerenes with longer alkyl chains presented fewer defects as compared to PCBM. Among these, the devices employing the IP-R derivatives resulted in larger current density and open circuit voltage, leading to higher efficiencies. The increase of the V_{oc} was accompanied by an improvement of the external quantum efficiency of the electroluminescence, suggesting a reduction of the non-radiative recombination in solar cells using IP-R derivatives as electron transport materials.

4.6. Contribution of the author

L. Gil-Escrig; C. Momblona; M. Sessolo; H. J. Bolink. “Fullerene imposed high open-circuit voltage in efficient perovskite based solar cells” J. Mater. Chem. A. 4, 3667-3672 (2016)

Journal of Materials Chemistry A

COMMUNICATION

View Article Online
View Journal | View Issue

Fullerene imposed high open-circuit voltage in efficient perovskite based solar cells†

Lidón Gil-Escrig, Cristina Momblona, Michele Sessolo and Henk J. Bolink*

Cite this: *J. Mater. Chem. A*, 2016, **4**, 3667

Received 23rd December 2015
Accepted 24th January 2016

DOI: 10.1039/c5ta10574a

www.rsc.org/MaterialsA

Five different commercially available fullerenes are evaluated as hole blocking/electron transporting materials in p–i–n methylammonium lead iodide perovskite solar cells using a vacuum deposited perovskite absorber layer. A significant enhancement of the solar cell performance can be obtained by selecting a suitable fullerene derivative. Open-circuit voltages as high as 1.11 volts are obtained leading to a power conversion efficiency of 14.6%.

Organometal halide perovskites have recently attracted much interest in photovoltaic applications because of their impressive performance, now exceeding 21%.[1–3] Several methods have been reported in order to deposit the perovskite layer; one of them is the physical vapour deposition technique. This presents some advantages over solution-based methods, such as high purity, compatibility with large area, and fine control over the film thickness and morphology, leading to high-efficiency photovoltaic devices.[4–9] In general, two main device architectures have been used to fabricate perovskite solar cells. One of them (n–i–p) is derived from cells built on a mesoporous TiO_2 scaffold with a typical configuration of a substrate/TiO_2 (n)/perovskite (i)/organic semiconductor (p).[10–13] The other configuration is the p–i–n structure, substrate/hole transporting layer (HTL) (p)/perovskite (i)/electron transporting layer (ETL) (n), in which the perovskite crystals are created on top of transparent substrates covered with a hole transport layer, mostly poly(3,4-ethylenedioxythiophene) doped with poly(styrenesulfonate) (PEDOT:PSS). The ETL materials used in this configuration are mostly fullerene derivatives.[5,14–16] Jeng *et al.* were the first in using three fullerene derivatives (C_{60}, phenyl-C_{61}-butyric acid methyl ester ($PC_{61}BM$)), and indene-C_{60} bisadduct ($IC_{60}BA$) in a p–i–n configuration such as ETLs.[14] They reported a PCE of 3.9% by employing PCBM and they verified the formation of a donor–acceptor interface at the $CH_3NH_3PBI_3/C_{60}$ interface. Soon after, Sun *et al.* demonstrated a pure bilayer $CH_3NH_3PBI_3/PC_{60}BM$ solar cell with a PCE of 7.4%, the best reported until then for an all-solution-processable planar heterojunction device.[17] More recently, Seo *et al.* reported the fabrication of a highly improved $MAPbI_3$ perovskite solar cell using a solvent engineering approach and varying PCBM layer thicknesses, leading to 14% in the optimum device.[18] Apart from PCBM, other fullerene derivatives have been used in perovskite solar cells. For example Wang *et al.* reported a high fill factor (FF) using a double layer structure to passivate trap states consisting of $PC_{61}BM/C_{60}$ or $IC_{60}BA/C_{60}$.[19] Also Chiang *et al.* reported an efficiency of 16.3% using $PC_{71}BM$ as an electron transport material, in which solvent annealing of this layer was carefully conducted.[20] Recently, Liang *et al.* demonstrated that the performance of a device follows the trend of increased electron mobility in the fullerene layer. They claimed that a higher electron mobility of the fullerene film promotes charge dissociation/transport in the device. They reported efficiencies of 8.06%, 13.37% and 15.44% for $IC_{60}BA$, $PC_{60}BM$, C_{60}, respectively, as the mobility in C_{60} is higher than that in the $PC_{60}BM$ and in the $IC_{60}BA$ films, respectively.[21] A lot of work on interface engineering between the PCBM layer and the metal contact has been carried out to overcome the mismatch in the energy levels of the metal contact (Al, Ag or Au) and the PCBM layer. In order to improve this, additional layers have been inserted between them, such as thermally evaporated LiF,[18] Ba[22] and C_{60}/bathocuproine (BCP),[23] or solution processed poly[(9,9-bis(30-(*N*,*N*-dimethylamino)propyl)-2,7-fluorene)-*alt*-2,7-(9,9-dioctylfluorene)]-(PFN),[24] bis-C_{60}-surfactant,[25] TiO_x,[15] ZnO,[26] *etc.*

PCBM is the most used fullerene derivative in the p–i–n architecture, yet its room temperature solubility in aromatic solvents is limited to approximately 20 mg ml^{-1} limiting the achievable layer thickness. Recently, different alkyl esters, instead of the methyl ester were offered commercially by Solenne BV. Additionally, two different alkyl esters of a slightly different fullerene employing a different linker were reported to have improved solubility and when used in an organic solar cell

Instituto de Ciencia Molecular, Universidad de Valencia, c/Catedrático J. Beltrán, 2, 46980 Paterna, Spain. E-mail: henk.bolink@uv.es; Fax: +34-963543273; Tel: +34-963544416

† Electronic supplementary information (ESI) available. See DOI: 10.1039/c5ta10574a

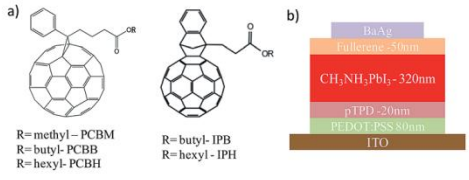

Fig. 1 (a) Chemical structures of the n-type fullerene derivatives, PCBM, PCBB, PCBH, IPB, and IPH. (b) Device layout.

to cause higher open-circuit voltages (V_{oc}'s). Sieval *et al.* claimed that these two new fullerene derivatives combine the advantages of [60]PCBM, *i.e.*, good solubility and easy separation, with higher V_{oc} values due to slightly lower reduction potentials.[27]

Most p–i–n type perovskite solar cells use PEDOT:PSS as the hole transporting layer yet as it is oxidized it does not block electrons. We have extensively studied the use of a thin electron blocking layer polyTPD (poly(*N*,*N*′-bis(4-butylphenyl)-*N*,*N*′-bis(phenyl)benzidine)) (a hole transporting arylamine based polymer) in between the PEDOT:PSS and the perovskite absorber.[5,28–32] As the polyarylamine layer is apolar, wetting from perovskite precursor solvents such as dimethylformamide is not good complicating the processing from the perovskite layer using precursor solutions. However, when the perovskite layer is deposited using a vacuum based process, which is rather insensitive to the substrate layer, a homogeneous perovskite layer is formed on the electron blocking layer. Using this architecture Lin *et al.*, achieved efficiencies of 16.5% in optimized cells using PCBM and a p-type polymeric semiconductor as the electron blocking layer.[6]

In this communication, five different commercially available fullerenes are evaluated as the hole blocking/electron transporting materials in p–i–n perovskite solar cells employing polyTPD as the electron blocking layer with a vacuum deposited perovskite absorber layer. The fullerenes are members of two distinct families; [6,6]-phenyl-C_{61}-butyric acid with methyl (PCBM), butyl (PCBH), hexyl ester (PCBB) and indene-C_{60}-propionic acid butyl ester and hexyl ester (IPB and IPH, respectively) (Fig. 1a). Improved processing and high power conversion efficiencies were obtained ranging from 13% to 14.6% depending on the particular fullerene employed. Hence, a significant enhancement of the solar cell performance can be obtained by selecting the suitable fullerene derivative.

Device preparation

Materials

Photolithographically patterned ITO covered glass substrates were purchased from Naranjo-Substrates (http://www.naranjosubstrates.com). PEDOT:PSS (Clevious PVP Al 4083) was obtained from Heraeus Holding and used as received. Poly-TPD was purchased from ADS Dye Source. PbI_2 was purchased from Aldrich and CH_3NH_3I from Lumtec, both were used as received. All the fullerenes (PCBM, PCBB, PCBH, IPB, IPH) were purchased from Solenne BV. Devices (Fig. 1b) were prepared on cleaned ITO substrates, by spin coating a thin layer (70 nm) of PEDOT:PSS. On top of this a thin film of polyTPD was deposited from a chlorobenzene solution (7 mg ml^{-1}). The substrates were transferred to a vacuum chamber into a nitrogen-filled glovebox (MBraun, <0.1 ppm O_2 and <0.1 ppm H_2O) and evacuated to a pressure of 1×10^{-6} mbar. Two ceramic crucibles were filled with CH_3NH_3I and PbI_2 each of which were heated to 70 °C and 250 °C, respectively, the $CH_3NH_3PbI_3$ was then thermally evaporated to a thickness of 320 nm, using a protocol described previously.[5] The film thickness was controlled by the PbI_2 evaporation rate maintained around 0.5 Å s^{-1}. The fullerene layer was deposited using a chlorobenzene solution of 20 mg ml^{-1} under ambient conditions using spin coating. The devices were completed by the thermal evaporation of the metal electrode under a base pressure of 2×10^{-6} mbar to a thickness of 10 nm of Ba and 100 nm of Ag. Device characterization was performed using a mini-sun simulator with a halogen lamp designed by ECN and calibrated with a Si reference cell. The unencapsulated solar cells were measured in a N_2-filled glovebox. The current density (*J*) *versus* voltage (*V*) characteristics were obtained in the dark and under illumination using a shadow mask to prohibit lateral current collection from outside the active area. The current-density-*versus*-voltage (*J*–*V*) and irradiance-*versus*-voltage (*L*–*V*) characteristics were obtained using a Keithley Model 2400 source measurement unit and a Si-photodiode coupled to an integrated sphere, respectively.

Results and discussion

The crystallinity of the vacuum deposited perovskite was investigated by grazing incidence X-ray diffraction (GIXRD) measurements, revealing the typical $CH_3NH_3PbI_3$ diffraction pattern (in terms of both peak position and relative intensity, see Fig. S1†). The absorption spectrum (Fig. S2†) also confirms the formation of the perovskite. The main difference between PCBM and PCB-Cn (PCBH and PCBB) is the increased length of the alkyl chains (Cn) used in the ester group that makes them more soluble. This leads to improved processing and to more homogeneous layers on top of the perovskite layer with fewer defects as evidenced by optical microscope images (Fig. S3 in the ESI†). The film morphology on a micrometer scale as observed from atomic force microscope characterization does not show significant differences between the different fullerene derivatives (Fig. S4†). In all cases the fullerene films on top of the perovskite absorbers are rather smooth with a root-mean-square roughness of around 10 nm. The absorption spectra of the PCB-R films are similar, yet differ from those of the films of the IP-R derivatives (Fig. 2).

The PCB-R show a higher absorption (350–450 nm), with weak tails extending as far as 600 nm (Fig. S5†). The origin of this absorption tail is the result of light scattering or other experimental artefacts. We note that films of C_{60} are reported to have similar absorption tails at low energies.[33] The IP-R films have only one absorption peak with a maximum around 325 nm whereas the PCB-R films present two peaks with maxima at 300

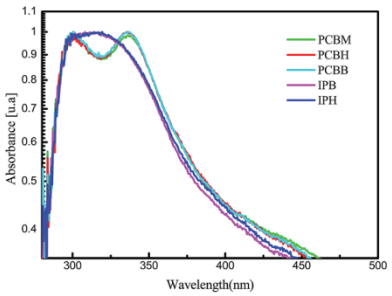

Fig. 2 Optical absorption spectra for thin films on quartz of the five different fullerene derivatives.

and 350 nm, due to the differences in the chemical structure as seen before for the fullerenes.

The devices employing the different fullerenes were characterized by determining the current density *versus* voltage both in the dark and under approximate 1 sun illumination. Fig. 3a shows the dark current density *versus* voltage curves. The leakage current is low, indicating the high quality of the diodes independent of the fullerene employed for the whole series of devices. This is remarkable in view of the craters observed in the PCBM films (Fig. S3†) when deposited on top of the perovskite layer. It implies that such craters do not lead to ohmic leakage currents due to charge injection from the Ba/Ag electrode to the perovskite layer. A low leakage current density is beneficial for maximum open circuit voltages as the recombination due to leakage is diminished. The typical diode performance under approximately 1 sun illumination for the series of devices is shown in Fig. 3b. In line with the good diode quality the *J–V* curves under illumination are also rather squared showing good charge extraction up to voltages close to V_{oc}. This is evidenced by the high fill factors obtained which are in between 75 and 80% (see Table 1). No clear trends in the FF with the different fullerenes employed were observed, although the devices with the PCBB fullerene showed consistently lower values than the others. The short-circuit current density (J_{sc}) of the solar cells was highest for the devices employing IPH as the n-type layer. There was not much difference in J_{sc} for the other devices employing the rest of the fullerenes, although the lowest J_{sc} values were obtained for devices employing PCBM. In the devices using PCBM the reduction in current density is most likely due to the defects (craters) in the PCBM layer (see Fig. S3†) as commented previously. These defects are positions in the device that lead to charge recombination.

The V_{oc} values obtained were higher (10–20 mV) for the devices employing the IP-R derivatives. This is in line with the lower reduction potential of the IP-R fullerenes compared to PCBM as reported by Sieval *et al.*[27] Hence, here a clear effect of the LUMO level of the fullerene on the obtainable V_{oc} is shown, implying that further optimizations are possible. Due to both the higher current density and open circuit voltage for the devices using IPH as the hole blocking material, these devices exhibit the best power conversion efficiencies reaching 14.6% for the record cell. Considering that the thickness of the perovskite layer used is 320 nm these efficiencies are among the

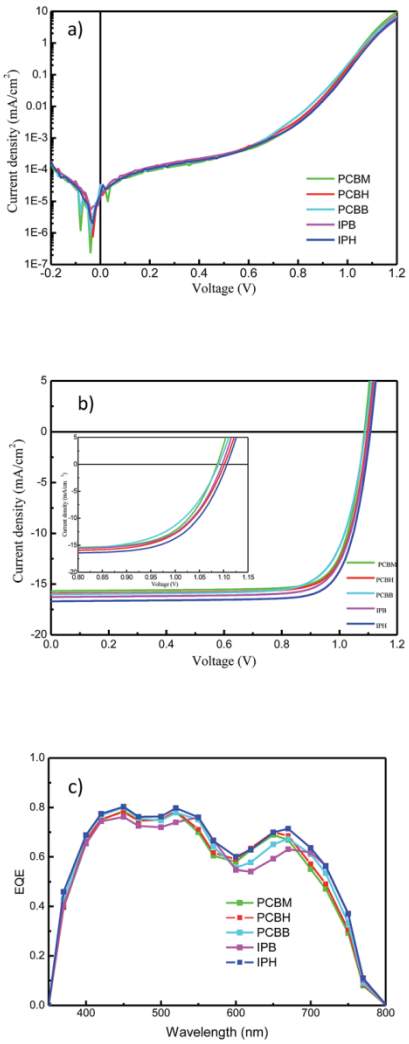

Fig. 3 Electrical characterization of the different diodes, (a) current density *versus* voltage plotted on a semilog scale (b) current density *versus* voltage curves under 1 sun illumination, inset shows amplification of the curves, and (c) external quantum efficiency (EQE_{PV}) of the different diodes.

Table 1 Photovoltaic parameters for the devices using the studied fullerenes

Fullerene	V_{oc} (mV)	J_{sc} (mA cm^{-2})	FF (%)	PCE (%)
PCBM	1087	15.68	80	13.58
PCBH	1097	15.92	79	13.75
PCBB	1090	16.02	76	13.27
IPB	1102	16.28	78	14.02
IPH	1107	16.70	79	14.64

best obtained for vacuum deposited p–i–n type solar cells. No hysteresis was detected when a scan speed of 0.01 V s^{-1} was used for any of the devices using the different fullerenes. The forward and reverse *J–V* scans are virtually identical (Fig. S6†). The key device parameters are summarized in Table 1 (best data, represented) whereas the spreading of the data is represented in Fig. S7 of the ESI.†

The external quantum efficiency (EQE_{PV}, Fig. 3c) of the diodes was determined by illuminating them with a white-light halogen lamp in combination with narrow bandpass filters. The EQE_{PV} values of the devices employing the different fullerenes were high (0.7 to 0.8) in the visible range, while they diminished at wavelengths > 600 nm, where the perovskite is weakly absorbing ($EQE_{PV} \sim 0.6$). The onset response lies in the near-infrared, 770 nm. The trend in EQE_{PV} is the same as previously observed for the J_{sc}, hence again the highest values are observed for the devices using IPH as the hole blocking material. The calculated current density is within 5% of the measured value under 1 sun illumination.

The increase in V_{oc} of the solar cells employing IPH, compared to those that use PCB-R varieties, may be due to the lower reduction potential of IPH. Yet this also implies that the quasi fermi level splitting in the perovskite layer must be sufficient to yield such a high V_{oc}. One of the major loss factors in the potential energy of the separated electron and holes is non-radiative decay.[34] Hence, if the V_{oc} is increased this may be related to a decrease in the non-radiative recombination of charge carriers in favour of radiative recombination. To test this, the diode series containing the different fullerene derivatives were also driven under forward bias at moderate voltages (above the V_{oc}). The electroluminescence was monitored using a sensitive Si-photodiode coupled to an integrating sphere.

In Fig. 4a, the current density and irradiance as a function of the applied bias for all devices using the different fullerene derivatives are presented. A deviation from the leakage current occurs around 0.5 V, after which two regimes can be identified. First, an almost linear increase (in the log scale plot) is present, followed by a slower increase at higher voltages. The first regime is due to a diffusion current, whereas the second regime is indicative of an injection or space-charge limited current. Eventually, the current density reaches values higher than 100 mA cm^{-2} at 2.5 V, indicative of low carrier injection barriers and good charge transport in the diodes. Intense electroluminescence was observed in all the devices prepared, with only slight differences as a function of the fullerene derivative used. The

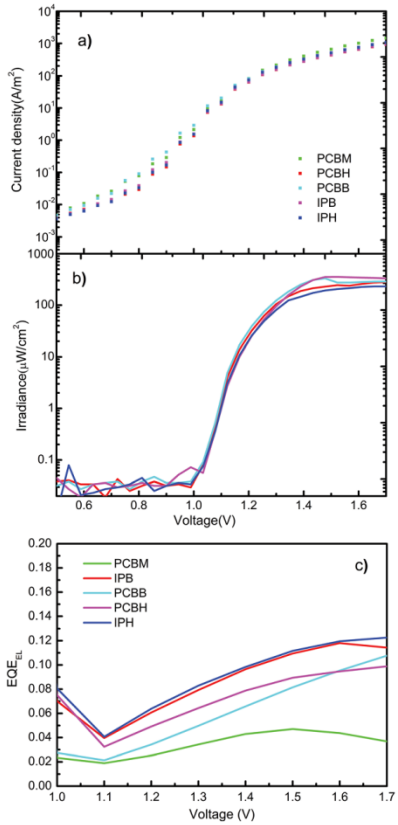

Fig. 4 (a) Current density and (b) radiance *versus* the voltage applied. (c) External quantum efficiency (EQE) *versus* the voltage applied for the different fullerene derivatives used.

turn-on voltage for the electroluminescence was found to be as low as 1 V for the complete series of devices, similar to that previously reported.[22,35,36]

The maximum external quantum efficiency of the electroluminescence (EQE_{EL}) of the diodes, however, did change depending on the fullerene derivative that was used. For the diode using PCBM an EQE_{EL} of ~0.04% (Fig. 4b) was obtained, very similar to that reported previously for similar diodes.[22,35,36] Yet the EQE_{EL} for the devices using fullerenes different from PCBM is increased, with the best values found for devices using the IP-R fullerenes reaching 0.12%. This is a 3 times increase compared to the EQE_{EL} of the diode employing PCBM. Hence, the increase in V_{oc} of the solar cells is accompanied by an increase in the radiative efficiency suggesting a reduction in non-radiative decay pathways.

Conclusions

In summary, five different fullerene derivatives (PCBM, PCBH, PCBB, IPB and IPH) were evaluated as the electron transporting/hole blocking layer in p–i–n solar cells. The fullerenes with alkyl esters longer than methyl lead to improved layers with fewer defects than the layers obtained with PCBM. In the devices employing the PCB-R fullerenes, the improved layer quality did not lead to a significant improvement in photovoltaic behaviour. For the devices that use the IP-R type fullerenes both the current density and open circuit voltage are improved, leading to improved photovoltaic performance of these devices. When operated as LEDs, it was shown that the external quantum efficiency of electroluminescence is improved for all devices with the longer alkyl ester fullerenes, which is indicative of a reduction in the non-radiative decay in these devices. Hence, the PCB-R and in particular IP-R are very promising fullerenes for perovskite solar cells and larger area processing where the layer formation is more critical than in the small area devices used here.

Acknowledgements

This work was supported by the European Union H2020 project INFORM (grant 675867), the Spanish Ministryof Economy and Competitiveness (MINECO) (MAT2014-55200)and the Generalitat Valenciana (Prometeo/2012/053). C. M. thanks the MINECO for a predoctoral contract (previously FPI).

References

1 A. Kojima, K. Teshima, Y. Shirai and T. Miyasaka, *J. Am. Chem. Soc.*, 2009, **131**, 6050–6051.
2 M. M. Lee, J. Teuscher, T. Miyasaka, T. N. Murakami and H. J. Snaith, *Science*, 2012, **338**, 643–647.
3 W. S. Yang, J. H. Noh, N. J. Jeon, Y. C. Kim, S. Ryu, J. Seo and S. I. Seok, *Science*, 2015, **348**, 1234–1237.
4 M. Liu, M. B. Johnston and H. J. Snaith, *Nature*, 2013, **501**, 395–398.
5 O. Malinkiewicz, A. Yella, Y. H. Lee, G. M. Espallargas, M. Graetzel, M. K. Nazeeruddin and H. J. Bolink, *Nat. Photonics*, 2014, **8**, 128–132.
6 Q. Lin, A. Armin, R. C. R. Nagiri, P. L. Burn and P. Meredith, *Nat. Photonics*, 2015, **9**, 106–112.
7 C.-W. Chen, H.-W. Kang, S.-Y. Hsiao, P.-F. Yang, K.-M. Chiang and H.-W. Lin, *Adv. Mater.*, 2014, **26**, 6647–6652.
8 L. E. Polander, P. Pahner, M. Schwarze, M. Saalfrank, C. Koerner and K. Leo, *APL Mater.*, 2014, **2**, 081503.
9 L. K. Ono, M. R. Leyden, S. Wang and Y. Qi, *J. Mater. Chem. A*, 2016, DOI: 10.1039/c5ta08963h.
10 S. D. Stranks, G. E. Eperon, G. Grancini, C. Menelaou, M. J. P. Alcocer, T. Leijtens, L. M. Herz, A. Petrozza and H. J. Snaith, *Science*, 2013, **342**, 341–344.
11 G. E. Eperon, V. M. Burlakov, P. Docampo, A. Goriely and H. J. Snaith, *Adv. Funct. Mater.*, 2014, **24**, 151–157.
12 B. Conings, L. Baeten, C. De Dobbelaere, J. D'Haen, J. Manca and H.-G. Boyen, *Adv. Mater.*, 2014, **26**, 2041–2046.
13 Q. Chen, H. Zhou, Z. Hong, S. Luo, H.-S. Duan, H.-H. Wang, Y. Liu, G. Li and Y. Yang, *J. Am. Chem. Soc.*, 2014, **136**, 622–625.
14 J.-Y. Jeng, Y.-F. Chiang, M.-H. Lee, S.-R. Peng, T.-F. Guo, P. Chen and T.-C. Wen, *Adv. Mater.*, 2013, **25**, 3727–3732.
15 P. Docampo, J. M. Ball, M. Darwich, G. E. Eperon and H. J. Snaith, *Nat. Commun.*, 2013, 4.
16 J.-Y. Jeng, K.-C. Chen, T.-Y. Chiang, P.-Y. Lin, T.-D. Tsai, Y.-C. Chang, T.-F. Guo, P. Chen, T.-C. Wen and Y.-J. Hsu, *Adv. Mater.*, 2014, **26**, 4107–4113.
17 S. Sun, T. Salim, N. Mathews, M. Duchamp, C. Boothroyd, G. Xing, T. C. Sum and Y. M. Lam, *Energy Environ. Sci.*, 2014, **7**, 399–407.
18 J. Seo, S. Park, Y. Chan Kim, N. J. Jeon, J. H. Noh, S. C. Yoon and S. I. Seok, *Energy Environ. Sci.*, 2014, **7**, 2642–2646.
19 Q. Wang, Y. Shao, Q. Dong, Z. Xiao, Y. Yuan and J. Huang, *Energy Environ. Sci.*, 2014, **7**, 2359–2365.
20 C.-H. Chiang, Z.-L. Tseng and C.-G. Wu, *J. Mater. Chem. A*, 2014, **2**, 15897–15903.
21 P.-W. Liang, C.-C. Chueh, S. T. Williams and A. K. Y. Jen, *Adv. Energy Mater.*, 2015, **5**, 1402321.
22 L. Gil-Escrig, G. Longo, A. Pertegas, C. Roldan-Carmona, A. Soriano, M. Sessolo and H. J. Bolink, *Chem. Commun.*, 2015, **51**, 569–571.
23 Z. Xiao, C. Bi, Y. Shao, Q. Dong, Q. Wang, Y. Yuan, C. Wang, Y. Gao and J. Huang, *Energy Environ. Sci.*, 2014, **7**, 2619–2623.
24 J. You, Y. Yang, Z. Hong, T.-B. Song, L. Meng, Y. Liu, C. Jiang, H. Zhou, W.-H. Chang, G. Li and Y. Yang, *Appl. Phys. Lett.*, 2014, **105**, 183902.
25 P.-W. Liang, C.-Y. Liao, C.-C. Chueh, F. Zuo, S. T. Williams, X.-K. Xin, J. Lin and A. K. Y. Jen, *Adv. Mater.*, 2014, **26**, 3748–3754.
26 W. Qiu, M. Buffière, G. Brammertz, U. W. Paetzold, L. Froyen, P. Heremans and D. Cheyns, *Org. Electron.*, 2015, **26**, 30–35.
27 A. B. Sieval, N. D. Treat, D. Rozema, J. C. Hummelen and N. Stingelin, *Chem. Commun.*, 2015, **51**, 8126–8129.
28 K. Tvingstedt, O. Malinkiewicz, A. Baumann, C. Deibel, H. J. Snaith, V. Dyakonov and H. J. Bolink, *Sci. Rep.*, 2014, **4**, 6071.
29 C. Roldan-Carmona, O. Malinkiewicz, A. Soriano, G. Minguez Espallargas, A. Garcia, P. Reinecke, T. Kroyer, M. I. Dar, M. K. Nazeeruddin and H. J. Bolink, *Energy Environ. Sci.*, 2014, **7**, 994–997.
30 C. Roldan-Carmona, O. Malinkiewicz, R. Betancur, G. Longo, C. Momblona, F. Jaramillo, L. Camacho and H. J. Bolink, *Energy Environ. Sci.*, 2014, **7**, 2968–2973.
31 C. Momblona, O. Malinkiewicz, C. Roldán-Carmona, A. Soriano, L. Gil-Escrig, E. Bandiello, M. Scheepers, E. Edri and H. J. Bolink, *APL Mater.*, 2014, **2**, 081504.
32 O. Malinkiewicz, C. Roldán-Carmona, A. Soriano, E. Bandiello, L. Camacho, M. K. Nazeeruddin and H. J. Bolink, *Adv. Energy Mater.*, 2014, 1400345, DOI: 10.1002/aenm.201400345.

33 S. Cook, H. Ohkita, Y. Kim, J. J. Benson-Smith, D. D. C. Bradley and J. R. Durrant, *Chem. Phys. Lett.*, 2007, **445**, 276–280.
34 O. D. Miller, E. Yablonovitch and S. R. Kurtz, *IEEE Journal of Photovoltaics*, 2012, **2**, 303–311.
35 Z.-K. Tan, R. S. Moghaddam, M. L. Lai, P. Docampo, R. Higler, F. Deschler, M. Price, A. Sadhanala, L. M. Pazos, D. Credgington, F. Hanusch, T. Bein, H. J. Snaith and R. H. Friend, *Nat. Nanotechnol.*, 2014, **9**, 687–692.
36 Y.-H. Kim, H. Cho, J. H. Heo, T.-S. Kim, N. Myoung, C.-L. Lee, S. H. Im and T.-W. Lee, *Adv. Mater.*, 2015, **27**, 1248–1254.

Chapter 5.

Interface engineering in efficient vacuum deposited perovskite solar cells.

5.1. Introduction.

The difference in energy between the work function of common electrode metals, such as Ag, Au or Al, and the lowest unoccupied molecular orbital (LUMO) of electron transport materials such as PCBM, can hinder efficient charge injection and extraction in organic optoelectronic devices.[107, 108] Ideally, an ohmic contact between the electrode and the electron transport material should be attained, by minimizing the energy barrier at the interface. In some cases, the deposition of metals such as Al onto fullerenes can lead to a chemical reaction at the interface and to the formation of an insulating layer between the cathode and the ETL, causing a rapid degradation of the device performance.[109] Extensive work has been carried out in order to find interlayers able to reduce the energy mismatch between the LUMO of fullerenes and the work function of the metal cathode, while also functioning as a protection to avoid diffusion of the thermally evaporated metal into the organic materials. In perovskite solar cells, metal oxides (TiO_2, ZnO) have been widely investigated as ETLs in n-i-p configurations.[55, 110] Moreover, they have also been studied as interlayers between the fullerene ETL and the cathode in p-i-n cells, with promising performance and stability. *Docampo et al.* showed the potential of using a compact film of TiO_2 deposited from solution in between PCBM and Al, obtaining efficiencies up to 9.8%.[110] In a similar manner, *Bai et al.* integrated ZnO nanocrystals at the cathode interface, which enhanced the electrical contact and the cell-to-cell reproducibility, as well as their environmental stability.[111] In general for perovskite solar cells there has been a large effort in identifying new interfacial materials, as perovskites are more prone to surface recombination.[95] In particular, efforts are directed towards the passivation of defects at the perovskite surface and especially at the grain boundaries. *Min et al*[112] first demonstrated the potential of a perylene-diimide derivative to modify the PCBM/Ag interface, showing a remarkable PCE of 14%. Other organic materials have been used to reduce the contact resistance and the interfacial charge recombination, improving in this way the charge extraction. Among these, bathocuproine (BCP) is commonly used in combination with fullerenes,[55] while bis-C60 surfactant,[113] amino-functionalized polymers (PN4N)[114] or titanium

(diisopropoxide) bis(2,4-pentanedionate) (TIPD) buffer layers[115] have also been used in perovskite cells. Some polyelectrolytes (e.g., PEIE, P3TMAHT) were introduced at the interface in order to create a quasi-ohmic contact, as a consequence of the formation of interface dipoles with a negative charge on Ag.[116] Finally, thin interlayers such as LiF or low work function metals such as Ba/Ca are also used in order to ensure an ohmic contact and efficient charge extraction.[117, 118] These materials are, however, very reactive towards air and oxygen, hence the devices must be rigorously encapsulated to avoid rapid degradation.

5.2. Interface engineering in efficient perovskite solar cells

In this chapter, the effect of combining a fullerene ETL with ionic electron extraction interlayers in p-i-n perovskite solar cells is discussed. The two ionic interlayers presented in this work are a perylene diimide with N-oxide as the terminal groups (PDINO)[66, 112] and a conjugate polyelectrolyte, PFNBr[119, 120], whose structures are reported in Fig 5.1. Both materials are soluble in polar solvents and can therefore be deposited onto the fullerene ELT by spin-coating, prior to the deposition of a metal cathode. The fullerene derivative employed in this work is IPH, which was selected following the study presented in the previous chapter.[121] In addition, in this chapter we show that an electron blocking layer in between the PEDOT:PSS and the perovskite is needed to guarantee high performing devices.

5.3 Experimental methods

PEDOT:PSS was spin-coated on top of clean ITO substrates and annealed at 150 ºC for 15 min. A thin film of polyTPD was subsequently deposited from a chlorobenzene solution (7 mg mL^{-1}). Hence the substrates were transferred to a vacuum chamber integrated in a nitrogen-filled glovebox. The deposition of the perovskite was carried out by dual source thermal evaporation using the protocol described in chapter 2.2. The IPH films were deposited by spin coating its chlorobenzene solution (20 mg mL^{-1}) in air. Hence, a thin layer of PDINO or PFNBr was spin coated from methanol (concentrations of 1 mg mL^{-1} or 2 mg mL^{-1}, respectively) on top of the fullerene layer. The devices were completed with the thermal evaporation

of the top electrode (either 100 nm Ag or 10 nm Ba capped with 100 nm Ag) under a base pressure of $2 \cdot 10^{-6}$ mbar. The device characterization was performed as described in chapter 2.2.

5.4. Results and Discussion

Fig 5.1a depicts the p-i-n device structure employed, with the molecular structures of the ionic interlayers, PDINO and PFNBr.

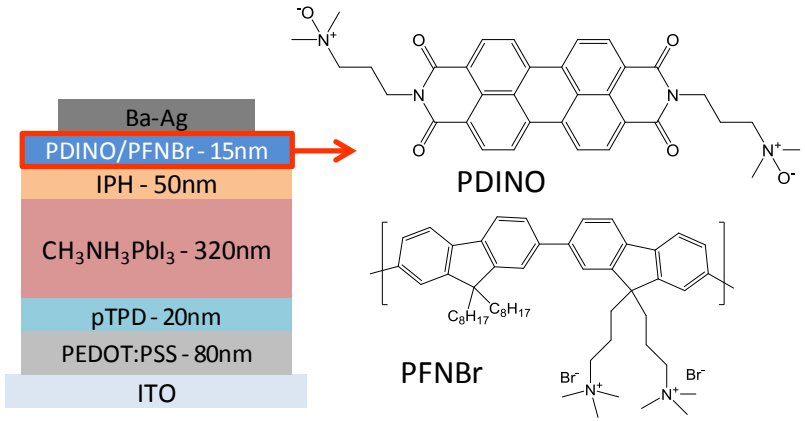

Fig 5.1 Schematics of the p-i-n perovskite solar cell with the molecular structures of PDINO and PFNBr.

The formation of the $MAPbI_3$ perovskite phase was confirmed by GIXRD measurements and optical absorption (Fig 5.2).

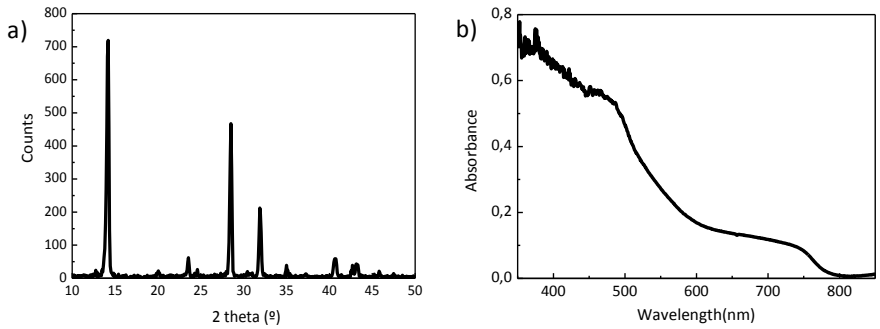

Fig 5.2 (a) GIXRD pattern and (b) optical absorption spectrum of the vacuum deposited perovskite film (320 nm), with preferred orientation along (100) and (001) directions.

First of all, the effect of the polyTPD electron blocking layer on the device performance was studied. Fig 5.3a shows the *J-V* curves in the dark. Both devices presented the typical behavior of a diode and similar leakage current, although the device without the electron blocking layer showed a lower built-in potential and a higher current density compared with the one with polyTPD.

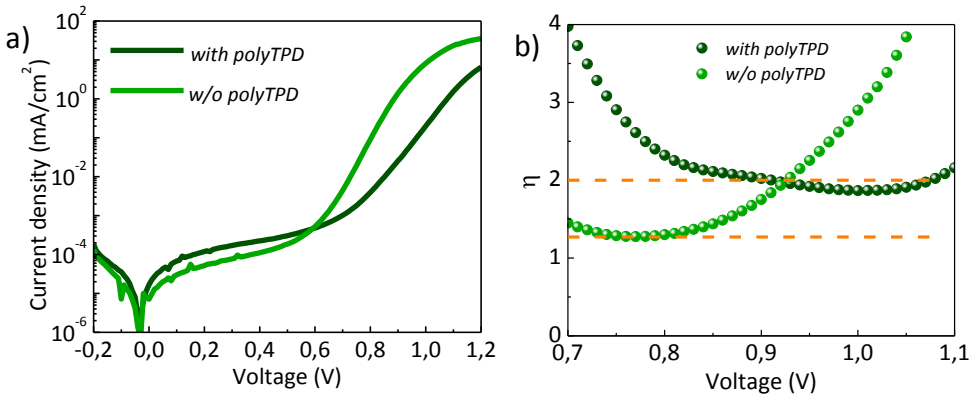

Fig 5.3 (a) J-V curves in the dark and (b) calculated ideality factor for devices with and without polyTPD. The electron extraction used for these cells is IPH/Ba-Ag.

The minimum of the current density was found not to be at V = 0 V, most likely due to partial charging of the cells during the voltage sweep, when some charges accumulate at one of the device interfaces. In order to study the differences among these diodes, we calculated the ideality factor (η, Fig 5.3b). As described chapter 4, in the absence of recombination, the ideal diode equation should apply, where η equals unity. This is also the case for direct recombination, whereas trap-assisted recombination can change the ideality factor up to a value of 2.[85] From Fig 5.3b, we could observe that the device without polyTPD presented a η value close to 1, suggesting direct recombination taking place at the PEDOT:PSS contact, whereas for the device with electron blocking layer, the recombination at the interface was mainly trap-assisted recombination (η~ 2), in agreement with previous reports on similar devices.[85] Fig 5.4 shows the current density vs voltage curves measured under illumination for the same device series and the corresponding EQE.

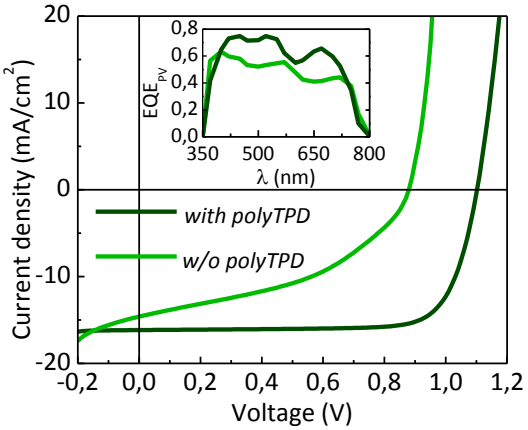

Fig 5.4 J-V curves under illumination for devices with and without polyTPD, using IPH/Ba-Ag as electron extraction layer. The inset shows the corresponding photovoltaic external quantum efficiency (EQE_{pv}).

Also the *J-V* curves under illumination suggest a significant recombination of the photogenerated charge carriers when no electron blocking layer is deposited below the perovskite. In fact, the device showed a lower V_{oc} (0.88 V) compared to the solar cells employing a polyTPD layer (1.1 V). In addition, polyTPD has a larger ionization potential compared to PEDOT:PSS, which helps maintaining the device photovoltage. The direct recombination and the lower built-in potential in the polyTPD-free device also affect the FF. Likewise, the photovoltaic external quantum efficiency (EQE_{PV}) was substantially reduced in the cells without polyTPD, resulting in lower current densities. Another possible explanation for the lower performance in the devices without polyTPD could be the chemical reduction of the PEDOT:PSS when the methylamine (MA) is present in the atmosphere. It has been reported that after the reduction, a strong absorbance band appears at 400-1100 nm and the conductivity and work function simultaneously decrease.[122] This PEDOT:PSS reduction leads to a poor hole collection, with low V_{oc} , J_{sc} and hence PCEs in the perovskite solar cells. These findings could be more critical in the dual-source vapour deposited perovskite based solar cells, as it is more likely that part of the MAI degrades to MA and hydroiodic acid (HI). Within this view, the additional

polyTPD layer would protect PEDOT:PSS from interacting with the perovskite precursors.

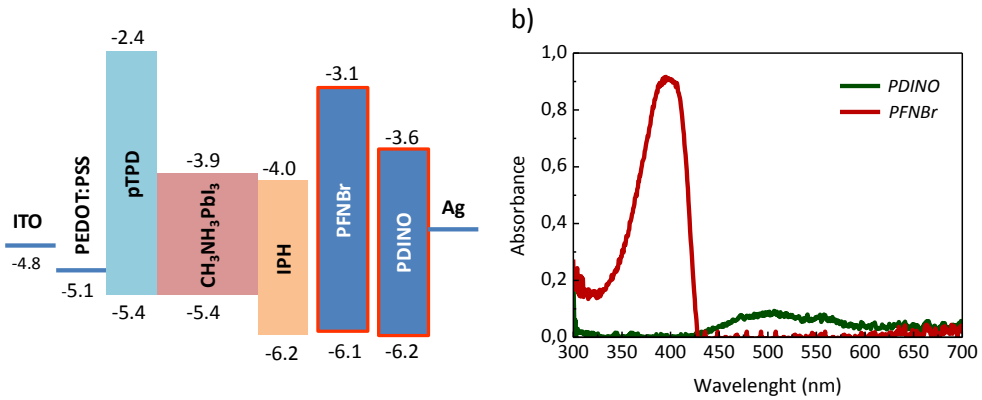

Fig 5.5 Flat energy band diagram for the materials used in the device preparation (b) Optical absorption spectra of both electron extraction layers on quartz substrates.

As mentioned before, Ba is a very reactive metal that will affect the long-term stability of the solar cells if not rigorously encapsulated. In order to substitute it while maintaining a good energy level alignment between the IPH and Ag, we investigated two different interface materials, PDINO and PFNBr. The energy levels of the PDINO and PFNBr are reported in Fig 5.5 and were taken from the literature.[66, 123] In PDINO the presence of amino N-oxide groups introduce a dipole moment at the metal/organic interface, lowering the effective metal work function and hence facilitating the electron transfer from the IPH to the Ag electrode. In addition, the HOMO energy of the PDINO was estimated to be −6.2 eV, which is sufficiently large to avoid hole-electron recombination at the cathode. Similarly, when the PFNBr layer was used at the cathode interface, mobile charges could redistribute under the applied bias forming dipoles, improving the charge transfer and reducing the recombination at the interface.[124]

The absorption spectra of thin films of these two materials are reported in Fig 5.5 b. A broad absorption was observed for the PDINO, due to the strong intermolecular interaction among perylenes, while only a sharp absorption

band in the UV-blue region of the electromagnetic spectrum appeared in the absorption spectrum of PFNBr. As discussed in previous chapters, in order to obtain high efficiency solar cells it is essential to obtain good quality perovskite films and a homogeneous coverage of the interface materials. Here, we studied by AFM the surface morphology of the IPH and IPH coated with the PDINO and PFNBr deposited on top of the perovskite.

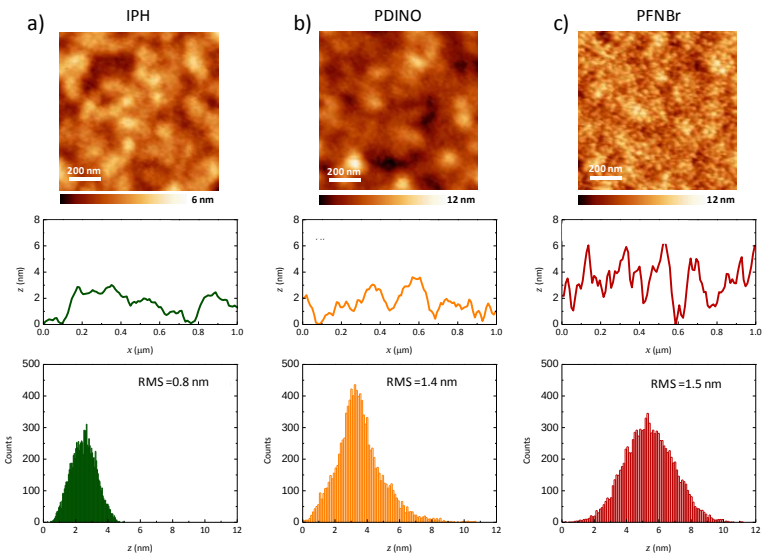

Fig 5.6 Atomic Force microscopy (AFM) characterization of the surface of a) IPH b) IPH/PDINO and c) IPH/PFNBr. All films are deposited onto an ITO/PEDOT:PSS/MAPbI$_3$ stack.

The topography of the IPH layer deposited onto the perovskite film was very flat and homogeneous, as also presented in the chapter 4. The RMS was as low as 0.8 nm. After the deposition of the two ionic interlayers, the RMS was only slightly increased to 1.4 nm for the PDINO and 1.5 nm for the PFNBr, with good surface coverage. While the morphology was maintained when the PDINO was deposited onto the IPH, PFNBr layers were composed of very fine grains with a higher peak-to-peak roughness (R_{PTP}) of 11.3 nm, as compared to the other ETLs (R_{PTP} =5.0 nm for the IPH and 10.8 nm for the IPH/PDINO). Still, in both cases the layers were sufficiently smooth, allowing the formation of high quality diodes.

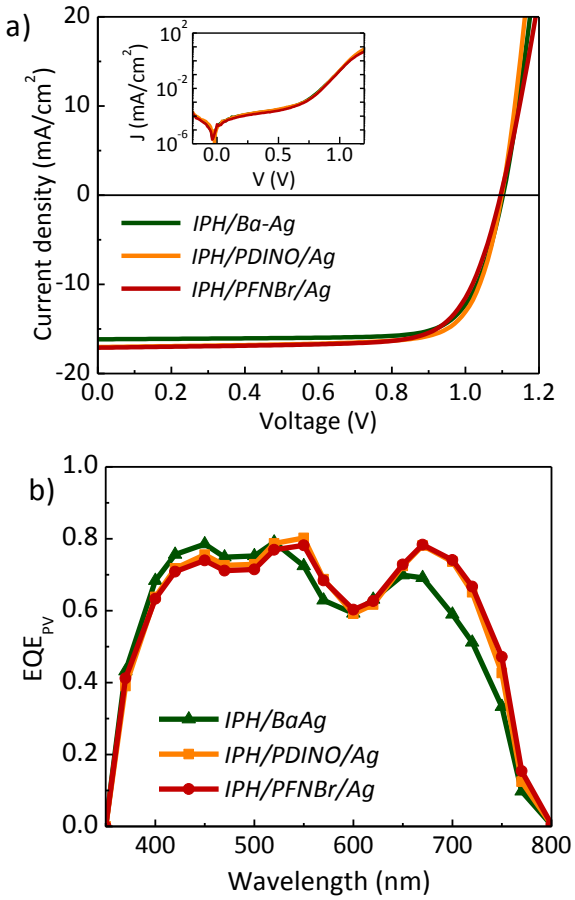

Fig 5.7 (a) J-V curves under 1 sun illumination for the devices employing different cathode interlayers; the inset shows the J-V curve collected in the dark. (b) External quantum efficiency (EQE_{PV}) of the same diodes series.

Devices employing the two different electron extraction layers (PDINO and PFNBr) and a reference with IPH/Ba-Ag were characterized by measuring the *J-V* curves both in the dark and under 1 sun illumination.

The inset in Fig 5.7a shows the dark J-V characteristics of the three devices, which were essentially identical. All of them present a low leakage current, indicative of the absence of large defects in the films and of the good quality of the diodes, in agreement with the AFM analysis. The *J-V* curves under 1 sun illumination are presented in Fig 5.7a for the three cell configurations. All of them showed good FF values ranging from 74 to 77,

indicating a good charge transport and extraction within the diodes (see table 2).

Table 2 Average photovoltaic parameters for the devices using different electron extraction layers.

	V_{oc} (mV)	J_{sc} (mA/cm^2)	*FF* (%)	*PCE* (%)
IPH/BaAg	1102	16.16	77	13.7
IPH/PDINO/Ag	1101	17.03	76	14.3
IPH/PFNBr/Ag	1096	17.10	74	13.9

The V_{oc} values were also rather high, about 1.1 V, in agreement with the low reduction potential of the IPH. No clear trend was observed, but lower FF and V_{oc} were obtained when employing the PFNBr interlayer, perhaps due to the slightly rougher surface observed by AFM. The main difference between the device series was the short circuit current density, with lower values obtained for the devices employing Ba/Ag as the electrode. The EQE_{PV} measured between 650 and 770 nm for the Ba-Ag devices is lower (EQE_{PV} ~ 0.6) compared to those obtained with PDINO and PFNBr (EQE_{PV} ~ 0.8). As a consequence of the use of Ba (which has a lower reflectance than bare Ag), the solar cell has a different optical interference and light absorption profile. The lower EQE_{PV} in the red part of the spectra most likely originated from an altered optical-field distribution within the perovskite absorber. In all of the devices the EQE_{PV} obtained in the visible range were similar (0.7 - 0.8). The highest power conversion efficiencies were obtained with PDINO as the cathode interlayer, with average values of 14.3%, and a record cell with PCE of 15.2%. All solar cells parameters are summarized in table 2 and the spreading of the data depicted in Fig 5.8.

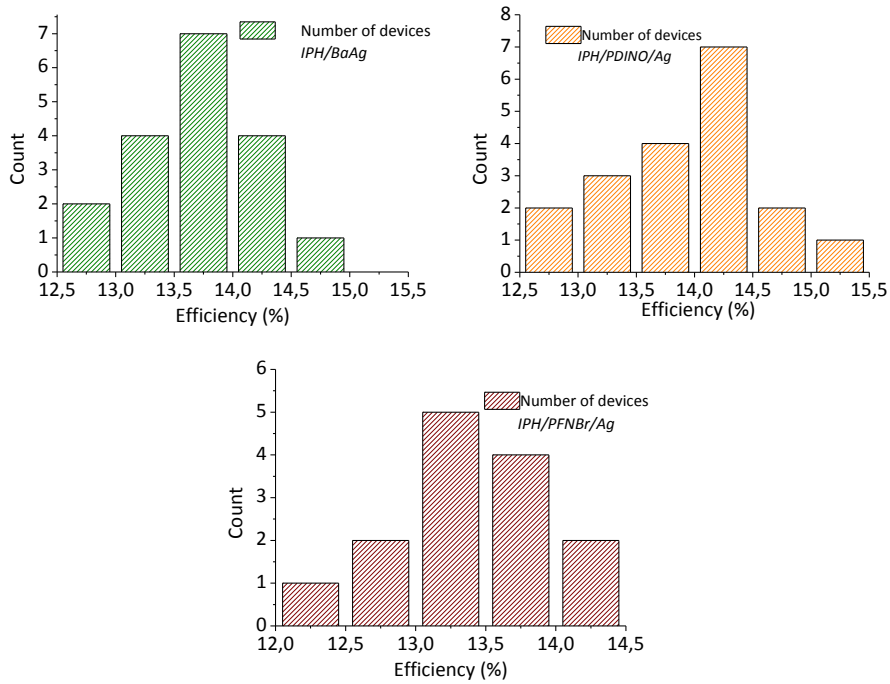

Fig 5.8 Statistics of the PCE measured for the different electron extraction layers used.

Finally, the diodes were driven under forward bias at moderate voltages (above V_{oc}, Fig 5.9) in order to study their electroluminescence. The current density was observed to be similar for all devices, with values higher than 100 mA/cm^2 at 2 V, indicating a low injection barrier and efficient charge transport in the diodes. The electroluminescence rapidly increased at applied bias of about 1 V, in agreement with irradiance values reported elsewhere.[74, 77, 86] Among the devices, both the current density and irradiance for PFNBr were found to be lower, in agreement with the hindered charge transport/extraction observed under illumination. The external quantum efficiency for electroluminescence (EQE_{EL}) of the different diodes was also evaluated.

As presented in the previous chapter, the EQE_{EL} value obtained with the IPH fullerene was 0.12%, while for the PCBM was as low as 0.04%. Interestingly, higher EQE_{EL} (0.15%) were obtained for the devices with PDINO and PFNBr layers. This increase of the radiative efficiency suggested a reduction of the

non-radiative recombination pathways when a proper interlayer was used between the ETL and the cathode.

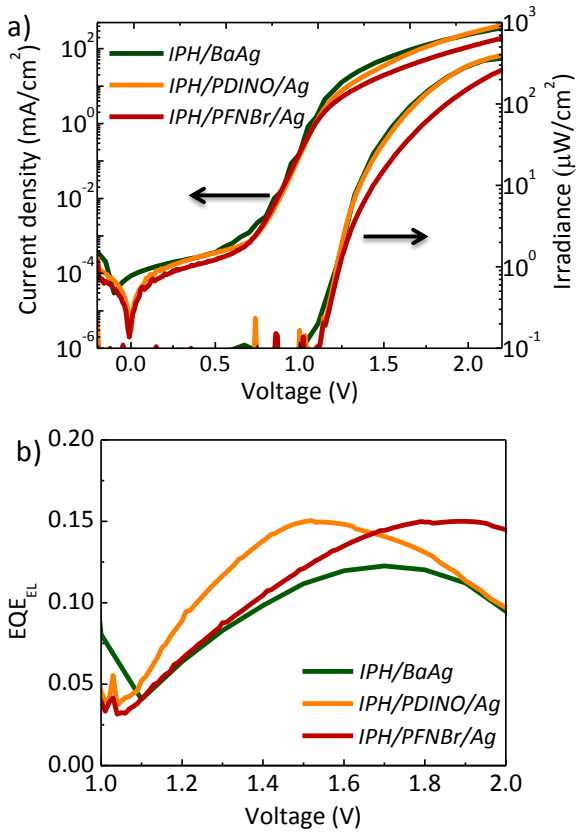

Fig 5.9 (a) Current density and irradiance versus voltage applied and (b) External quantum efficiency versus the voltage applied for the devices with different electron extraction layers.

5.5. Conclusion.

In summary, this chapter investigated the charge transport interfaces in p-i-n vacuum deposited perovskite solar cells. It was found that it is crucial to use an electron blocking/hole transport layer in between the PEDOT:PSS and the perovskite film in order to maintain the photovoltaic performance. This was due to the direct recombination of photogenerated charges at the PEDOT:PSS/perovskite interface when no polyTPD layer was added in between. On the electron transport side, we evaluated two different

electron extraction interlayers, PDINO and PFNBr. In both cases, high performances were achieved, similar or even higher to those employing low work function metals such as Ba. This effect was due to the favorable dipoles introduced by the charged molecules. As a consequence, a reduction of the non-radiative recombination at the electron injection interface was observed.

5.6. Contribution of the author

L. Gil-Escrig; C. Momblona; D. Forgács; S. Pla; F. Fernández-Lázaro; M. Sessolo; Á. Sastre-Santos; H. J. Bolink. “Interface engineering in efficient vaccum deposited perovskite solar cells” Organic electronics 37, 396-401 (2016)

Organic Electronics 37 (2016) 396–401

Contents lists available at ScienceDirect

Organic Electronics

journal homepage: www.elsevier.com/locate/orgel

Interface engineering in efficient vacuum deposited perovskite solar cells

Lidón Gil-Escrig [a], Cristina Momblona [a], Dávid Forgács [a], Sara Pla [b], Fernando Fernández-Lázaro [b], Michele Sessolo [a], Ángela Sastre-Santos [b], Henk J. Bolink [a, *]

[a] Instituto de Ciencia Molecular (ICMOL), Universidad de Valencia, 46980 Paterna, Spain
[b] Área de Química Orgánica, Instituto de Bioingeniería, Universidad Miguel Hernández, 03202 Elche, Spain

ARTICLE INFO

Article history:
Received 18 April 2016
Received in revised form
10 July 2016
Accepted 13 July 2016
Available online 22 July 2016

Keywords:
Hybrid perovskites
Solar cells
Organic transport layers
Perylene

ABSTRACT

We studied the effect of the charge transport layers in p-i-n perovskite solar cells using vacuum deposited methylammonium lead iodide thin-film absorbers. While solution-processed perovskite films are frequently deposited directly on PEDOT:PSS leading to good solar cell performances, in some cases even to very good V_{oc} values, we show that in devices employing vacuum deposited $MAPbI_3$ perovskites, the removal of the polyTPD electron blocker substantially reduces the photovoltaic behavior. This is indicative of rather different charge transport properties in the vacuum deposited $MAPbI_3$ perovskites compared to those prepared from solution. On the other hand, we investigated the use of ionic interlayers as a possible alternative to low work function electrodes, whose reactivity towards air and moisture compromises the device stability. Two different electron extraction materials were evaluated as interlayers between the fullerene electron transport layer and a silver electrode, in particular a perylenediimide derivative and a conjugated polyelectrolyte. By studying the photovoltaic response and the electroluminescence properties of planar diodes using the ionic films and comparing them with devices employing barium, we found that such ionic interlayers can successfully replace the use of reactive electrodes, since they facilitate the electron extraction while reducing the non-radiative recombination at the electron transport interface.

1. Introduction

Organometal halide perovskites have recently attracted a wide interest in photovoltaic applications because of their impressive efficiencies, now exceeding 21% [1–3]. The perovskite film can be deposited by solution processing or vacuum techniques. Vacuum deposition is an attractive method with a wide implementation in the semiconductor industry. It has a number of benefits, including material purity, fine control over deposition parameters (*e.g.* deposition rate, thickness and stoichiometry) and high reproducibility, and has been used in the preparation of high-efficiency photovoltaic devices [4–9]. Two different configurations have been reported so far. In the n-i-p configuration the perovskite is deposited onto a TiO_2 layer. Such architecture typically requires a high temperature thermal treatment, as a result it cannot be directly implemented on plastic foils or in multi-junctions devices [7,10–12]. The alternative structure is the p-i-n, where the perovskite films are deposited on top of transparent substrates covered with a conducting polymer, mostly poly(3,4-ethyl-enedioxythiophene) doped with poly(styrenesulfonate) (PEDOT:PSS). However, PEDOT:PSS does not block the electrons and there is a large difference between the PEDOT:PSS work function (WF, −5.0/-5.1 eV) and the valence band edge of perovskite absorbers such as methylammonium lead iodide ($MAPbI_3$, −5.4 eV). This difference may cause losses in built-in potential of the devices. Moreover, without an electron blocking layer, electron-hole recombination can occur at the perovskite-PEDOT:PSS interface which leads to a decrease of all the photovoltaic parameters such as the open circuit voltage, fill factor and the short circuit current density (V_{oc}, FF and J_{sc}, respectively). Many approaches have been developed in order to reduce the energy offset between the PEDOT:PSS and the perovskite. Lim *et al.* developed a hole extraction layer with a high WF composed of a blend of PEDOT:PSS and a perfluorinated ionomer. The increase in the WF allowed to align the energy levels and hence to increase the efficiency of the devices [13]. Small molecular

* Corresponding author.
E-mail address: henk.bolink@uv.es (H.J. Bolink).

http://dx.doi.org/10.1016/j.orgel.2016.07.019
1566-1199/

weight organic semiconductors (commonly named as small molecules) have been also used to tune the energy levels at the interface between the electrode and the perovskite. Polander *et al.* showed a gradual increase in V_{oc} due to a reduction of the energy level difference between the hole extraction layer and the perovskite [8]. Polymer electrolyte have also been successfully applied as hole transport layers in perovskite solar cells, enhancing charge transport and limiting electron-hole recombination at the electrode interface [14]. Different kinds of p-type polymeric organic semiconductors were introduced by Lin et al. to reduce the potential mismatch at the interface between PEDOT:PSS and the $MAPbI_3$ perovskite [6]. In general, polymers with higher ionization potential showed higher V_{oc} values. Our group has extensively used thin electron blocking layer of polyTPD, poly[*N*,*N*′-di(4-butylphenyl)-*N*,*N*′-diphenylbenzidine], a hole transport arylamine-based polymer, in between the PEDOT:PSS and the perovskite absorber [5,15–19]. As the polyarylamine layer is apolar, the solution processing of the perovskite is not straightforward on top of this layer. However, when the perovskite is deposited using vacuum-based processes, compact and homogeneous films can be formed onto the electron blocking layer.

In the p-i-n configuration, [6,6]-phenyl-C61 butyric acid methyl ester (PCBM) is the most widely used electron transport material because of its excellent electron transport properties. Apart from PCBM, other fullerene derivatives have been used, achieving efficiencies of 16.3% and 15.44% with $PC_{71}BM$ and C_{60}, respectively [20,21]. Recently, five different fullerenes were evaluated in our group as hole blocking/electron transport materials. We observed an enhancement of the solar cell performance when the indene-C_{60}-propionic acid hexyl ester (IPH) was used [22], reaching efficiency values of 14.6%. Extensive work has been carried out in order to reduce the mismatch in the energy levels between the fullerene electron affinity and the metal contact WF (Al, Ag or Au), mostly by inserting additional interlayers. Ethoxylated polyethylenimine (PEIE) or poly[3-(6-trimethylammoniumhexyl)thiophene] (P3TMAHT) were introduced in between the PCBM and the Ag cathode to create a quasi-ohmic contact, as a consequence of the formation of interface dipoles with a negative charge on Ag [23]. Similarly, a chemisorbed dipolar interface layer based on an amine-functionalized fullerene derivative, DMAPA-C_{60}, was used in between the PCBM and the Ag electrode [24]. Docampo *et al.* developed a high efficiency perovskite solar cell by depositing an n-type TiO_x layer between PCBM and Al [25]. In addition the bis-C_{60} surfactant and amino-functionalized polymer (PN4N) were also employed as effective electron-selective interfacial layer [26,27]. Finally, layers such as LiF or low WF metals such as Ba are commonly used in order to have ohmic contact and efficient charge extraction [19,28], but these materials are very reactive with air and oxygen. Other vacuum deposited layers can be introduced in between the PCBM and the metal cathode, *i.e.* bathocuproine (BCP), fullerene (C_{60}) or ZnO [29–31].

Here, we report on the effect of employing electron blocking materials in combination with ionic interlayers on the performance of solar cells using a vacuum deposited $MAPbI_3$ perovskite absorber. Two different electron extraction materials are evaluated in p-i-n vacuum deposited perovskite solar cells. In particular, a perylenediimide derivative, *N*,*N*′-bis(dimethylaminopropyl-*N*‴-oxide)-perylene-3,4:9,10-tetracarboxidiimide (PDINO) and a poly{(9,9-bis[3′-(*N*,*N*,*N*-ethyldimethylammonium)propyl]- fluorene-2,7-diyl) dibromide -alt- (9,9-dioctylfluorene-2,7-diyl)} (PFNBr) are solution processed in between the fullerene derivative (IPH) and the Ag cathode [21,32–34]. Also, we evaluate the need of an electron blocking layer (polyTPD) in between the PEDOT:PSS and the perovskite. By simultaneously using the electron blocking layer and the ionic interlayer, solar cells with high power conversion efficiencies (PCEs) are obtained.

2. Experimental

Photolithographically patterned indium tin oxide (ITO) coated glass substrates were purchased from Naranjo-substrates (http://www.naranjosubstrates.com). PEDOT:PSS (Clevios™ P VP AI 4083) was obtained from Heraeus. PbI_2 was purchased from Sigma Aldrich and CH_3NH_3I and PFNBr from Lumtec, all of them were used as received. The IPH fullerene was purchased from Solenne BV. The PDINO was synthesized according to a previously published protocol [32].

ITO-coated glass substrates were subsequently cleaned with soap, water and isopropanol in an ultrasonic bath, followed by O_2 plasma treatment. PEDOT:PSS was spin-coated on top and annealed at 150° for 15 min. On top of this layer a thin film of polyTPD was deposited from a chlorobenzene solution (7 mg ml^{-1}). The substrates were transferred to a vacuum chamber integrated in a nitrogen-filled glovebox (O_2 < 0.1 ppm and H_2O < 0.1 ppm) and evacuated to a pressure of 10^{-6} mbar. Two ceramic crucibles were filled with CH_3NH_3I and PbI_2 and heated to 70 °C and 250 °C, respectively. The film thickness was controlled by the PbI_2 sublimation at a rate of 0.5 A s^{-1}. The fullerene layer was deposited by spin coating of its chlorobenzene solution (20 mg ml^{-1}) in air. Hence, a thin layer of PDINO or PFNBr was spin coated from a methanol solution (concentrations of 1 mg ml^{-1} or 2 mg ml^{-1}, respectively) on top of the fullerene layer. The devices were completed by the thermal evaporation of the top electrode under a base pressure of $2 \cdot 10^{-6}$ mbar to a thickness of 100 nm of Ag or Ba/Ag (10/100 nm).

The device external quantum efficiency (EQE) was estimated using the cell response at different wavelengths (measured with a white light halogen lamp in combination with band-pass filters), where the solar spectrum mismatch was corrected using a calibrated Silicon reference cell (MiniSun simulator by ECN, the Netherlands). The current density-voltage (J-V) characteristics were obtained using a Keithley 2400 source measure unit and under white light illumination, and the short circuit current density was corrected taking into account the device EQE. The electrical characterization was validated using a solar simulator by Abet Technologies (model 10500 with an AM1.5G xenon lamp as the light source). Before each measurement, the exact light intensity was determined using a calibrated Si reference diode equipped with an infrared cut-off filter (KG-3, Schott). Importantly, no differences in the J-V characteristics obtained with the different evaluation method were observed. The current-density versus voltage (*J-V*) and irradiance versus voltage (*L-V*) characteristics were obtained using a Keithley Model 2400 source measurement unit and a Si-photodiode coupled to an integrated sphere, respectively.

3. Results and discussion

Fig. 1a shows the typical p-i-n device structure employed, ITO/PEDOT:PSS/polyTPD/$MAPbI_3$/IPH/PDINO or PFNBr/Ba-Ag or Ag. The crystallinity of the vacuum deposited perovskite was investigated by grazing incidence X-ray diffraction (GIXRD) measurements, revealing the typical $MAPbI_3$ diffraction pattern (in terms of both peak position and relative intensity), as shown in Fig. S1a. The absorption spectrum (Fig. S1b) also confirms the formation of the perovskite. Initially, we studied the effect of the polyTPD electron blocking layer on the device performance. From the J-V curves in the dark (Fig. 2a), a typical diode behavior can be observed for both devices, yet the one with no blocking layer shows a lower built-in potential and higher current density compared to the reference device with the polyTPD layer. By looking at the diode ideality

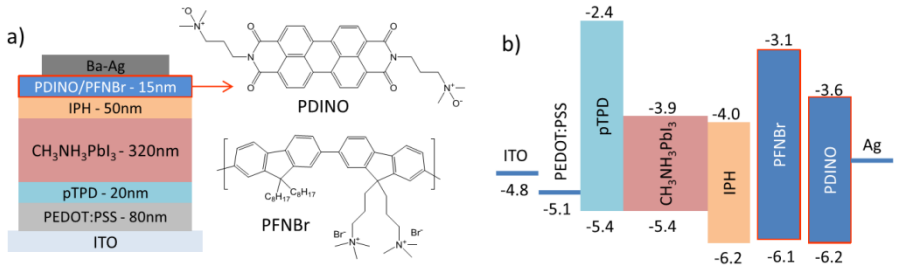

Fig. 1. (a) Device schematics of the p-i-n perovskite solar cell with the molecular structures of the PDINO and PFNBr. (b) Flat energy band diagram for the materials used in the device preparation.

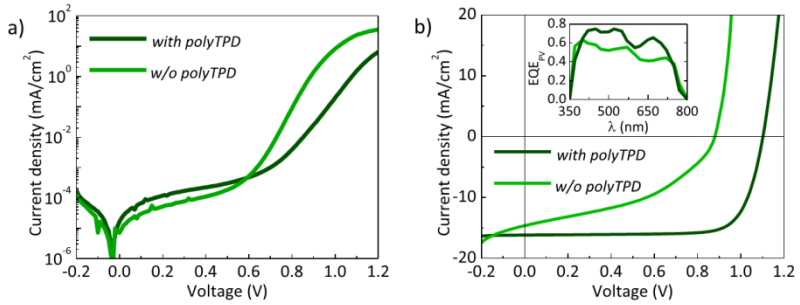

Fig. 2. J-V curves in the dark (a) and under illumination (b) for devices with and without polyTPD. The electron extraction interface used for these cells is IPH/Ba-Ag. The inset in (b) show the correspondent photovoltaic external quantum efficiency (EQE_{PV}).

factor (η, Fig. S2), one can observe how the device without the polyTPD shows an increased direct charge recombination at the PEDOT:PSS contact (η closer to 1) as compared to the reference device, for which the recombination is mostly trap-assisted (η ~ 2), in agreement with previous reports [35]. The minimum of the current density is not at applied bias V = 0, most likely due to partial charging of the cells during the voltage sweep from −0.2 V to 0 V, where some amount of charges accumulates at one of the device interfaces. The devices performance under illumination (Fig. 2b) suggests that in the absence of the electron blocking polyTPD films, the photogenerated charge carriers do recombine at the PEDOT:PSS/$MAPbI_3$ interface. In fact, the V_{oc} of the device without polyTPD (0.88 V) is much lower compared to the one with the blocking layer (1.10 V). This is also a consequence of the lower WF of the PEDOT:PSS as compared to the polyTPD ionization potential, which helps maintaining the device photovoltage. The direct charge recombination and the lower built-in potential of the device without polyTPD causes a decrease of the FF and of the current density, strongly undermining the overall solar cell performance. Hence, in vacuum deposited perovskite cells, the presence of a hole transport layer in between the PEDOT:PSS and the absorber is needed to guarantee proper device functioning. This is indicative of rather different charge transport properties in the vacuum deposited $MAPbI_3$ perovskites compared to those prepared from solution. This is an important observation as for solar cells employing perovskite absorbers having high electron and hole mobilities one does expect that optimum performing devices are obtained with charge selective (or blocking) layers on both sides of the absorber. This may well be the reason why perovskite solar cells deposited on metal oxides (TiO_2, ZnO) generally perform better then their inverted counterparts, as with the metal oxide the perovskite layer is sandwiched in between two charge selective layers.

As already mentioned, Ba is very unstable and it severely affects the stability of the devices. Hence, in order to substitute it and overcome the mismatch of the energy levels among IPH and Ag, we incorporated an extraction layer (composed of either PDINO or PFNBr) between the IPH and the Ag cathode. The energy levels of the PDINO and the PFNBr were reported elsewhere (see Fig. 1b) [32,36]. The presence of amino *N*-oxide groups in the PDINO introduces large dipole moments at the metal/organic interface, substantially lowering the metal WF and hence facilitating the electron transfer from the IPH to the Ag electrode. In addition, the deeper highest occupied molecular orbital (HOMO) of the PDINO helps the hole confinement in the perovskite. Similarly, the incorporation of the PFNBr layer assists the electron extraction from the IPH to Ag by formation of an ohmic contact, as mobile charges can redistribute under the applied bias forming dipoles, improving the charge-transfer and reducing the recombination at the interface [37].

The absorption spectra of these two materials are reported in Fig S3. A broad absorption is observed for the PDINO, due to the efficient perylene stacking, while a sharp peak appears in the absorption spectra of the PFNBr material. A uniform and compact perovskite film and its homogeneous coverage with the interface material is imperative to obtain high performing solar cells. The topography of the IPH layer deposited onto the perovskite, as obtained by atomic force microscopy, is very flat and homogeneous, with a root-mean-square roughness (R_{RMS}) of 0.8 nm. Once

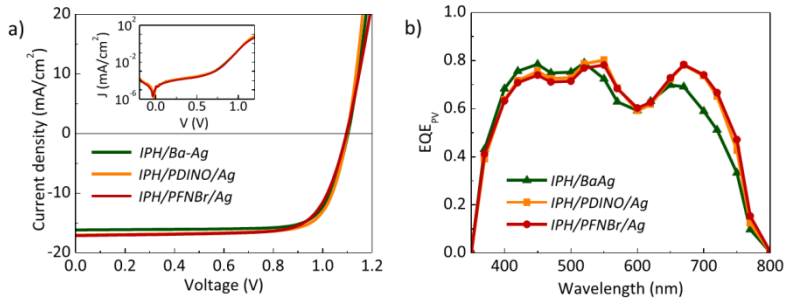

Fig. 3. (a) J-V curves under 1 sun illumination for the devices employing different electron transport layers; the inset shows the J-V curve collected in the dark. (b) External quantum efficiency (EQE_{PV}) of the same diodes series.

Table 1
Average photovoltaic parameters for the devices using different electron extraction layers.

	V_{oc} (mV)	J_{sc} (mA/cm^2)	FF (%)	PCE (%)
IPH/Ba/Ag	1102	16.16	77	13.7
IPH/PDINO/Ag	1101	17.03	76	14.3
IPH/PFNBr/Ag	1096	17.10	74	13.9

subsequently coated with PDINO or PFNBr, such flat morphology is maintained, with R_{RMS} only slightly enlarged to 1.4 nm and 1.5 nm, respectively. While the PDINO layer is essentially conformal to the IPH, the PFNBr film shows a different morphology, with very fine grains and a higher peak-to-peak roughness (R_{PTP}) of 11.3 nm (R_{PTP} = 5.0 nm for the IPH and 10.8 nm for the IPH/PDINO). Anyhow, in both cases the layers are rather smooth, allowing for the preparation of high quality diodes.

Devices employing the two different extraction layers (PDINO and PFNBr) and the reference device with Ba/Ag as the electrode were characterized by determining the J-V curves both in the dark and under 1 sun illumination. The inset of Fig. 3a shows the dark J-V characteristics for the three devices, which are essentially identical. The leakage current is very low, indicative of the absence of defects in the diodes and especially in the transport layers used. The photovoltaic behavior under 1 sun illumination for the same devices is shown in Fig. 3a. As expected from the good diode characteristics, high fill factors ranging from 74 to 77 were obtained (see Table 1). The solar cells V_{oc} are very high, approximately 1.1 V for all devices, in agreement with the lower reduction potential of the IPH [22]. No clear trend is observed, although slightly lower FFs and V_{oc} were measured when the PFNBr layer was deposited in between the IPH and the Ag cathode. Interestingly, the short-circuit current density (J_{sc}) of the solar cells was found to be lower when the barium was used as the electrode. In devices using Ba/Ag the lower current density is related with the reduction in the external quantum efficiency (EQE_{pv}) at lower wavelength (Fig. 3b). The measured EQE_{pv} between 650 and 770 nm for the Ba/Ag-capped devices is lower (EQE_{PV} ~0.6) compared to those obtained for the cells employing PDINO and PFNBr (EQE_{PV} ~0.8). As a consequence of the use of Ba/Ag (which has a lower reflectance compared to bare Ag, Fig S7), the solar cell has a different optical interference and hence light absorption profile. The lower EQE_{PV} in the red part of the spectra most likely originates from an altered optical-field distribution within the perovskite absorber [38]. In all of the devices, EQE_{PV} values of 0.7–0.8 were obtained in the visible range.

Finally, the best power conversion efficiencies were obtained when the PDINO was deposited as the electron extraction layer, reaching values of 14.3% on average, and a record cell of 15.2%. The key parameters are summarized in Table 1, whereas the spreading of the data is represented in Fig S6. No hysteresis was observed when a scan speed of 250 mV s^{-1} was used for the J-V measurements, and the forward and reverse characteristics were virtually identical (Fig S5).

In Fig. 4a, the electroluminescence characterization (J-V and L-V) is presented for the same device series. The current density reaches values higher than 100 mA/cm^2 at 2 V, indicating low carrier

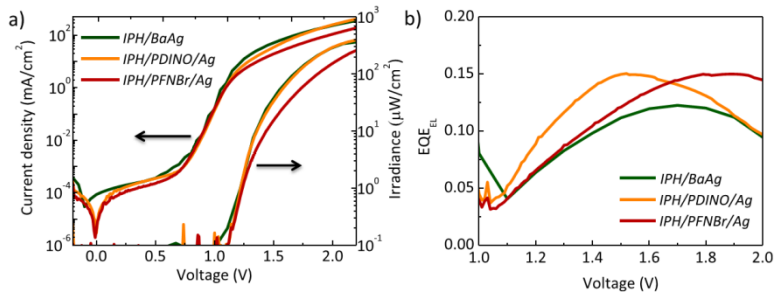

Fig. 4. (a) Current density and radiance *versus* voltage applied. (c) External quantum efficiency *versus* the voltage applied for the different extraction layer used.

injection barriers and efficient charge transport in the diodes. The irradiance rapidly increases with a turn-on voltage of 1 about V, in agreement with electroluminescent devices published elsewhere [39–41]. The correspondent maximum external quantum efficiency for electroluminescence (EQE_{EL}) of the diodes change slightly depending on the interlayer deposited on top of the IPH fullerene, see Fig. 4b. In previous studies, EQE_{EL} of 0.12% was reached by using the IPH fullerene derivative, while for diodes using PCBM an EQE_{EL} of 0.04% was obtained [39–41]. Interestingly, higher EQE_{EL} (0.15%) have been obtained for the devices using PDINO and PFNBr layers. This increase of the radiative efficiency suggests a reduction in non-radiative recombination pathways when the barium layer is removed.

4. Conclusions

In summary, we investigated the charge transport interfaces in p-i-n vacuum deposited perovskite solar cells. We found that a polyTPD hole transport (and electron blocking) layer in between the PEDOT:PSS and the perovskite is needed in order to avoid direct charge recombination and to enhance the device photovoltage. On the electron transport side, we evaluated PDINO and PFNBr as electrode interlayers, and obtained similar or even higher higher power conversion efficiency compared to devices employing low WF metals such as Ba. This is a consequence of the favorable dipoles introduced by the charged molecules, facilitating the electron extraction while reducing the non-radiative recombination at the electron transport interface.

Acknowledgment

We acknowledge financial support from the European Union H2020 project INFORM (grant 675867), the Spanish Ministry of Economy and Competitiveness (MINECO) via the Unidad de Excelencia María de Maeztu MDM-2015-0538, MAT2014-55200-R, CTQ2014-55798-R and PCIN-2015-255 and the Generalitat Valenciana (Prometeo/2012/053, Prometeo 2012/010). C. M. and M.S. thank the MINECO for their pre- and post-doctoral (JdC) contracts.

Appendix A. Supplementary data

Supplementary data related to this article can be found at http://dx.doi.org/10.1016/j.orgel.2016.07.019.

References

[1] A. Kojima, K. Teshima, Y. Shirai, T. Miyasaka, Organometal halide perovskites as visible-light sensitizers for photovoltaic cells, J. Am. Chem. Soc. 131 (2009) 6050–6051.
[2] M.M. Lee, J. Teuscher, T. Miyasaka, T.N. Murakami, H.J. Snaith, Efficient hybrid solar cells based on meso-superstructured organometal halide perovskites, Science 338 (2012) 643–647.
[3] W.S. Yang, J.H. Noh, N.J. Jeon, Y.C. Kim, S. Ryu, J. Seo, S.I. Seok, High-performance photovoltaic perovskite layers fabricated through intramolecular exchange, Science 348 (2015) 1234–1237.
[4] M. Liu, M.B. Johnston, H.J. Snaith, Efficient planar heterojunction perovskite solar cells by vapour deposition, Nature 501 (2013) 395–398.
[5] O. Malinkiewicz, A. Yella, Y.H. Lee, G.M. Espallargas, M. Graetzel, M.K. Nazeeruddin, H.J. Bolink, Perovskite solar cells employing organic charge-transport layers, Nat. Phot. 8 (2014) 128–132.
[6] M. Sessolo, C. Momblona, L. Gil-Escrig, H.J. Bolink, Photovoltaic devices employing vacuum-deposited perovskite layers, MRS Bull. 40 (2015) 660–666.
[7] Q. Chen, H. Zhou, Z. Hong, S. Luo, H.-S. Duan, H.-H. Wang, Y. Liu, G. Li, Y. Yang, Planar heterojunction perovskite solar cells via vapor-assisted solution process, J. Am. Chem. Soc. 136 (2014) 622–625.
[8] L.E. Polander, P. Pahner, M. Schwarze, M. Saalfrank, C. Koerner, K. Leo, Hole-transport material variation in fully vacuum deposited perovskite solar cells, APL Mater. 2 (2014) 081503.
[9] L.K. Ono, M.R. Leyden, S. Wang, Y. Qi, Organometal halide perovskite thin films and solar cells by vapor deposition, J. Mater. Chem. A 4 (2016) 6693–6713.
[10] S.D. Stranks, G.E. Eperon, G. Grancini, C. Menelaou, M.J.P. Alcocer, T. Leijtens, L.M. Herz, A. Petrozza, H.J. Snaith, Electron-hole diffusion lengths exceeding 1 micrometer in an organometal trihalide perovskite absorber, Science 342 (2013) 341–344.
[11] G.E. Eperon, V.M. Burlakov, P. Docampo, A. Goriely, H.J. Snaith, Morphological control for high performance, solution-processed planar heterojunction perovskite solar cells, Adv. Funct. Mater. 24 (2014) 151–157.
[12] B. Conings, L. Baeten, C. De Dobbelaere, J. D'Haen, J. Manca, H.-G. Boyen, Perovskite-based hybrid solar cells exceeding 10% efficiency with high reproducibility using a thin film sandwich approach, Adv. Mater. 26 (2014) 2041–2046.
[13] K.-G. Lim, H.-B. Kim, J. Jeong, H. Kim, J.Y. Kim, T.-W. Lee, Boosting the power conversion efficiency of perovskite solar cells using self-organized polymeric hole extraction layers with high work function, Adv. Mater. 26 (2014) 6461–6466.
[14] X. Li, X. Liu, X. Wang, L. Zhao, T. Jiu, J. Fang, Polyelectrolyte based hole-transporting materials for high performance solution processed planar perovskite solar cells, J. Mater. Chem. A 3 (2015) 15024–15029.
[15] K. Tvingstedt, O. Malinkiewicz, A. Baumann, C. Deibel, H.J. Snaith, V. Dyakonov, H.J. Bolink, Radiative efficiency of lead iodide based perovskite solar cells, Sci. Rep. 4 (2014) 6071.
[16] C. Roldan-Carmona, O. Malinkiewicz, A. Soriano, G. Minguez Espallargas, A. Garcia, P. Reinecke, T. Kroyer, M.I. Dar, M.K. Nazeeruddin, H.J. Bolink, Flexible high efficiency perovskite solar cells, Energy Environ. Sci. 7 (2014) 994–997.
[17] C. Roldan-Carmona, O. Malinkiewicz, R. Betancur, G. Longo, C. Momblona, F. Jaramillo, L. Camacho, H.J. Bolink, High efficiency single-junction semi-transparent perovskite solar cells, Energy Environ. Sci. 7 (2014) 2968–2973.
[18] C. Momblona, O. Malinkiewicz, C. Roldán-Carmona, A. Soriano, L. Gil-Escrig, E. Bandiello, M. Scheepers, E. Edri, H.J. Bolink, Efficient methylammonium lead iodide perovskite solar cells with active layers from 300 to 900 nm, APL Mater. 2 (2014) 081504.
[19] O. Malinkiewicz, C. Roldán-Carmona, A. Soriano, E. Bandiello, L. Camacho, M.K. Nazeeruddin, H.J. Bolink, Metal-oxide-free methylammonium lead iodide perovskite-based solar cells: the influence of organic charge transport layers, Adv. Energy Mater. 4 (2014) 1400345.
[20] C.-H. Chiang, Z.-L. Tseng, C.-G. Wu, Planar heterojunction perovskite/PC71BM solar cells with enhanced open-circuit voltage via a (2/1)-step spin-coating process, J. Mater. Chem. A 2 (2014) 15897–15903.
[21] J. You, Y. Yang, Z. Hong, T.-B. Song, L. Meng, Y. Liu, C. Jiang, H. Zhou, W.-H. Chang, G. Li, Y. Yang, Moisture assisted perovskite film growth for high performance solar cells, Appl. Phys. Lett. 105 (2014) 183902.
[22] L. Gil-Escrig, C. Momblona, M. Sessolo, H.J. Bolink, Fullerene imposed high open-circuit voltage in efficient perovskite based solar cells, J. Mater. Chem. A 4 (2016) 3667–3672.
[23] H. Zhang, H. Azimi, Y. Hou, T. Ameri, T. Przybilla, E. Spiecker, M. Kraft, U. Scherf, C.J. Brabec, Improved high-efficiency perovskite planar heterojunction solar cells via incorporation of a polyelectrolyte interlayer, Chem. Mater. 26 (2014) 5190–5193.
[24] H. Azimi, T. Ameri, H. Zhang, Y. Hou, C.O.R. Quiroz, J. Min, M. Hu, Z.-G. Zhang, T. Przybilla, G.J. Matt, E. Spiecker, Y. Li, C.J. Brabec, A universal interface layer based on an amine-functionalized fullerene derivative with dual functionality for efficient solution processed organic and perovskite solar cells, Adv. Energy Mater. 5 (2015) 1401692.
[25] P. Docampo, J.M. Ball, M. Darwich, G.E. Eperon, H.J. Snaith, Efficient organometal trihalide perovskite planar-heterojunction solar cells on flexible polymer substrates, Nat. Commun. 4 (2013) 2761.
[26] P.-W. Liang, C.-Y. Liao, C.-C. Chueh, F. Zuo, S.T. Williams, X.-K. Xin, J. Lin, A.K.Y. Jen, Additive enhanced crystallization of solution-processed perovskite for highly efficient planar-heterojunction solar cells, Adv. Mater. 26 (2014) 3748–3754.
[27] Q. Xue, Z. Hu, J. Liu, J. Lin, C. Sun, Z. Chen, C. Duan, J. Wang, C. Liao, W.M. Lau, F. Huang, H.-L. Yip, Y. Cao, Highly efficient fullerene/perovskite planar heterojunction solar cells via cathode modification with an amino-functionalized polymer interlayer, J. Mater. Chem. A 2 (2014) 19598–19603.
[28] J. Seo, S. Park, Y. Chan Kim, N.J. Jeon, J.H. Noh, S.C. Yoon, S.I. Seok, Benefits of very thin PCBM and LiF layers for solution-processed p-i-n perovskite solar cells, Energy Environ. Sci. 7 (2014) 2642–2646.
[29] Z. Xiao, C. Bi, Y. Shao, Q. Dong, Q. Wang, Y. Yuan, C. Wang, Y. Gao, J. Huang, Efficient, high yield perovskite photovoltaic devices grown by interdiffusion of solution-processed precursor stacking layers, Energy Environ. Sci. 7 (2014) 2619–2623.
[30] Q. Wang, Y. Shao, Q. Dong, Z. Xiao, Y. Yuan, J. Huang, Large fill-factor bilayer iodine perovskite solar cells fabricated by a low-temperature solution-process, Energy Environ. Sci. 7 (2014) 2359–2365.
[31] W. Qiu, T. Merckx, M. Jaysankar, C. Masse de la Huerta, L. Rakocevic, W. Zhang, U.W. Paetzold, R. Gehlhaar, L. Froyen, J. Poortmans, D. Cheyns, H.J. Snaith, P. Heremans, Pinhole-free perovskite films for efficient solar modules, Energy Environ. Sci. 9 (2016) 484–489.
[32] Z.-G. Zhang, B. Qi, Z. Jin, D. Chi, Z. Qi, Y. Li, J. Wang, Perylene diimides: a thickness-insensitive cathode interlayer for high performance polymer solar cells, Energy Environ. Sci. 7 (2014) 1966–1973.
[33] J. Min, Z.-G. Zhang, Y. Hou, C.O. Ramirez Quiroz, T. Przybilla, C. Bronnbauer,

F. Guo, K. Forberich, H. Azimi, T. Ameri, E. Spiecker, Y. Li, C.J. Brabec, Interface engineering of perovskite hybrid solar cells with solution-processed perylene–diimide heterojunctions toward high performance, Chem. Mater. 27 (2015) 227–234.
[34] Z. He, C. Zhong, S. Su, M. Xu, H. Wu, Y. Cao, Enhanced power-conversion efficiency in polymer solar cells using an inverted device structure, Nat. Phot. 6 (2012) 591–595.
[35] G.-J.A.H. Wetzelaer, M. Scheepers, A.M. Sempere, C. Momblona, J. Ávila, H.J. Bolink, Trap-assisted non-radiative recombination in organic–inorganic perovskite solar cells, Adv. Mater. 27 (2015) 1837–1841.
[36] J.H. Seo, T.-Q. Nguyen, Electronic properties of conjugated polyelectrolyte thin films, J. Am. Chem. Soc. 130 (2008) 10042–10043.
[37] Z. He, C. Zhong, X. Huang, W.-Y. Wong, H. Wu, L. Chen, S. Su, Y. Cao, Simultaneous enhancement of open-circuit voltage, short-circuit current density, and fill factor in polymer solar cells, Adv. Mater. 23 (2011) 4636–4643.
[38] Q. Lin, A. Armin, R.C.R. Nagiri, P.L. Burn, P. Meredith, Electro-optics of perovskite solar cells, Nat. Phot. 9 (2015) 106–112.
[39] L. Gil-Escrig, G. Longo, A. Pertegas, C. Roldan-Carmona, A. Soriano, M. Sessolo, H.J. Bolink, Efficient photovoltaic and electroluminescent perovskite devices, Chem. Commun. 51 (2015) 569–571.
[40] Z.-K. Tan, R.S. Moghaddam, M.L. Lai, P. Docampo, R. Higler, F. Deschler, M. Price, A. Sadhanala, L.M. Pazos, D. Credgington, F. Hanusch, T. Bein, H.J. Snaith, R.H. Friend, Bright light-emitting diodes based on organometal halide perovskite, Nat. Nano 9 (2014) 687–692.
[41] Y.-H. Kim, H. Cho, J.H. Heo, T.-S. Kim, N. Myoung, C.-L. Lee, S.H. Im, T.-W. Lee, Multicolored organic/inorganic hybrid perovskite light-emitting diodes, Adv. Mater. 27 (2015) 1248–1254.

Chapter 6.

Conclusions.

The aim of this thesis was the development of materials and thin-film deposition techniques for the fabrication of vacuum deposited perovskite solar cells. The role of the interface between the perovskite and the charge transport materials has been studied in details, highlighting the importance of reducing non-radiative recombination at the interface in order to maintain a high photovoltage.

In chapter 3 a novel approach to prepare mixed iodide-bromide perovskites, using vacuum deposition techniques, was presented. The amount of bromide in the mixed halide compound was controlled by the thickness of the $MAPbBr_3$ perovskite deposited on top of the $MAPbI_3$ perovskite. Solar cells using a perovskite with a bandgap of 1.7 eV were prepared, leading to promising power conversion efficiency, which is particularly interesting as they can be applied as top cells in a tandem configuration with Si or CIGS cells. We also established a limit for the full interdiffusion of the two separate perovskite films, above which the carrier recombination in the film dominates the device behavior, decreasing the photovoltaic performance.

The importance of the selection of a suitable electron transport layer was highlighted in chapter 4. In this work, the perovskite layer was deposited by dual source thermal evaporation. Five different fullerene derivatives with different alkyl chains were tested in a p-i-n configuration. The layers of the fullerene derivatives with longer alkyl chains presented fewer defects when deposited on top of the perovskite film. As a result, these fullerenes lead to enhanced performances when used in solar cells, essentially due to an improvement of the V_{oc}. By measuring the devices as light-emitting diodes, an improvement of the external quantum efficiency for electroluminescence was achieved when fullerenes with longer alkyl chains were tested, indicating a reduction of the non-radiative recombination. Hence, these fullerene derivatives are very promising as cathode interlayers in perovskite solar cells.

The electrode interfaces were further studied in chapter 5, again using p-i-n perovskite solar cells. First, the importance of using an electron blocking layer between the perovskite and the PEDOT:PSS was discussed. In the absence of the polyTPD layer, severe charge recombination was observed at the PEDOT:PSS interface, leading to poor performances in the perovskite

solar cells. In addition, two different cathode interlayers were evaluated as candidates to substitute low work function metals electrodes. Enhanced efficiencies were obtained when a thin layer of PDINO or PFNBr was deposited by solution processing in between the fullerene and Ag electrode. The formation of interfacial dipoles helps the charge transfer from the IPH to Ag reducing charge recombination at that interface. This reduction was confirmed by electroluminescence measurements on the same devices, as the EQE_{EL} using the PDINO and the PFNBr layers was much higher compared to cells with Ba electrode.

Chapter 7.

Resumen en castellano.

Capítulo 1: Introducción

1.1. Introducción

El consumo global de energía está en continuo crecimiento. Por esta razón, es necesario encontrar fuentes de energía limpias, baratas y renovables, que supongan una alternativa viable frente a los combustibles fósiles, como son el gas, el petróleo o el carbón. Una posible alternativa es la tecnología fotovoltaica. En este ámbito, las células solares de silicio representan la tecnología más madura, tanto a nivel tecnológico como comercial. Sin embargo, a pesar de ser eficientes y estables, su precio elevado (debido esencialmente al coste de producción) sigue impulsando la búsqueda de tecnologías alternativas. En los últimos años ha empezado a desarrollarse una nueva generación de células solares muy prometedoras, basadas en la perovskita orgánica-inorgánica (híbrida) como material absorbente de luz.

Las perovskitas híbridas de plomo deben su nombre a la estructura cristalina (3D) generalizable mediante la fórmula ABX_3, donde A es un catión orgánico, B es un metal divalente (Pb^{2+}) y X es un anión haluro. Esta estructura consiste en un retículo de octaedros de haluro de plomo (PbX_6) unidos por los vértices, intercalados con cationes orgánicos. Si el catión es bastante pequeño para caber en la cavidad determinada por cuatro octaedros plomo-halógeno (lo cual ocurre solo si A es cesio, metilamonio o formamidinio), se forman estructuras tridimensionales (3D) estables. Si el catión orgánico es más grande, la estructura tridimensional colapsa en una bidimensional, donde láminas de tetraedros de plomo-halógeno (PbX_4) se alternan con capas de moléculas orgánicas. Aunque las estructuras 2D presenten interesantes características optoelectrónicas, en esta tesis se han estudiado solo perovskitas 3D. Dentro de la familia de las perovskitas 3D, la más investigada ha sido el ioduro de metilamonio y plomo ($MAPbI_3$), debido a sus excepcionales propiedades fotovoltaicas.

Las perovskitas híbridas de plomo presentan una gran variedad de propiedades, que las hacen ser muy interesantes para su aplicación en sistemas fotovoltaicos. Algunas de ellas son:

- Alto coeficiente de absorción

- Baja energía de enlace de los excitones
- Fácil control del ancho de banda de los materiales
- Buena movilidad de electrones y huecos
- Alta constante dieléctrica

1.2 Técnicas de deposición

Las perovskitas híbridas presentan la ventaja de poder ser depositadas en capa delgada mediante numerosos y diversos métodos de preparación, que pueden dividirse en dos clases: métodos de deposición por disolución y de alto vacío.

Métodos por disolución (Figura 1.3)

- Deposición en un solo paso
- Deposición en un solo paso con anti-disolventes
- Deposición secuencial por *spin-coating*
- Deposición secuencial por inmersión

Métodos de alto vacío (Figura 1.4)

- Co-evaporación
- Evaporación flash
- Evaporación secuencial

En esta tesis, el principal método de deposición empleado es la co-evaporación, aunque en el primer capítulo se emplea una combinación de dos métodos, la co-evaporación y la deposición secuencial, para la preparación de una perovskita mixta de yodo-bromo.

1.3 Arquitectura del dispositivo

La eficiencia de las células solares de perovskita depende en gran medida de la calidad de la capa depositada, cuya morfología viene determinada por el método de deposición y el tipo de sustrato empleados. Además, la arquitectura del dispositivo juega un papel importante a la hora de determinar la eficiencia de extracción de carga. La arquitectura del dispositivo se puede dividir en dos clases: p-i-n y n-i-p. En células p-i-n, el

material transportador de huecos (de tipo p) se deposita en el sustrato transparente debajo de la perovskita, y a continuación se deposita una capa transportadora de electrones. Finalmente, se evapora el cátodo (Ag, Al) para completar el dispositivo. Los materiales más utilizados en este tipo de configuración son polímeros conductores (PEDOT:PSS, polyTPD, etc.) como transportadores de huecos y el fullereno o sus derivados (PCBM) como transportadores de electrones.

Dentro de la configuración opuesta, n-i-p, existen dos tipos de estructuras: la plana y la mesoporosa, dependiendo de la estructura del material transportador de electrones (de tipo n) que se deposita sobre el sustrato transparente. En general, en esta configuración los materiales más empleados son el óxido de titanio (TiO_2) como transportador de electrones y el spiro-MeOTAD como transportador de huecos.

En esta tesis, se utiliza la configuración p-i-n para la fabricación de las células solares de perovskita.

1.4. Células solares de perovskita

En una célula solar el material fotoactivo absorbe luz generando pares de electrones y huecos, que son separados y extraídos hacia los electrodos por los materiales transportadores de tipo n y p, respectivamente. Para que una célula solar sea altamente eficiente, el material activo tiene que presentar una baja energía de enlace excitónica y una alta movilidad de las cargas. Estos dos parámetros son importantes porque determinan el tipo de recombinación de las cargas. Existen tres clases de recombinación en los materiales semiconductores (Figura 1.6):

- Recombinación no radiativa por defectos
- Recombinación radiativa
- Recombinación Auger no radiativa

En las células solares, para la obtención de altas eficiencias, la recombinación no radiativa tiene que ser minimizada y por ese motivo se tiene que reducir al mínimo la cantidad de defectos que haya en la capa de perovskita como en el resto del dispositivo. De ahí, la importancia de la

optimización de los métodos de deposición de la capa de perovskita, así como de la arquitectura elegida para fabricar el dispositivo.

Las células solares y los diodos orgánicos emisores de luz (OLEDs, del inglés *organic light-emitting diodes*) son dispositivos complementarios. Los OLEDs son dispositivos multicapa donde una capa de material orgánico electroluminiscente está intercalada entre capas de semiconductores orgánicos.

Los materiales óptimos para células solares tienen que ser buenos emisores de luz, además de presentar un alto coeficiente de absorción. En condiciones de circuito abierto, donde no se genera corriente, todas las cargas generadas recombinan. El voltaje de circuito abierto (V_{oc}) de la célula solar será máximo cuando todos los procesos de recombinación que ocurren en el dispositivo sean radiativos, y en ese caso la electroluminiscencia de la célula solar será también máxima. Debido a que todas las cargas se recombinarán radiativamente, el flujo de fotones absorbidos será igual al flujo emitido. Esta relación de reciprocidad permite predecir el V_{oc}, midiendo la eficiencia cuántica externa (EQE) de electroluminiscencia de los dispositivos. Por ese motivo, a lo largo de esta tesis se caracteriza tanto la eficiencia fotovoltaica como la electroluminiscencia de las células solares de perovskita.

1.5. Objetivos de la tesis

El objetivo de la tesis es el desarrollo de materiales y métodos de deposición de capas de perovskita utilizando procesos de alto vacío, principalmente mediante co-evaporación. Para la fabricación de los dispositivos, se han empleado y optimizado diferentes materiales transportadores de electrones y de huecos. La tesis está estructurada de la siguiente manera:

- Capítulo 1: Se desarrolla un método de deposición novedoso para la preparación de capas delgadas de perovskitas mixtas yodo-bromo.

- Capítulo 2: Se presenta el estudio de diferentes derivados del fullereno como materiales transportadores de electrones para conseguir células solares de perovskita de alta eficiencia.
- Capítulo 3: Se optimiza la interfaz entre la capa transportadora de electrones y el electrodo metálico, con el objetivo de reemplazar el bario cuya reactividad limita la estabilidad de los dispositivos.

Capítulo 2: Metodología

2.1. Fabricación de células solares de perovskita

La preparación y la caracterización de las células solares de perovskita tuvo lugar en una sala limpia de clase 10000 (Figura 2.1).

Todos los dispositivos estudiados durante esta tesis utilizaron la siguiente arquitectura: ITO/PEDOT:PSS/polyTPD/perovskita/fullereno/PDINO o PFNBr/Ba-Ag o Ag. Todos los materiales empleados en este trabajo están disponibles comercialmente y se emplearon sin previa purificación.

Co-evaporación de la perovskita

La deposición de la perovskita se llevó a cabo en una cámara de alto vacío integrada en una caja de guantes de atmósfera inerte, Figura 2.2. Los materiales utilizados para preparar la perovskita $MAPbI_3$ fueron MAI y PbI_2, los cuales en este proceso se subliman desde unos crisoles de cerámica con regulador de temperatura. Los sustratos están a 20 cm de las fuentes y debajo de los sustratos el sistema presenta una placa de metal que se puede abrir y cerrar para iniciar o interrumpir la deposición del material sobre los sustratos. Por último, la velocidad a la que se depositan los materiales se controla mediante dos sensores (microbalanzas de cuarzo) instalados en la cámara de vacío. Una vez rellenados los crisoles con los materiales, se hace el vacío llegando a una presión de 10^{-6} mbar. Una vez alcanzada la presión, el MAI se calienta a 75 ºC hasta conseguir una velocidad de evaporación constante. Entonces, se aumenta la temperatura del crisol de PbI_2 hasta alcanzar una velocidad de deposición que resulte en

la estequiometría correcta. El espesor de las capas de perovskita se controla con un tercer sensor, situado a la misma altura que los sustratos.

2.3. Caracterización de las células solares

Los parámetros que se utilizan para calcular la eficiencia de las células solares bajo iluminación (Figura 2.3) son:

- Corriente de circuito cerrado (J_{sc}, mA cm^{-2}, representa la corriente generada a 0 V).

- Voltaje de circuito abierto (V_{oc}, V, es el máximo voltaje generado por una célula solar con corriente igual a 0).

- Factor de forma o *fill factor* (FF, %, se define como la relación entre el punto de máxima potencia dividido entre el producto de V_{oc} y J_{sc}. Gráficamente representa la "cuadratura" de la curva de densidad de corriente contra el voltaje).

- Eficiencia de conversión energética (PCE, %, expresada por el cociente del punto de máxima potencia de la célula y la potencia irradiada sobre el dispositivo).

- Eficiencia cuántica externa (EQE_{PV}, %, representa el número de electrones extraídos mediante los contactos dividido por el número de fotones incidentes sobre el dispositivo).

En algunos estudios las células solares fueron caracterizadas como diodos emisores de luz. Los parámetros que caracterizan el rendimiento de estos dispositivos son:

- Irradiancia (W m^{-2}, representa la potencia de la luz emitida por unidad de superficie).

- Densidad de corriente (A m^{-2}, corresponde a la intensidad de corriente por unidad de superficie).

- Eficiencia de corriente (cd A^{-1}, representa la cantidad de luz emitida por unidad eléctrica inyectada en el dispositivo).

- Eficiencia de potencia (lm W^{-1}, expresa la eficiencia del diodo teniendo en cuenta el consumo de potencia).

- Eficiencia cuántica externa ($EQE_{EL,}$ %, representa el número de fotones emitidos por electrones inyectados en el dispositivo).

Capítulo 3: Dispositivos basados en perovskita mixta de haluros yodo-bromo para células solares y diodos emisores de luz

3.1 Introducción

Como hemos visto anteriormente, las células solares de silicio dominan, por ahora, el mundo de la fotovoltaica, a pesar de su alto coste. Una manera de disminuir el precio de la energía fotovoltaica es aumentar la eficiencia por unidad de superficie, un objetivo que puede conseguirse preparando células solares de tipo tándem, constituidas por dos dispositivos en serie y materiales fotoactivos con absorción de luz complementaria. Considerando el ancho de banda del silicio (1.1 eV), se podría aumentar la eficiencia por encima del 35% combinándolo con semiconductores cuyas bandas prohibidas sean de 1.7 - 1.75 eV. Las células solares de perovskita son buenas candidatas para ser incorporadas en dispositivos tándem con silicio, ya que entre su amplia variedad de propiedades, está el fácil control del ancho de banda (E_g) que puede modularse por simple intercambio de algunos de los componentes de la perovskita. Para aumentar E_g, la principal estrategia es la parcial o completa sustitución del anión haluro. La perovskita $MAPbI_3$ posee un E_g de 1.55 eV y si se remplaza completamente el yoduro por bromuro el ancho de banda aumenta hasta 2.3 eV. Asimismo, cuando el haluro se remplaza por cloruro, el E_g aumenta hasta 3.2 eV. Como hemos comentado anteriormente, el ancho de banda ideal para células solares complementarias a las de Si o CIGS es de 1.7 - 1.75 eV. Este E_g se puede conseguir con la sustitución parcial del yoduro por bromuro, formando una perovskita de haluros mixta. Aunque se hayan publicado

células solares eficientes basadas en perovskitas con un ancho de banda de 1.7 eV, estos materiales sufren segregación de fases en presencia de altas concentraciones de bromuro. Esta segregación de fases es muy perjudicial para la obtención de células solares eficientes y, a pesar de los numerosos estudios sobre este fenómeno, no ha habido una solución clara y definitiva a este problema.

En este capítulo se presenta un método de deposición innovador para la preparación de perovskita de haluros mixta. En este nuevo método, se prepara una perovskita de yodo por co-evaporación que se recubre posteriormente con una segunda capa de perovskita de bromo. Esta última es depositada mediante evaporación secuencial, evaporando primero el $PbBr_2$ y después convirtiéndolo con una disolución de MABr. Para asegurar una total conversión, se hace un tratamiento térmico de las capas a 100 ºC, permitiendo así la inter-difusión de los aniones haluros entre las dos perovskitas. La cantidad de bromo que contiene la perovskita mixta final depende del espesor de la capa de $MAPbBr_3$ depositado encima de la perovskita pura de yodo.

3.2. Metodología

Todos los materiales empleados en este trabajo están disponibles comercialmente y se utilizaron sin purificación posterior a su adquisición. La arquitectura de los dispositivos consiste en: ITO/PEDOT:PSS (80 nm)/polyTPD (20 nm)/$MAPbI_3$ (300 nm)/$MAPbBr_3$(x)/PCBM (50 nm)/Ba (10 nm)/Ag (100 nm). Las capas de PEDOT:PSS y polyTPD se prepararon por *spin-coating*. Después de cada deposición las capas fueron sometidas a un tratamiento térmico como el descrito en la metodología del capítulo 2.1. La capa de perovskita $MAPbI_3$ se preparó mediante co-evaporación del yoduro de metilamonio y el yoduro de plomo. Posteriormente y sin romper vacío se evaporó una capa de $PbBr_2$, con diferentes espesores dependiendo de la cantidad de bromuro deseada. El $PbBr_2$ se convirtió a $MAPbBr_3$ por *spin-coating* de una disolución de MABr en isopropanol. Por último, se hizo un tratamiento térmico a 100 ºC durante 5 min para obtener la estequiometría mixta $MAPb(I_{1-x}Br_x)_3$. La capa de perovskita preparada se recubrió con una capa de PCBM de 50 nm de grosor mediante *spin-coating*. El dispositivo se

completó con la deposición térmica en vacío de un cátodo metálico formado por 10 nm de Ba y 100 nm de Ag.

3.3. Resultados y discusión

La formación de la perovskita mixta de yoduro-bromuro se investigó por diferentes técnicas de caracterización. En los espectros de absorción (Figura 3.2) se observó el desplazamiento de la absorción al aumentar el espesor de la perovskita de bromo depositada encima de la de yodo, debido a un aumento de la cantidad de bromuro incluida. De este modo, el ancho de banda de las distintas perovskitas fabricadas aumentó a medida que aumentaba el espesor de la capa de bromuro, alcanzando 1.92 eV cuando el espesor de la capa fue de 200 nm. Mediante difracción de rayos X (Figura 3.4) también se observó la formación de la perovskita mixta en las diferentes composiciones, ya que al igual que en la absorción, también se produjo un desplazamiento de los picos al aumentar la cantidad de bromo. Para las capas de perovskita mixta con alta concentración de bromuro (x = 0.4 y x = 0.6) se observó una contribución minoritaria de perovskita de yodo, debido a una conversión incompleta de la perovskita. Este efecto se debe probablemente a un espesor de $PbBr_2$ demasiado elevado para que la difusión de los iones haluro fuese completa. Igualmente se observó un cambio en la morfología con respecto a la perovskita de yodo y de bromo (Figura 3.3), con la formación de granos más pequeños en la perovskita mixta.

Posteriormente los dispositivos fabricados fueron caracterizados como células solares (Figura 3.5). Primero se midió la eficiencia cuántica externa, en la que se apreció la misma tendencia observada en el espectro de absorción, con un desplazamiento hacia menores longitudes de onda al aumentar la cantidad de bromo. La disminución del EQE_{PV} fue mayor en las dos concentraciones con mayores cantidades de bromo, debido a la conversión incompleta de los materiales observada en el XRD. La misma tendencia se observó cuando se midieron las curvas de voltaje, con una disminución de la corriente de circuito cerrado. Por otra parte, el voltaje de circuito abierto aumentó cuando la cantidad de bromuro fue incrementada. El FF fue similar en todas las concentraciones excepto para las dos mayores,

en las que disminuyó considerablemente. Finalmente, se consiguió una eficiencia de 9.3% en células solares de perovskita mixta con ancho de banda de 1.7 eV.

Los dispositivos fueron caracterizados también como emisores de luz (Figura 3.6), y se observó un desplazamiento del espectro de electroluminiscencia hacia longitudes de onda menores, al aumentar la cantidad de bromo. Se observó una segunda componente del espectro de electroluminiscencia en las perovskitas con mayores cantidades de bromo, lo cual confirma la conversión incompleta de la perovskita mixta para elevados espesores de $PbBr_2$. Finalmente se calculó el factor de idealidad de los diodos con las distintas composiciones para buscar información sobre el tipo de recombinación de carga en los dispositivos. Para diodos con $x < 0.2$, el factor de idealidad encontrado fue cercano a 2, indicando que la recombinación tiene lugar por medio de trampas o defectos. Para composiciones con $x > 0.2$, el factor de idealidad se aproximó a 1, indicando recombinación directa de las cargas, debido probablemente a la presencia de perovskita pura de yodo residual, la cual tiene un ancho de banda menor que la perovskita mixta de haluros.

3.4. Conclusiones

En este capítulo se ha presentado un método innovador para la obtención de perovskita mixta de haluros yodo-bromo, con un ancho de banda de 1.7 eV aproximadamente, que tiene potencial aplicación en células solares tipo tándem con Si o CIGS. En este estudio se obtuvieron perovskitas con estequiometría variable en función del espesor de la capa de perovskita de bromo depositada encima de la perovskita pura de yodo. Se observó un aumento del voltaje de circuito abierto, consiguiendo eficiencias de 9.3% para la perovskita mixta con ancho de banda de 1.7 eV. Finalmente, con las diferentes técnicas de caracterización se observó la conversión incompleta a perovskita mixta cuando la cantidad de bromo añadida era mayor de 0.2.

Capítulo 4: Alto voltaje de circuito abierto determinado por fullerenos en células solares eficientes de perovskita

4.1 Introducción

En las células solares de perovskita las capas transportadoras de electrones (ETLs) juegan un papel importante, ya que además de extraer y transportar los electrones de la capa activa hacia el cátodo, sirven como bloqueadores de huecos, reduciendo así la recombinación en la interfaz. Algunas de las características de los ETLs son indispensables para obtener buenas eficiencias, como por ejemplo: una alta movilidad de carga, el buen alineamiento energético con las capas adyacentes y una buena morfología. Desde el comienzo de la investigación sobre las células solares de perovskita, se han utilizado diferentes transportadores de electrones, dependiendo sobre todo de la arquitectura de la célula solar empleada. Por ejemplo, en la configuración n-i-p, el TiO_2 es el material más utilizado, mientras que en la configuración p-i-n los derivados de los fullerenos son los más empleados, ya que presentan propiedades muy acordes con los requisitos mencionados previamente. Además, algunos estudios han demostrado que los fullerenos podrían pasivar los defectos superficiales en la perovskita, reduciendo de esta manera la recombinación en las células solares. En este capítulo se presentan cinco derivados del fullereno diferentes y se estudian sus propiedades como materiales transportadores de electrones en células solares de perovskita de tipo p-i-n.

4.2. Metodología

Todos los materiales empleados en este trabajo están disponibles comercialmente y se utilizaron sin purificación posterior a su adquisición. La arquitectura de los dispositivos consiste en: ITO/PEDOT:PSS (80 nm)/polyTPD (20 nm)/$MAPbI_3$ (320 nm)/fullereno (50 nm)/Ba (10 nm)/Ag (100 nm). Las capas de PEDOT:PSS y polyTPD se prepararon por *spin-coating*. Después de cada deposición las capas fueron sometidas a un tratamiento térmico como el descrito en la metodología del capítulo 2.1. La capa de perovskita $MAPbI_3$ se preparó mediante co-evaporación del yoduro de metilamonio y el yoduro de plomo. La perovskita se recubrió con una

capa de fullereno de 50 nm de grosor, mediante *spin-coating*. El dispositivo se completó con la deposición térmica en vacío de un cátodo metálico formado por 10 nm de Ba y 100 nm de Ag.

4.3. Resultados y discusión

En este capítulo se estudiaron dos familias de derivados de los fullerenos. Por una parte, se utilizaron tres derivados PCB-R con cadenas alquílicas de metilo (PCBM), butilo (PCBB) y hexilo (PCBH) y, por otra parte, dos derivados IP-R con cadenas alquílicas de butilo (IPB) y hexilo (IPH). Las dos familias de derivados presentan absorción óptica diferente (Figura 4.3), en función de las estructuras y de la cadena alquílica empleada (Figura 4.1). Los derivados PCB-R presentaron dos picos de absorción sobre 300 nm y 350 nm, respectivamente, mientras que los derivados IP-R solo presentaron un pico de absorción con un máximo a 325 nm. Las distintas capas transportadoras de electrones depositadas sobre la perovskita co-evaporada presentaron características diferentes dependiendo del derivado empleado. Cuando el PCBM se depositó encima de la perovskita, aparecieron algunos defectos que pueden convertirse en centros de recombinación de carga, como puede observarse en la Figura 4.5. Las capas de los otros derivados estuvieron libres de defectos ya que los compuestos presentaron una mayor solubilidad al poseer cadenas alquílicas más largas. Además, la morfología superficial de estos derivados del fullereno fue más homogénea que la obtenida con el PCBM, mejorando el recubrimiento de la perovskita.

Los dispositivos fabricados con los diferentes fullerenos fueron caracterizados inicialmente como células solares (Figura 4.7). Se observaron valores más elevados de voltaje de circuito abierto con los derivados IP-R en comparación con los PCB-R, en concreto de unos 10 - 20 mV. Esto es un efecto del menor potencial de reducción de los derivados IP-R. Además, los valores de corriente de circuito cerrado fueron más elevados para los dispositivos que utilizaron IPH como transportador de electrones. Para el resto de los fullerenos, los valores de J_{sc} fueron parecidos, con valores menores para las células solares con PCBM debido probablemente a los defectos observados en la capa. No se observó una clara tendencia en el FF,

y en todos los dispositivos los valores fueron altos, de entre 75 - 80%. Finalmente, las mejores eficiencias se obtuvieron empleando el IPH como transportador de electrones, alcanzando valores máximos de 14.6%.

Estos dispositivos también fueron caracterizados como diodos emisores de luz. En la Figura 4.9 observamos que la eficiencia cuántica externa para la electroluminiscencia depende del derivado de fullereno empleado, siendo las obtenidas para los derivados IP-R las más elevadas. Los dispositivos con estos dos fullerenos como ETL, fueron los que también alcanzaron mayores valores de V_{oc}, lo que sugiere una disminución de la recombinación no-radiativa al interfaz de la perovskita con estos dos derivados de fullereno.

4.4. Conclusiones

En este capítulo se ha presentado el estudio de cinco derivados de fullereno como materiales transportadores de electrones en células solares p-i-n. Se comprobó que los derivados de fullereno con cadenas alquílicas más largas formaron capas más homogéneas en comparación con las capas de PCBM. Las mejores eficiencias se consiguieron con los compuestos IP-R, ya que presentaron mayores valores de V_{oc} y de J_{sc}. El aumento del voltaje de circuito abierto vino acompañado por un incremento de la eficiencia cuántica de electroluminiscencia, sugiriendo una reducción de la recombinación no-radiativa. Por tanto, podemos concluir que estos nuevos derivados de fullereno son materiales muy prometedores como transportadores de electrones en células solares de perovskita.

Capítulo 5: Optimización de la interface en células solares de perovskita

5.1. Introducción

En los dispositivos electrónicos existe una barrera energética interfacial entre el nivel de Fermi de los electrodos metálicos, como son Ag y Au, y el orbital molecular no ocupado de más baja energía (LUMO) del transportador de electrones (PCBM), que conlleva una pérdida de potencial al extraer las cargas. Por este motivo, se emplean materiales que mejoren las propiedades eléctricas y electrónicas en la interfaz entre la capa activa

(perovskita) y los electrodos, para así obtener eficiencias más elevadas. Para minimizar la pérdida de energía en el contacto, la barrera de energía en la interfaz entre el cátodo y la capa de PCBM debería ser idealmente nula (contacto óhmico). Por esta razón, se ha estudiado el efecto de una capa interfacial que reduzca la diferencia de energía entre la capa de fullereno y el contacto metálico (Al, Ag, Au). Se ha estudiado el efecto en la extracción selectiva de carga de dos materiales iónicos (PDINO, PFNBr), procesados por disolución y depositados entre la capa de fullereno y el cátodo. En este estudio se emplea el derivado de fullereno IPH, seleccionado en estudios presentados en el capítulo anterior. Además, en este capítulo se estudia la importancia del empleo de una capa bloqueadora de electrones entre la capa de PEDOT:PSS y la perovskita.

5.2. Metodología

Todos los materiales empleados en este trabajo están disponibles comercialmente y se utilizaron sin purificación posterior a su adquisición, excepto el PDINO, que fue sintetizado por el grupo de investigación de la Profesora Ángela Sastre. La arquitectura de los dispositivos consiste en: ITO/PEDOT:PSS (80 nm)/polyTPD (20 nm)/$MAPbI_3$ (320 nm)/IPH (50 nm)/PDINO o PFNBr/Ba (10 nm)/Ag (100 nm). Las capas de PEDOT:PSS y polyTPD se prepararon por *spin-coating*. Después de cada deposición las capas fueron sometidas a un tratamiento térmico como el descrito en el capítulo 2.1. La capa de perovskita $MAPbI_3$ se preparó mediante co-evaporación del yoduro de metilamonio y el yoduro de plomo. La perovskita se recubrió con una capa de IPH de 50 nm de grosor, mediante *spin-coating*. Después, una fina capa de PDINO y/o PFNBr fue depositada por *spin-coating.* El dispositivo se completó con la deposición térmica en vacío de un cátodo metálico formado por 10 nm de Ba y 100 nm de Ag o sólo por 100 nm de Ag cuando se utilizaron las capas intermedias iónicas.

5.3. Resultados y discusión

En este capítulo se estudió, en primer lugar, el efecto del uso del polyTPD como capa bloqueadora de electrones. En la Figura 5.4, se observó la diferencia tanto en las curvas de corriente-voltaje bajo iluminación como en la eficiencia cuántica externa. La curva relativa a las células solares sin

polyPTD presentó un V_{oc} menor, indicando una recombinación directa de cargas en la interfaz entre el PEDOT:PSS y la perovskita. Además, el PEDOT:PSS presenta una función de trabajo menor que la del polyTPD, lo cual disminuye el fotovoltaje del dispositivo. La recombinación directa y el menor fotovoltaje observado con el PEDOT:PSS también afectaron al FF. De igual manera, la eficiencia cuántica externa (EQE_{PV}) fue mucho menor en ausencia de polyTPD, obteniendo corrientes de circuito cerrado menores. Esto es indicativo de las diferentes propiedades de transporte que posee la perovskita evaporada comparada con células de perovskita preparadas por disolución, ya que en la mayoría de trabajos donde la perovskita se deposita por disolución no se utiliza ninguna capa bloqueadora de electrones. Siguiendo con este estudio, también se analizó el factor de idealidad para los dos tipos de dispositivo, con y sin polyTPD. Para los dispositivos sin la capa bloqueadora de electrones, el factor de idealidad se aproximó a 1, apuntando a la recombinación directa de las cargas, mientras que en los dispositivos con polyTPD el factor de idealidad fue 2, señal de una recombinación interfacial mediada por trampas o defectos.

En segundo lugar, se emplearon dos materiales como capas intermedias para la extracción de electrones. Por una parte se depositó el PDINO entre la capa de fullereno (IPH) y el cátodo (Ag); en este caso la presencia de un grupo N-óxido introduce un momento dipolar en la interfaz entre el metal y el material orgánico, bajando de esta manera la función de trabajo del metal y facilitando la transferencia de electrones desde el IPH hasta el cátodo. En segundo lugar, se depositó de manera análoga una capa de PFNBr entre el fullereno y el electrodo. La incorporación de esta capa intermedia también permite crear un contacto óhmico en la interfaz, mejorando así la extracción de los electrones hacia el electrodo.

Los dispositivos fabricados fueron caracterizados como células solares. Aparte de las células solares con las dos capas iónicas, también se prepararon células solares de referencia con Ba-Ag como cátodo. En la Figura 5.7 podemos observar las curvas de voltaje tanto en oscuridad como bajo iluminación, así como la eficiencia cuántica externa. Los resultados obtenidos fueron similares para todos los dispositivos fabricados. Todos

ellos presentaron FF elevados, entre 74 y 77%, de acuerdo con la buena calidad de las capas preparadas. Igualmente, los valores de V_{oc} obtenidos fueron elevados en todos los casos, aproximadamente 1.1 V, gracias al bajo potencial de reducción del IPH como transportador de electrones. La principal diferencia entre las capas de extracción de electrones estudiadas fue la corriente de circuito cerrado (J_{sc}), donde los valores menores fueron obtenidos con el Ba-Ag como electrodo. Además este cátodo presentó EQE_{PV} menores entre las longitudes de onda de 650 y 770 nm, comparadas con las obtenidas con el PDINO y el PFNBr. Esto es consecuencia de la menor reflectancia del Ba/Ag frente al Ag, que hace que las células solares tengan un perfil de absorción de luz diferente. Finalmente, las mejores eficiencias se consiguieron utilizando una capa fina de PDINO entre la capa de fullereno y el cátodo, alcanzando eficiencias de hasta 15.2%.

Como se hizo en los capítulos anteriores, los dispositivos fabricados fueron caracterizados también como diodos emisores de luz. Como se puede comprobar en la Figura 5.9, los valores de eficiencia cuántica externa fueron mayores cuando el bario fue sustituido por la capa de PDINO o de PFNBr, sugiriendo que las mejorías observadas se deben en parte a una reducción de la recombinación no-radiativa a la interfaz entre el fullereno y el cátodo.

5.4. Conclusiones

En este capítulo se ha estudiado la extracción de carga en la interfaz entre la perovskita y los electrodos en células solares de configuración p-i-n. En primer lugar, se ha evaluado la importancia del uso de una capa bloqueadora de electrones entre el PEDOT:PSS y la perovskita. Se ha observado que existe una recombinación directa de las cargas a la interfaz entre el PEDOT:PSS y la perovskita, haciendo necesario el uso de una capa de polyTPD entre los dos materiales. En segundo lugar, se han evaluado dos capas intermedias para extraer los electrones del fullereno hacia el cátodo, PDINO y PFNBr. En ambos casos, se han obtenido eficiencias similares o incluso mayores con respeto a dispositivos donde se ha utilizado Ba-Ag como cátodo. Esto es consecuencia de la formación de unos dipolos favorables en la interfaz entre la capa de fullereno y el cátodo, que hace que la función de trabajo del metal se reduzca y que permita extraer más

eficientemente los electrones. En la caracterización de la electroluminiscencia, se ha observado una reducción de la recombinación no-radiativa cuando el bario fue sustituido por la capa de PDINO o PFNBr.

Capítulo: 6 Conclusiones generales

El objetivo de esta tesis consistía en el desarrollo de células solares de perovskita eficientes preparadas mediante métodos de alto vacío y de disolución. La importancia de optimizar la interfaz entre la perovskita y las capas transportadoras de cargas se ha estudiado en los dos últimos capítulos de esta tesis, obteniendo mejores eficiencias, debido a la reducción sustancial de la recombinación no-radiativa.

En el capítulo 3 se ha presentado un método innovador para la obtención de la perovskita mixta de yodo-bromo, utilizando principalmente métodos de alto vacío. Las distintas concentraciones de bromo se controlaron mediante el espesor de la capa de $MAPbBr_3$ depositada encima de la perovskita pura de yodo. Entre las distintas composiciones preparadas, se preparó una célula solar de perovskita con un ancho de banda de 1.7 eV y con una eficiencia de 9.3%, la cual es particularmente interesante para la fabricación de células solares tándem con silicio o CIGS. Cuando se incrementó el contenido de bromo por encima de 0.2, las eficiencias de las células solares disminuyeron drásticamente debido a una disminución de la corriente de circuito cerrado. Esto se atribuye a la incompleta formación de la perovskita mixta, causando la segregación del material en fases distintas que favorecen la recombinación directa de carga.

En el capítulo 4 se ha evaluado la importancia en la elección de la capa transportadora de electrones en células solares de perovskita evaporada en la configuración de tipo p-i-n. Cinco derivados de fullereno con cadenas alquílicas diferentes fueron estudiados. En este trabajo se observó que los derivados de fullerenos que presentaban cadenas alquílicas más largas presentaban mayores solubilidades, y por tanto las capas de estos compuestos presentaban menos defectos cuando eran depositadas encima de la perovskita. Como resultado, los dispositivos basados en estos

fullerenos alcanzaron mejores eficiencias, debido principalmente a una mejora en el V_{oc}, ya que los defectos observados en la capa de PCBM pueden actuar como centros de recombinación de carga. De la misma manera, cuando los dispositivos fabricados fueron caracterizados como diodos emisores de luz, las mejores eficiencias cuánticas externas se alcanzaron con los derivados del fullereno con cadenas alquílica más largas, más concretamente de los derivados IP-R. Esto indica que el uso de estos derivados disminuye la recombinación no radiativa al electrodo.

La optimización de las interfaces en las células solares de perovskita evaporada se ha evaluado en el capítulo 5. En primer lugar, se estudió la importancia de la deposición de una capa bloqueadora de electrones en la interfaz PEDOT:PSS/perovskita. Los dispositivos preparados sin la capa de polyTPD presentaron una severa recombinación en la interface afectando a la eficiencia de los mismos. Después se estudió la deposición de dos capas iónicas intermedias (PDINO, PFNBr) entre el fullereno y el cátodo (Ag), con el objetivo de poder sustituir el Ba. La formación de dipolos en estas capas ayuda en la transferencia de electrones desde la capa de IPH hacia el Ag, y reduce de esta manera la recombinación de las cargas en la interfaz. Se alcanzaron así eficiencias similares e incluso mayores a las obtenidas en dispositivos con Ba.

Bibliography

1. M. Konstantakou and T. Stergiopoulos, *Journal of Materials Chemistry A*, 2017, **5**, 11518-11549.
2. C. C. Stoumpos, L. Frazer, D. J. Clark, Y. S. Kim, S. H. Rhim, A. J. Freeman, J. B. Ketterson, J. I. Jang and M. G. Kanatzidis, *Journal of the American Chemical Society*, 2015, **137**, 6804-6819.
3. J.-C. Hebig, I. Kühn, J. Flohre and T. Kirchartz, *ACS Energy Letters*, 2016, **1**, 309-314.
4. A. Kulkarni, T. Singh, M. Ikegami and T. Miyasaka, *RSC Advances*, 2017, **7**, 9456-9460.
5. T. Baikie, N. S. Barrow, Y. Fang, P. J. Keenan, P. R. Slater, R. O. Piltz, M. Gutmann, S. G. Mhaisalkar and T. J. White, *Journal of Materials Chemistry A*, 2015, **3**, 9298-9307.
6. *Journal of the Physical Society of Japan*, 2002, **71**, 1694-1697.
7. Y. Zhao and K. Zhu, *Chemical Society Reviews*, 2016, **45**, 655-689.
8. S. Pang, H. Hu, J. Zhang, S. Lv, Y. Yu, F. Wei, T. Qin, H. Xu, Z. Liu and G. Cui, *Chemistry of Materials*, 2014, **26**, 1485-1491.
9. Q. Lin, A. Armin, R. C. R. Nagiri, P. L. Burn and P. Meredith, *Nature Photonics*, 2015, **9**, 106-112.
10. V. D'Innocenzo, G. Grancini, M. J. P. Alcocer, A. R. S. Kandada, S. D. Stranks, M. M. Lee, G. Lanzani, H. J. Snaith and A. Petrozza, 2014, **5**, 3586.
11. D. Sapori, M. Kepenekian, L. Pedesseau, C. Katan and J. Even, *Nanoscale*, 2016, **8**, 6369-6378.
12. H.-H. Fang, R. Raissa, M. Abdu-Aguye, S. Adjokatse, G. R. Blake, J. Even and M. A. Loi, *Advanced Functional Materials*, 2015, **25**, 2378-2385.
13. C. C. Stoumpos, C. D. Malliakas and M. G. Kanatzidis, *Inorganic Chemistry*, 2013, **52**, 9019-9038.
14. S. D. Stranks, G. E. Eperon, G. Grancini, C. Menelaou, M. J. P. Alcocer, T. Leijtens, L. M. Herz, A. Petrozza and H. J. Snaith, *Science*, 2013, **342**, 341-344.
15. V. Gonzalez-Pedro, E. J. Juarez-Perez, W.-S. Arsyad, E. M. Barea, F. Fabregat-Santiago, I. Mora-Sero and J. Bisquert, *Nano Letters*, 2014, **14**, 888-893.
16. W.-J. Yin, T. Shi and Y. Yan, *Advanced Materials*, 2014, **26**, 4653-4658.
17. Q. Dong, Y. Fang, Y. Shao, P. Mulligan, J. Qiu, L. Cao and J. Huang, *Science*, 2015, **347**, 967-970.
18. D. Shi, V. Adinolfi, R. Comin, M. Yuan, E. Alarousu, A. Buin, Y. Chen, S. Hoogland, A. Rothenberger, K. Katsiev, Y. Losovyj, X. Zhang, P. A. Dowben, O. F. Mohammed, E. H. Sargent and O. M. Bakr, *Science*, 2015, **347**, 519-522.

19. J. H. Noh, S. H. Im, J. H. Heo, T. N. Mandal and S. I. Seok, *Nano Letters*, 2013, **13**, 1764-1769.
20. B. Suarez, V. Gonzalez-Pedro, T. S. Ripolles, R. S. Sanchez, L. Otero and I. Mora-Sero, *The Journal of Physical Chemistry Letters*, 2014, **5**, 1628-1635.
21. E. T. Hoke, D. J. Slotcavage, E. R. Dohner, A. R. Bowring, H. I. Karunadasa and M. D. McGehee, *Chemical Science*, 2015, **6**, 613-617.
22. R. Comin, G. Walters, E. S. Thibau, O. Voznyy, Z.-H. Lu and E. H. Sargent, *Journal of Materials Chemistry C*, 2015, **3**, 8839-8843.
23. G. Xing, N. Mathews, S. Sun, S. S. Lim, Y. M. Lam, M. Grätzel, S. Mhaisalkar and T. C. Sum, *Science*, 2013, **342**, 344-347.
24. G. E. Eperon, S. D. Stranks, C. Menelaou, M. B. Johnston, L. M. Herz and H. J. Snaith, *Energy & Environmental Science*, 2014, **7**, 982-988.
25. J.-W. Lee and N.-G. Park, *MRS Bulletin*, 2015, **40**, 654-659.
26. M. Sessolo, C. Momblona, L. Gil-Escrig and H. J. Bolink, *MRS Bulletin*, 2015, **40**, 660-666.
27. H. Zhou, Q. Chen and Y. Yang, *MRS Bulletin*, 2015, **40**, 667-673.
28. L. Zheng, D. Zhang, Y. Ma, Z. Lu, Z. Chen, S. Wang, L. Xiao and Q. Gong, *Dalton Transactions*, 2015, **44**, 10582-10593.
29. D. T. Moore, H. Sai, K. W. Tan, D.-M. Smilgies, W. Zhang, H. J. Snaith, U. Wiesner and L. A. Estroff, *Journal of the American Chemical Society*, 2015, **137**, 2350-2358.
30. N. J. Jeon, J. H. Noh, Y. C. Kim, W. S. Yang, S. Ryu and S. I. Seok, *Nature Materials*, 2014, **13**, 897-903.
31. H. Cho, S.-H. Jeong, M.-H. Park, Y.-H. Kim, C. Wolf, C.-L. Lee, J. H. Heo, A. Sadhanala, N. Myoung, S. Yoo, S. H. Im, R. H. Friend and T.-W. Lee, *Science*, 2015, **350**, 1222-1225.
32. J. W. Jung, S. T. Williams and A. K. Y. Jen, *RSC Advances*, 2014, **4**, 62971-62977.
33. M. Xiao, F. Huang, W. Huang, Y. Dkhissi, Y. Zhu, J. Etheridge, A. Gray-Weale, U. Bach, Y.-B. Cheng and L. Spiccia, *Angewandte Chemie International Edition*, 2014, **53**, 9898-9903.
34. Y. Zhou, M. Yang, W. Wu, A. L. Vasiliev, K. Zhu and N. P. Padture, *Journal of Materials Chemistry A*, 2015, **3**, 8178-8184.
35. J. Burschka, N. Pellet, S.-J. Moon, R. Humphry-Baker, P. Gao, M. K. Nazeeruddin and M. Gratzel, *Nature*, 2013, **499**, 316-319.
36. K. Liang, D. B. Mitzi and M. T. Prikas, *Chemistry of Materials*, 1998, **10**, 403-411.
37. J.-H. Im, I.-H. Jang, N. Pellet, M. Grätzel and N.-G. Park, *Nature Nanotechnology*, 2014, **9**, 927-932.
38. J.-H. Im, H.-S. Kim and N.-G. Park, *APL Materials*, 2014, **2**, 081510.
39. M. Liu, M. B. Johnston and H. J. Snaith, *Nature*, 2013, **501**, 395-398.
40. O. Malinkiewicz, A. Yella, Y. H. Lee, G. M. Espallargas, M. Graetzel, M. K. Nazeeruddin and H. J. Bolink, *Nature Photonics*, 2014, **8**, 128-132.

41. L. K. Ono, S. Wang, Y. Kato, S. R. Raga and Y. Qi, *Energy & Environmental Science*, 2014, **7**, 3989-3993.
42. D. Liu, M. K. Gangishetty and T. L. Kelly, *Journal of Materials Chemistry A*, 2014, **2**, 19873-19881.
43. M. R. Leyden, L. K. Ono, S. R. Raga, Y. Kato, S. Wang and Y. Qi, *Journal of Materials Chemistry A*, 2014, **2**, 18742-18745.
44. A. Ng, Z. Ren, Q. Shen, S. H. Cheung, H. C. Gokkaya, G. Bai, J. Wang, L. Yang, S. K. So, A. B. Djurisic, W. W.-f. Leung, J. Hao, W. K. Chan and C. Surya, *Journal of Materials Chemistry A*, 2015, **3**, 9223-9231.
45. C.-W. Chen, H.-W. Kang, S.-Y. Hsiao, P.-F. Yang, K.-M. Chiang and H.-W. Lin, *Advanced Materials*, 2014, **26**, 6647-6652.
46. D. B. Mitzi, M. T. Prikas and K. Chondroudis, *Chemistry of Materials*, 1999, **11**, 542-544.
47. S. Ahmad, C. Hanmandlu, P. K. Kanaujia and G. V. Prakash, *Opt. Mater. Express*, 2014, **4**, 1313-1323.
48. G. Longo, L. Gil-Escrig, M. J. Degen, M. Sessolo and H. J. Bolink, *Chemical Communications*, 2015, **51**, 7376-7378.
49. Z. Song, S. C. Watthage, A. B. Phillips and M. J. Heben, *PHOTOE*, 2016, **6**, 022001-022001.
50. A. Kojima, K. Teshima, Y. Shirai and T. Miyasaka, *Journal of the American Chemical Society*, 2009, **131**, 6050-6051.
51. J.-H. Im, C.-R. Lee, J.-W. Lee, S.-W. Park and N.-G. Park, *Nanoscale*, 2011, **3**, 4088-4093.
52. H.-S. Kim, C.-R. Lee, J.-H. Im, K.-B. Lee, T. Moehl, A. Marchioro, S.-J. Moon, R. Humphry-Baker, J.-H. Yum, J. E. Moser, M. Grätzel and N.-G. Park, 2012, **2**, 591.
53. M. M. Lee, J. Teuscher, T. Miyasaka, T. N. Murakami and H. J. Snaith, *Science*, 2012, **338**, 643-647.
54. W. Chen, Y. Wu, J. Liu, C. Qin, X. Yang, A. Islam, Y.-B. Cheng and L. Han, *Energy & Environmental Science*, 2015, **8**, 629-640.
55. Q. Wang, Y. Shao, Q. Dong, Z. Xiao, Y. Yuan and J. Huang, *Energy & Environmental Science*, 2014, **7**, 2359-2365.
56. M. A. Green, K. Emery, Y. Hishikawa, W. Warta, E. D. Dunlop, D. H. Levi and A. W. Y. Ho-Baillie, *Progress in Photovoltaics: Research and Applications*, 2017, **25**, 3-13.
57. H. Zhou, Q. Chen, G. Li, S. Luo, T.-b. Song, H.-S. Duan, Z. Hong, J. You, Y. Liu and Y. Yang, *Science*, 2014, **345**, 542-546.
58. C. Momblona, L. Gil-Escrig, E. Bandiello, E. M. Hutter, M. Sessolo, K. Lederer, J. Blochwitz-Nimoth and H. J. Bolink, *Energy & Environmental Science*, 2016, **9**, 3456-3463.
59. W. Chen, Y. Wu, Y. Yue, J. Liu, W. Zhang, X. Yang, H. Chen, E. Bi, I. Ashraful, M. Grätzel and L. Han, *Science*, 2015, **350**, 944-948.

60. J. You, L. Meng, T.-B. Song, T.-F. Guo, Y. Yang, W.-H. Chang, Z. Hong, H. Chen, H. Zhou, Q. Chen, Y. Liu, N. De Marco and Y. Yang, *Nature Nanotechnology*, 2016, **11**, 75-81.
61. K.-C. Wang, J.-Y. Jeng, P.-S. Shen, Y.-C. Chang, E. W.-G. Diau, C.-H. Tsai, T.-Y. Chao, H.-C. Hsu, P.-Y. Lin, P. Chen, T.-F. Guo and T.-C. Wen, 2014, **4**, 4756.
62. T. C. Sum and N. Mathews, *Energy & Environmental Science*, 2014, **7**, 2518-2534.
63. A. Baumann, S. Väth, P. Rieder, M. C. Heiber, K. Tvingstedt and V. Dyakonov, *The Journal of Physical Chemistry Letters*, 2015, **6**, 2350-2354.
64. X. Wu, M. T. Trinh, D. Niesner, H. Zhu, Z. Norman, J. S. Owen, O. Yaffe, B. J. Kudisch and X. Y. Zhu, *Journal of the American Chemical Society*, 2015, **137**, 2089-2096.
65. O. D. Miller, E. Yablonovitch and S. R. Kurtz, *IEEE Journal of Photovoltaics*, 2012, **2**, 303-311.
66. Z.-G. Zhang, B. Qi, Z. Jin, D. Chi, Z. Qi, Y. Li and J. Wang, *Energy & Environmental Science*, 2014, **7**, 1966-1973.
67. T. Todorov, T. Gershon, O. Gunawan, Y. S. Lee, C. Sturdevant, L.-Y. Chang and S. Guha, *Advanced Energy Materials*, 2015, **5**, 1500799-n/a.
68. Z. Yu, M. Leilaeioun and Z. Holman, 2016, **1**, 16137.
69. D. P. McMeekin, G. Sadoughi, W. Rehman, G. E. Eperon, M. Saliba, M. T. Hörantner, A. Haghighirad, N. Sakai, L. Korte, B. Rech, M. B. Johnston, L. M. Herz and H. J. Snaith, *Science*, 2016, **351**, 151-155.
70. J. F. Geisz and D. J. Friedman, *Semiconductor Science and Technology*, 2002, **17**, 769.
71. N. N. Lal, T. P. White and K. R. Catchpole, *IEEE Journal of Photovoltaics*, 2014, **4**, 1380-1386.
72. W. S. Yang, J. H. Noh, N. J. Jeon, Y. C. Kim, S. Ryu, J. Seo and S. I. Seok, *Science*, 2015, **348**, 1234-1237.
73. D. B. Mitzi, K. Chondroudis and C. R. Kagan, *IBM Journal of Research and Development* 2001, **45**, 29-45.
74. Z.-K. Tan, R. S. Moghaddam, M. L. Lai, P. Docampo, R. Higler, F. Deschler, M. Price, A. Sadhanala, L. M. Pazos, D. Credgington, F. Hanusch, T. Bein, H. J. Snaith and R. H. Friend, *Nature Nanotechnology*, 2014, **9**, 687-692.
75. N. K. Kumawat, A. Dey, A. Kumar, S. P. Gopinathan, K. L. Narasimhan and D. Kabra, *ACS Applied Materials & Interfaces*, 2015, **7**, 13119-13124.
76. N. K. Kumawat, A. Dey, K. L. Narasimhan and D. Kabra, *ACS Photonics*, 2015, **2**, 349-354.
77. Y.-H. Kim, H. Cho, J. H. Heo, T.-S. Kim, N. Myoung, C.-L. Lee, S. H. Im and T.-W. Lee, *Advanced Materials*, 2015, **27**, 1248-1254.
78. G. Xing, N. Mathews, S. S. Lim, N. Yantara, X. Liu, D. Sabba, M. Grätzel, S. Mhaisalkar and T. C. Sum, *Nature Materials*, 2014, **13**, 476-480.
79. J. H. Heo, D. H. Song and S. H. Im, *Advanced Materials*, 2014, **26**, 8179-8183.

80. C. Bi, Y. Yuan, Y. Fang and J. Huang, *Advanced Energy Materials*, 2015, **5**, 1401616.
81. Y. Chen, T. Chen and L. Dai, *Advanced Materials*, 2015, **27**, 1053-1059.
82. M. Hu, C. Bi, Y. Yuan, Y. Bai and J. Huang, *Advanced Science*, 2016, **3**, 1500301.
83. Y. Shao, Y. Fang, T. Li, Q. Wang, Q. Dong, Y. Deng, Y. Yuan, H. Wei, M. Wang, A. Gruverman, J. Shield and J. Huang, *Energy & Environmental Science*, 2016, **9**, 1752-1759.
84. A. Sadhanala, F. Deschler, T. H. Thomas, S. E. Dutton, K. C. Goedel, F. C. Hanusch, M. L. Lai, U. Steiner, T. Bein, P. Docampo, D. Cahen and R. H. Friend, *The Journal of Physical Chemistry Letters*, 2014, **5**, 2501-2505.
85. G.-J. A. H. Wetzelaer, M. Scheepers, A. M. Sempere, C. Momblona, J. Ávila and H. J. Bolink, *Advanced Materials*, 2015, **27**, 1837-1841.
86. L. Gil-Escrig, G. Longo, A. Pertegas, C. Roldan-Carmona, A. Soriano, M. Sessolo and H. J. Bolink, *Chemical Communications*, 2015, **51**, 569-571.
87. C. Bi, Y. Yuan, Y. Fang and J. Huang, *Advanced Energy Materials*, 2015, **5**.
88. K. Wojciechowski, M. Saliba, T. Leijtens, A. Abate and H. J. Snaith, *Energy & Environmental Science*, 2014, **7**, 1142-1147.
89. S. Gubbala, V. Chakrapani, V. Kumar and M. K. Sunkara, *Advanced Functional Materials*, 2008, **18**, 2411-2418.
90. E. Hendry, M. Koeberg, B. O'Regan and M. Bonn, *Nano Letters*, 2006, **6**, 755-759.
91. D. Liu and T. L. Kelly, *Nature Photonics*, 2014, **8**, 133-138.
92. J. P. Correa Baena, L. Steier, W. Tress, M. Saliba, S. Neutzner, T. Matsui, F. Giordano, T. J. Jacobsson, A. R. Srimath Kandada, S. M. Zakeeruddin, A. Petrozza, A. Abate, M. K. Nazeeruddin, M. Gratzel and A. Hagfeldt, *Energy & Environmental Science*, 2015, **8**, 2928-2934.
93. Y. Hou, C. O. R. Quiroz, S. Scheiner, W. Chen, T. Stubhan, A. Hirsch, M. Halik and C. J. Brabec, *Advanced Energy Materials*, 2015, **5**, 1501056.
94. P.-W. Liang, C.-C. Chueh, S. T. Williams and A. K. Y. Jen, *Advanced Energy Materials*, 2015, **5**, 1402321.
95. M. A. Green, A. Ho-Baillie and H. J. Snaith, *Nature Photonics*, 2014, **8**, 506-514.
96. X. Meng, Y. Bai, S. Xiao, T. Zhang, C. Hu, Y. Yang, X. Zheng and S. Yang, *Nano Energy*, 2016, **30**, 341-346.
97. Y. Shao, Y. Yuan and J. Huang, 2016, **1**, 15001.
98. J.-Y. Jeng, Y.-F. Chiang, M.-H. Lee, S.-R. Peng, T.-F. Guo, P. Chen and T.-C. Wen, *Advanced Materials*, 2013, **25**, 3727-3732.
99. Y. Xing, C. Sun, H. L. Yip, G. C. Bazan, F. Huang and Y. Cao, *Nano Energy*, 2016, **26**, 7-15.
100. S. Shao, M. Abdu-Aguye, L. Qiu, L.-H. Lai, J. Liu, S. Adjokatse, F. Jahani, M. E. Kamminga, G. H. ten Brink, T. T. M. Palstra, B. J. Kooi, J. C. Hummelen

and M. Antonietta Loi, *Energy & Environmental Science*, 2016, **9**, 2444-2452.
101. C. Sun, Z. Wu, H.-L. Yip, H. Zhang, X.-F. Jiang, Q. Xue, Z. Hu, Z. Hu, Y. Shen, M. Wang, F. Huang and Y. Cao, *Advanced Energy Materials*, 2016, **6**, 1501534.
102. Y. Li, K. Lu, X. Ling, J. Yuan, G. Shi, G. Ding, J. Sun, S. Shi, X. Gong and W. Ma, *Journal of Materials Chemistry A*, 2016, **4**, 10130-10134.
103. W. Wang, J. Yuan, G. Shi, X. Zhu, S. Shi, Z. Liu, L. Han, H.-Q. Wang and W. Ma, *ACS Applied Materials & Interfaces*, 2015, **7**, 3994-3999.
104. S. Shao, Z. Chen, H. H. Fang, G. H. ten Brink, D. Bartesaghi, S. Adjokatse, L. J. A. Koster, B. J. Kooi, A. Facchetti and M. A. Loi, *Journal of Materials Chemistry A*, 2016, **4**, 2419-2426.
105. A. B. Sieval, N. D. Treat, D. Rozema, J. C. Hummelen and N. Stingelin, *Chemical Communications*, 2015, **51**, 8126-8129.
106. S. Cook, H. Ohkita, Y. Kim, J. J. Benson-Smith, D. D. C. Bradley and J. R. Durrant, *Chemical Physics Letters*, 2007, **445**, 276-280.
107. J. H. Seo, A. Gutacker, Y. Sun, H. Wu, F. Huang, Y. Cao, U. Scherf, A. J. Heeger and G. C. Bazan, *Journal of the American Chemical Society*, 2011, **133**, 8416-8419.
108. T. M. Khan, Y. Zhou, A. Dindar, J. W. Shim, C. Fuentes-Hernandez and B. Kippelen, *ACS Applied Materials & Interfaces*, 2014, **6**, 6202-6207.
109. S. Torabi, J. Liu, P. Gordiichuk, A. Herrmann, L. Qiu, F. Jahani, J. C. Hummelen and L. J. A. Koster, *ACS Applied Materials & Interfaces*, 2016, **8**, 22623-22628.
110. P. Docampo, J. M. Ball, M. Darwich, G. E. Eperon and H. J. Snaith, 2013, **4**, 2761.
111. S. Bai, Z. Wu, X. Wu, Y. Jin, N. Zhao, Z. Chen, Q. Mei, X. Wang, Z. Ye, T. Song, R. Liu, S.-t. Lee and B. Sun, *Nano Research*, 2014, **7**, 1749-1758.
112. J. Min, Z.-G. Zhang, Y. Hou, C. O. Ramirez Quiroz, T. Przybilla, C. Bronnbauer, F. Guo, K. Forberich, H. Azimi, T. Ameri, E. Spiecker, Y. Li and C. J. Brabec, *Chemistry of Materials*, 2015, **27**, 227-234.
113. P.-W. Liang, C.-Y. Liao, C.-C. Chueh, F. Zuo, S. T. Williams, X.-K. Xin, J. Lin and A. K. Y. Jen, *Advanced Materials*, 2014, **26**, 3748-3754.
114. Q. Xue, Z. Hu, J. Liu, J. Lin, C. Sun, Z. Chen, C. Duan, J. Wang, C. Liao, W. M. Lau, F. Huang, H.-L. Yip and Y. Cao, *Journal of Materials Chemistry A*, 2014, **2**, 19598-19603.
115. C. Li, F. Wang, J. Xu, J. Yao, B. Zhang, C. Zhang, M. Xiao, S. Dai, Y. Li and Z. a. Tan, *Nanoscale*, 2015, **7**, 9771-9778.
116. H. Zhang, H. Azimi, Y. Hou, T. Ameri, T. Przybilla, E. Spiecker, M. Kraft, U. Scherf and C. J. Brabec, *Chemistry of Materials*, 2014, **26**, 5190-5193.
117. O. Malinkiewicz, C. Roldán-Carmona, A. Soriano, E. Bandiello, L. Camacho, M. K. Nazeeruddin and H. J. Bolink, *Advanced Energy Materials*, 2014, **4**, 1400345.

118. J. Seo, S. Park, Y. Chan Kim, N. J. Jeon, J. H. Noh, S. C. Yoon and S. I. Seok, *Energy & Environmental Science*, 2014, **7**, 2642-2646.
119. J. You, Y. Yang, Z. Hong, T.-B. Song, L. Meng, Y. Liu, C. Jiang, H. Zhou, W.-H. Chang, G. Li and Y. Yang, *Applied Physics Letters*, 2014, **105**, 183902.
120. Z. He, C. Zhong, S. Su, M. Xu, H. Wu and Y. Cao, *Nature Photonics*, 2012, **6**, 591-595.
121. L. Gil-Escrig, C. Momblona, M. Sessolo and H. J. Bolink, *Journal of Materials Chemistry A*, 2016, **4**, 3667-3672.
122. T. Liu, F. Jiang, J. Tong, F. Qin, W. Meng, Y. Jiang, Z. Li and Y. Zhou, *Journal of Materials Chemistry A*, 2016, **4**, 4305-4311.
123. J. H. Seo and T.-Q. Nguyen, *Journal of the American Chemical Society*, 2008, **130**, 10042-10043.
124. Z. He, C. Zhong, X. Huang, W.-Y. Wong, H. Wu, L. Chen, S. Su and Y. Cao, *Advanced Materials*, 2011, **23**, 4636-4643.

Index of figures

Fig 1.1 (a) Crystal structure of cubic lead halide perovskite (α phase) (b) Crystal structure of the tetragonal crystal system (β phase) and orthorhombic phase (γ phase) of $MAPbX_3$. (c) Tolerance factors of a series of halides perovskites. Adapted from reference 7……14

Fig 1.2 (a) Absorption coefficient of mixed $MAPb(I_{1-x}Br_x)_3$ thin films with increasing bromide content, adapted from reference 21. (b) Absorption spectra of mixed $MAPb(Br_{3-x}Cl_x)$ thin film with increasing chloride content, adapted from reference 22. ……16

Fig 1.3 Schematics of the different solution deposition methods for hybrid perovskite thin-films, shown here in the case of methylammonium lead halides. Adapted from Reference 28.……17

Fig 1.4 Schematics of the different vacuum deposition methods for hybrid perovskite thin-films, shown here in the case of methylammonium lead halides. Adapted from Reference 28.……20

Fig 1.5 Schematics of perovskite solar cells in the (a) n-i-p mesoscopic, (b) n-i-p planar, (c) p-i-n planar, and (d) p-i-n mesoscopic structures. Adapted from reference 49……21

Fig 1.6 Scheme of the different types of recombination depending on the exciton binding energy. Adapted from reference 62……24

Fig 2.1. Nitrogen-filled glove box installed inside the clean-room at the Instituto de Ciencia Molecular (ICMol) of the Universidad de Valencia where all the devices were prepared and characterized……31

Fig 2.2 Scheme of the thermal vacuum deposition tool used in the dual source evaporation process……..33

Fig 2.3 J-V characteristic of a typical solar cell, highlighting the main parameters used in the characterization. The product of V_{mp} and J_{mp} is the maximum power that the solar cell can deliver.……..35

Fig 3.1 Process schematics with the deposition steps used to prepare the mixed halide perovskite……..44

Fig 3.2 (a) Optical absorption spectra for a series of $MAPb(I_{1-x}Br_x)_3$ perovskite films prepared with increasing thicknesses of the $MAPbBr_3$.(b) Variation of the optical bandgap for the same series of $MAPb(I_{1-x}Br_x)_3$ films, with the estimated Br content (right axis) (c) Optical absorption of a pristine $MAPbBr_3$ perovskite thin film obtained by converting a pre-deposited $PbBr_2$ layer by spin-coating with MABr solutions in isopropanol. No annealing is needed in order to obtain the pure bromide-based perovskite.……..45

Fig 3.3 On the top, correspondent evolution of the surface morphology as monitored by scanning electron microscopy (SEM, scale bar 500nm). On the bottom, atomic force microscopy (AFM) characterization of the (a) $MAPbI_3$, (b) $PbBr_2$ and (c) $MAPb(I_{1-x}Br_x)_3$. The indexes indicate (i) the surface topography (scale bar 1 cm), and (ii) a profile along the scanning direction……..46

Fig 3.4 X-ray diffraction (XRD) patterns of a series of $MAPb(I_{1-x}Br_x)_3$ perovskite thin films with increasing Br content (x)……..47

Fig 3.5 (a) EQE, (b) J-V curves under illumination, and (c) zoom on a log scale plot on the Voc for a series of solar cells using $MAPb(I_{1-x}Br_x)_3$ perovskite with increasing content (x)……..48

Fig 3.6 (a) Current density (left, symbols) and irradiance (right, lines) versus applied bias, (b) normalized electroluminescence spectra (the arrow indicates the blue shift for increasing Br content) for the mixed halide perovskite diode series ……50

Fig 3.7 External quantum efficiency (EQE) versus voltage applied of a series of diodes employing $MAPb(I_{1-x}Br_x)_3$ as the active material……..51

Fig 3.8 Calculated ideality factors for diodes based on $MAPb(I_{1-x}Br_x)_3$ with increasing Br content……52

Fig 4.1 (a) Device layout (b) Chemical structures of the fullerene derivatives, PCBM, PCBB, PCBH, IPB, IPH ……..66

Fig 4.2 (a) XRD pattern and (b) optical absorption spectrum for the vacuum deposited perovskite film (thickness 320 nm)……...66

Fig 4.3 Optical absorption spectra for thin films of the five different fullerenes deposited on quartz ……67

Fig 4.4 AFM topographies of a) PCBM b) PCBH c) PCBB d) IPB e) IPH…….68

Fig 4.5 Optical microscope images of the fullerene layers deposited on top of the perovskite: i) PCBM, ii) PCBH, iii) PCBB, iv) IPB and v) IPH……68

Fig 4.6 External quantum efficiency (EQE_{pv}) of the different diodes……69

Fig 4.7 Electrical characterization of the solar cells employing different fullerenes: (a) current density versus voltage under 1 sun illumination and in the dark (inset); (b) zoom around the V_{oc} of the J-V curves on a log scale plot for the solar cell series……70

Fig 4.8 Photovoltaics parameters (Jsc,Voc,FF,PCE) of the different fullerenes for > 8 devices per configuration……71

Fig 4.9 Current density and irradiance versus the applied voltage and (b) corresponding external quantum efficiency (EQE_{EL}) for diodes employing different fullerene derivatives ……..72

Fig 5.1 Schematics of the p-i-n perovskite solar cell with the molecular structures of PDINO and PFNBr ……85

Fig 5.2 (a) GIXRD pattern and (b) optical absorption spectrum of the vacuum deposited perovskite film (320 nm), with preferred orientation along (100) and (001) directions ……85

Fig 5.3 (a) J-V curves in the dark and (b) calculated ideality factor for devices with and without polyTPD. The electron extraction used for these cells is IPH/Ba-Ag ……86

Fig 5.4 J-V curves under illumination for devices with and without polyTPD, using IPH/Ba-Ag as electron extraction layer. The inset shows the corresponding photovoltaic external quantum efficiency (EQE_{pv})……..87

Fig 5.5 Flat energy band diagram for the materials used in the device preparation (b) Optical absorption spectra of both electron extraction layers on quartz substrates ……88

Fig 5.6 Atomic Force microscopy (AFM) characterization of the surface of a) IPH b) IPH/PDINO and c) IPH/PFNBr. All films are deposited onto an ITO/PEDOT:PSS/$MAPbI_3$ stack ……..89

Fig 5.7 (a) J-V curves under 1 sun illumination for the devices employing different cathode interlayers; the inset shows the J-V curve collected in the dark. (b) External quantum efficiency (EQE_{PV}) of the same diodes series ….90

Fig 5.8 Statistics of the PCE measured for the different electron extraction layers used……..92

Fig 5.9 (a) Current density and irradiance versus voltage applied and (b) External quantum efficiency versus the voltage applied for the devices with different electron extraction layers……..93

Index of tables

Table 1 Composition, optical and photovoltaic parameters for a series of solar cells based on $MAPbI_{(1-x)}Br_x)_3$……..49

Table 2 Average photovoltaic parameters for the devices using different electron extraction layers ……91

List of abbreviations

AFM	Atomic force microscopy
E_g	Band gap energy
ETM	Electron transport material
HTM	Hole transport material
ITO	Indium tin oxide
CIGS	Copper indium gallium selenide/sulphide
TiO_2	Titanium dioxide
LED	Light emitting diodes
LUMO	Lowest unoccupied molecular orbital
HOMO	Highest occupied molecular orbital
MAI	Methylammonium iodide
MABr	Methylammonium bromide
$MAPbBr_3$	Methylammonium lead tribromide
$MAPbI_3$	Methylammonium lead triiodide
$MAPbCl_3$	Methylammonium lead cloride
PCE	Power conversion efficiency
PL	Photoluminescence
PLQY	Photoluminescence quantum yield
PEDOT:PSS	Poly(3,4ethylenedioxythiophene)-poly(styrenesulfonate)

polyTPD	poly(N,N'-bis(4-butylphenyl)–N,N'-bis (phenyl)-benzidine)
PCBM	(6,6)-phenyl C61-butyric acid methyl ester
PFNBr	poly(9,9-bis[3'-(N,N,N-ethyldimethylammonium) propyl]- fluorene-2,7-diyl) dibromide -alt- (9,9-dioctylfluorene-2,7-diyl)
PDINO	N,N'-bis(dimethylaminopropyl-N'''-oxide)-perylene-3,4:9,10-tetracarboxidiimide
SEM	Scanning electron microscopy
RMS	Root-mean-square roughness
XRD	X-Ray diffraction
GIXRD	Grazing incidence x-Ray diffraction
V	Voltage
PSC	Perovskite solar cell
V_{OC}	Open circuit voltage
J	Current density
J_{SC}	Short circuit current density
I	Current
FF	Fill factor
EQE	External quantum efficiency
SSD	Solid state dye

Other contributions of the author

1. Sloane Evariste, Martina Sandroni, Thomas W. Rees, Cristina Roldán Carmona, Lidón Gil-Escrig, Henk J. Bolink, Etienne Baranoff and Eli Zysman-Colman "*Fluorine-free blue-green emitters for light-emitting electrochemical cells*" J. Mater. Chem. C. 2, 5793-5804 (2014)

2. C.Momblona, O. Malinkiewicz, C.Roldán-Carmona, A.Soriano, L.Gil-Escrig, E.Bandiello, M.Sheepers, E.Edri and H.J.Bolink "*Efficient methylammonium lead iodide perovskite solar cells with active layers from 300 to 900 nm*"APL Materials. 2, 081504 (2014)

3. Lidón Gil-Escrig, Giulia Longo, Antonio Pertegás, Cristina Roldán-Carmona, A.Soriano, MIchele Sessolo and Henk J.Bolink **"***Efficient photovoltaic and electroluminescent perovskite devices*",Chem. Commun. 51, 3, 569-571 (2015)

4. Giulia Longo, Lidón Gil-Escrig, Maarten J.Degen , Michele Sessolo and Henk J. Bolink *"Perovskite solar cells prepared by flash evaporation"*Chem. Commun. 51, 7376-7378 (2015).

5. Andreas M.Bünzli, Edwin C. Contable, Catherine E. Housecroft, Alessandro Prescimone, Jennifer A. Zampese, Giulia Longo, Lidón Gil-Escrig, Antonio Pertegás, Enrique Ortí and Henk J.Bolink "Exceptionally long-lived light-emitting electrochemical cells: multiple intra-cation π-stacking interactions in [Ir(C^N)2(N^N)][PF6] emitters"Chem. Sci. 6, 2843-2852 (2015)

6. Nikolai Kaihovirta, Giulia Longo, Lidón Gil-Escrig, Henk J. Bolink, and Ludvig Edman "*Self-absorption in a light-emitting electrochemical cell based on an ionic transitionmetal complex*"Appl. Phys. Lett. 106, 103502 (2015)

7. Michele Sessolo, Cristina Momblona, Lidón Gil-Escrig, and Henk J.Bolink, "*Photovoltaic devices employing vaccum-deposited perovskite layers*"MRS Bulletin. 40, 660−666 (2015)

8. G. El-Hajje, C.Momblona, L.Gil-Escrig, J.Avila, T.Guillemot, JF.Guillemoles, M. Sessolo, HJ. Bolink, L. Lombez.*"Quantification of spatial inhomogeneity in perovskite solar cells by hyperspectral luminescence imaging"* Energy Environ. Sci. ,9, 2286-2294 (2016)

9. C. D. Ertl; L. Gil-Escrig; J. Cerdá; A. Pertegás; H. J. Bolink; J. M. Junquera-Hernández; A. Prescimone; M. Neuburger; E. C. Constable; E. Ortí; C. E. Housecroft *"Regioisomerism in cationic sulfonyl-substituted [Ir(C^N)2(N^N)]+ complexes: its*

influence on photophysical properties and LEC performance" Dalton Trans. 45, 11668-11681 (2016)

10. M. Sessolo, L. Gil-Escrig, G. Longo; H. J. Bolink *"Perovskite Luminescent Materials"* Top. Curr. Chem. 374: 52 (2016)

11. C. Momblona; L. Gil-Escrig; E. Bandiello; E. M. Hutter; M. Sessolo; K. Lederer; J. Blochwitz-Nimoth; H. J. Bolink *"Efficient vacuum deposited p-i-n and n-i-p perovskite solar cells employing doped charge transport layers"* Energy Environ. Sci. 9, 3456 (2016)

12. Enrico Bandiello, Jorge Ávila, Lidón Gil-Escrig, Eelco Tekelenburg, Michele Sessolo and Henk J. Bolink *"Influence of mobile ions on the electroluminescence characteristics of methylammonium lead iodide perovskites diodes" J. Mater. Chem. A*, 2016,4, 18614-18620.

13. D. Forgács; L. Gil-Escrig; D. Pérez-Del-Rey; C. Momblona; J. Werner; B. Niesen; C. Ballif; M. Sessolo *"Efficient Monolithic Perovskite/Perovskite Tandem Solar Cells"* Adv. Energy Mater. (2017). DOI: 10.1002/aenm.201602121

14. K. Tvingstedt, L. Gil-Escrig, C. Momblona, P. Rieder, D. Kiermasch, M. Sessolo, A. Baumann, Henk J. Bolink, and Vladimir Dyakonov *"Removing Leakage and Surface Recombination in Planar Perovskite Solar Cells"* ACS Energy Lett. 2, 424-430 (2017).

15. Laura Calió, Cristina Momblona, Lidon Gil-Escrig, Samrana Kazima, Michele Sessolo,Ángela Sastre-Santos, Henk J. Bolink, Shahzada Ahmada *"Vacuum deposited perovskite solar cells employing dopant-free triazatruxene as the hole transport material"*Solar Energy Materials & Solar Cells 163, 237–241 (2017)

16. Tejas S. Sherkar, Cristina Momblona, Lidón Gil-Escrig, Henk J. Bolink,and L. Jan Anton Koster *"Improving Perovskite Solar Cells: Insights from a Validated Device Model*" *Adv. Energy Mater*. 1602432 (2017)

17. Tejas S. Sherkar, Cristina Momblona, Lidón Gil-Escrig, Jorge Ávila, Michele Sessolo, Henk J. Bolink,and L. Jan Anton Koster *"Recombination in perovskite solar cells: Significance of Grain Boundaries, Interface Traps, and Defect Ions" ACS Energy Lett.*, 2017, 2 (5), pp 1214–1222